High-Rate Deformation Behavior and Applications of Fluid Filled Reticulated Foams

By
Giorgia Bettin

BA, Mechanical Engineering, University of California, Berkeley (2002)

M.S., Mechanical Engineering, MIT(2005)

Submitted to the Department of Mechanical Engineering
in Partial Fulfillment of the Requirements for the Degree of
Doctor in Philosophy in Mechanical Engineering

at the

Massachusetts Institute of Technology
[September 2007]
Aug 2007

Signature of Author...
Department of Mechanical Engineering
August 8th, 2007

Certified by...
Gareth H. McKinley
Professor of Mechanical Engineering
Thesis Supervisor

Accepted by...
Lallit Anand
Chairman, Department Committee on Graduate Students

High-Rate Deformation Behavior and Applications of Fluid Filled Reticulated Foams

By
Giorgia Bettin

Submitted to the Department of Mechanical Engineering
On August 8th, 2007 in partial fulfillment of the
requirements for the Doctor in Philosophy in
Mechanical Engineering

ABSTRACT

The need for smarter and adaptive, energy absorption materials especially for human protection applications has fueled the interest in new and alternative energy absorbing composites. In this thesis a 'novel' energy absorbing fluid-composite that utilized a shear thickening fluid is developed. Shear-thickening fluids are a class of field responsive fluids that have the ability to transition from a low viscosity state to a high viscosity state under an imposed deformation field.

A shear thickening fluid composed of silica monodisperse spherical particles of $0.3 \pm 0.03\ \mu m$ diameter dispersed in ethylene glycol at volume fractions up to ϕ=60% has been characterized. The behavior of the silica suspensions is studied under steady shear, small and large amplitude oscillatory shear flow and also in transient extensional flow. Oscillatory experiments indicate that both the onset and magnitude of the shear thickening depends on the frequency and strain applied and show that rapid time-varying deformations result in maximum energy dissipation. Two different regimes are observed in extensional flow measurement: at low extension rates the suspensions respond as a viscous rate-thinning fluid, whereas beyond a critical extension rate, the suspension strain-hardens and ultimately fractures in a solid-like fashion.

Polyurethane open cell or 'reticulated' foam with a relative density of 0.03 and average cell size of 360 μm is chosen to envelop the concentrated silica suspensions. The behavior of this nonlinear fluid-solid composite is studied over a range of filling fractions under quasi-static deformation rates (strain rates between $10^{-2} - 1\ s^{-1}$), under dynamic impact loading (with energy densities of $e = 10^5 - 10^6\ J/m^3$) and under high strain-rate deformations (strain rates up to 800 s^{-1}). Results show that, if the foam is filled with a shear thickening suspension, the composite stiffens even at strain rates of $10^{-2}\ s^{-1}$ as the impregnated fluid shear-thickens due to the high local strain rates that develop on cellular length scales. Experiments at high impact loadings revealed two different mechanisms for energy absorption: at low impact energies viscous dissipation is dominant; whereas after a critical impact energy is reached, the fluid undergoes a transition from liquid-like to solid-like. High-speed digital video-imaging shows that cracks form and propagate through the sample and the impact energy is absorbed by viscoplastic deformation.

Potential applications for this fluid-solid composite include Traumatic Brain Injuries (TBI) protection and Primary Blast Injuries (PBI) mitigation. Traumatic Brain Injury (TBI) is a serious and potentially fatal injury that results from rapid accelerations of the head, and subjects the brain to high intracranial pressure and shear stresses. To reduce TBI damage, one needs to reduce the magnitude and rate of increase of the intracranial overpressure created by blasts or impacts and subsequent accelerations of the head. We investigated the use of the shear-thickening fluid-based composite to mitigate TBI and we found that through the mechanism of viscoplastic deformation, with solidification and shear banding, the composite was able to absorb large amount of energies (10^6 J/m^3) and still maintain stresses below critical levels. Additionally, the energy absorbing properties of the composite were found to be independent of the magnitude of the incoming energy.

Blast injuries are caused by high rate loading of the chest cavity after impact from a blast wave. The resultant pressure wave is transmitted and reflected inside the chest cavity where, at certain points, the pressure gradient became too big for the alveoli to sustain resulting in bursting and bleeding. A shock tube apparatus has been used to test the material response of the STF based composite. Single layer geometries have shown to provide some protection but they also always induced a magnification of the peak pressure which is related to the weight of the samples. A sandwich geometry formed by layering fluid-filled foam facing the incoming wave backed by unfilled foam is found to reduce the rate of pressure rise by 3 orders of magnitude. This behavior can be well described by a double spring-mass-damper system. The layered composite is found to respond linearly with increases in incoming pressure, as the rate of pressure rise has a linear relationship with the magnitude of the incoming pressure. The results found in this study suggest that the STF based composite is an excellent candidate for use in applications of both TBI protection and PBI mitigation.

Thesis Supervisor: Gareth H. McKinley

Title: Professor of Mechanical Engineering

Acknowledgments

I would like to thank my advisor, Gareth McKinley for his support and constant encouragement. A special thanks also goes to my group mates and at the Non-Newtonian Fluids lab for the endless discussions and support throughout the past few years. Finally, I would like to extend my thanks to the Institute for soldier Nanotechnologies (ISN) for providing financial support.

Table of Content

1. Introduction

Shear thickening fluids (STF) have fueled much interest in the filed of personal protection and are currently widely studied because of their unique ability to transition from a low viscosity to a high viscosity fluid, almost in solid like state. Their particular behavior makes these fluids ideal for energy absorption applications. While the fluid is in the low viscosity state, under normal conditions, it allows for user mobility and flexibility, but as it undergoes the shear-thickening transition when impacted (under large stresses), it absorbs some of the energy of the impact while helping to shunt (to transfer) the remaining. Additionally, the critical stress (onset) can be selected and tuned a priori for the specific application by choosing the appropriate shear thickening fluid components, for example the types and size of particles or background fluid.

Shear thickening fluids are also of particular interest because of their 'method of deployment' or activation. In fact shear thickening fluids do not require any external activation from the user, but they will activate (transition from low to high viscosity) only when subjected to a critical stress loading. This is not the case, for example, with electrorheological and magnetorheological fluids, which have also been studied for energy absorption applications. These systems require an imposed electric or magnetic field and have a switching time of the order of 10 ms, an order of magnitude greater then shear-thickening fluids.

The armed forces are particularly interested in these fluids as there is a pressing need for personal protection gear that is efficient at energy absorption yet still flexible enough to wear in combat where soldier mobility and comfort is vital. Particularly promising are the application of these fluids for Traumatic Brain Injury (TBI) protection and Primary Blast Injuries (PBI) mitigation. TBI is caused by the rapid acceleration or deceleration of the head that can result in coup and countercoup pressures and shear stresses in the brain inside the skull [1]. These types of injuries are common not only in the war zone but also in sport injuries and car and motorcycles crashes. PBI occurs when a body is exposed to a blast wave and is due to the resulting high pressure differential that is created across body tissue. Mitigation of these injuries can potentially benefit from development of shear-thickening fluid-based composites as they require materials that have the potential of absorbing large amount of energies while maintaining flexibility and conform to the user body shape during normal use.

One of the major concerns when trying to create an effective energy-absorbing composite that utilizes shear-thickening fluids (STF) is the interaction between the fluid and the enveloping geometry. The rheological response of shear thickening fluids is greatly affected by the local geometry and therefore the local deformation rates at which it is strained. Open cell elastomeric foams provide a potentially ideal packaging as they can amplify, at the pore scale, the global deformation rates imposed on the fluid. Additionally, these foams are flexible and they can conform to various surfaces, but at the same time the foam keeps the fluid contained through capillarity while allowing it to flow in between pores.

Additional constraints have to be taken into consideration when designing an efficient system for soldier protection applications. In fact, some functional requirements are not necessarily related to the level of protection, as for example weight, power requirements, integration of the system with current suit design, and of course comfort and flexibility of the final product. Using STF-foam systems offers a number of advantages from the soldier's perspective as they do not require 'user activation' or external power for operation; the fluid-solid composite is also compliant under normal operation and therefore allows for greater mobility and flexibility as compared to standard body armor. Weight minimization is a very important aspect of the design in which shear thickening fluids can offer an advantage over other types of energy absorbing material. In fact, if necessary, the overall density of the resulting material could be decreased by making the solid phase of the STF from hollow spheres or by using lighter material components such as charged polymeric particles rather than the common silica fillers employed presently. Additionally because these systems do not require power for operation they reduce the need for batteries and external power supplies, which are required for other 'smart fluid' based systems such as for magnetorheological and electrorheological composites.

In this work we investigate how shear thickening fluids can be efficiently utilized as part of an energy absorbing composite for the applications of traumatic brain injuries and primary blast injuries protection. For this purpose a silica-based suspension has been prepared and characterized and this has then been impregnated in open cell polyurethane foam. The resultant composites have been characterized under a range of loading rates that vary between quasi-static deformations rates (10^{-2} s^{-1}) to shock wave loadings.

2. Literature Review

2.1. Shear Thickening Fluids -- Introduction & Review

2.1.1. Introduction

Shear thickening fluids are part of a class of fluids commonly referred as "field-activated;" the means of activation in this case being imposition of an external deformation rate. This phenomenon is described as a steplike increase in viscosity as applied rate reaches a critical value; the fluids being low viscosity at imposed rates lower than the critical value, and high viscosity when rate exceed the critical value. The shear thickening behavior can be continuous when the fluid viscosity gradually increases after the critical shear rate or discontinuous if the viscosity jumps from one value to another (normally many orders of magnitude greater) at one specific shear rate as in the case illustrated in Figure 2.1.1. Shear thickening fluids are composed of highly concentrated suspensions dispersed in a carrier fluid. The thickening behavior of these suspensions is normally seen at high volume fraction so that the particles are dense enough that their average separation in equilibrium conditions is less than the particles diameter and therefore multiple-body and lubrication interaction between particles are of importance [2]. The shear thickening behavior of these fluids have been studied for well over a half century; some comprehensive reviews of the field can be found in Barnes [3], Hoffman [4, 5] and Laun [6]and more recently Stickel and Powell [2].

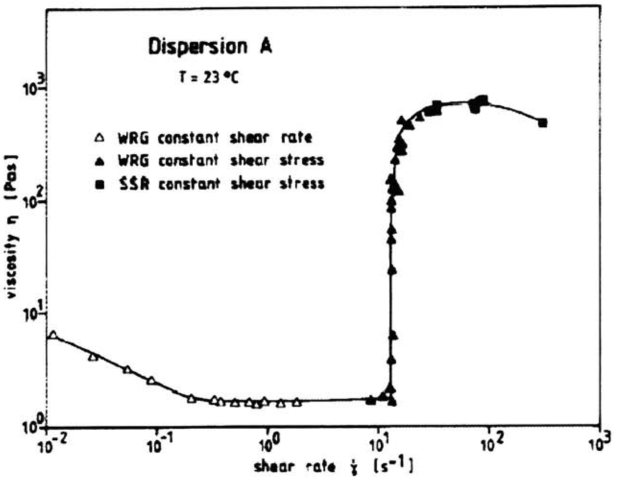

Figure 2.1.1: Viscosity of 400 nm Latex particles suspension in diethylene glycol at volume fraction of 50.4 % vs. shear rate as measured in a modified Weissenberg rheogoniometer and Sandwich Rheometer.[6] For this case the critical shear rate is 10 1/s.

2.1.2. Mechanism of Shear Thickening

In the case of extreme or discontinuous shear thickening behavior the fluid response at the critical shear rate has been historically difficult to study since most rheometer operated by controlling the imposed deformation rate. Only recently, with the improvement of stress controlled rheometers and with the help of additional techniques which can characterized the corresponding microstructure (neutron scattering [7-10], rheo-optical devices [11, 12]) has it became possible to rigorously study the shear thickening phenomenon and its microstructure. Additionally, computer simulations have recently contributed to the understanding of the mechanism of shear thickening. Stokesian Dynamics techniques [13-16] are commonly used to simulate the behavior of many-body interactions in the suspension, but other methods, like dissipative particles dynamics[17], and the Lagrange multiplier fictitious domain method [18] are also used. Two different mechanisms have been proposed from such calculations to explain these fluids behavior: the Order-Disorder theory and the 'Hydrocluster' theory.

2.1.2.1. Order-Disorder Theory

The order-disorder mechanism was first suggested by Hoffman [19] which observed that monodisperse suspensions under shear generate diffraction patterns under white light. An example of these patterns can be seen in Figure 2.1.2. Hoffman [19] developed a model to characterize this diffraction phenomena and showed that Figure 2.1.2 (A) corresponds to spheres layered in hexagonal packings while Figure 2.1.2 (B) suggests randomly positioned spheres.

According to this theory, as the suspension is sheared, particles align in hexagonally packed layers parallel to the plane of shear. After a critical stress is reached, flow instabilities start to grow and they induce particle motion out of their ordered layers; these particles then collide and jam into each other and produce the rise in viscosity.

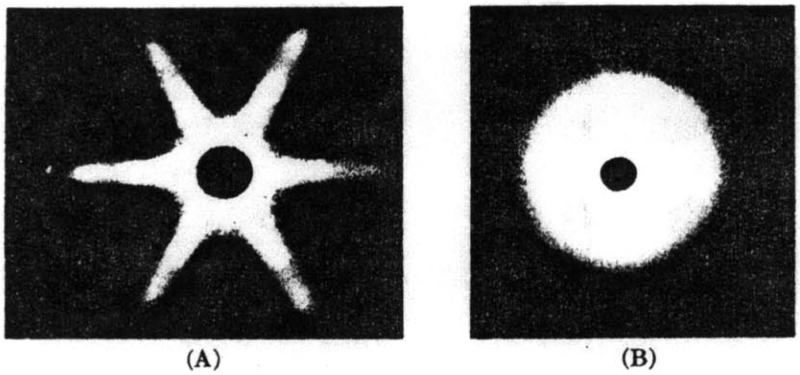

Figure 2.1.2: Diffraction patterns from monodisperse plastisols sheared in simple shearing flow. (A) Sample shear below critical shear rate. (B) Sample shear above critical shear rate [19].

2.1.2.2. Hydrocluster Theory

Another possible explanation for the shear thickening behavior of concentrated suspension is found in the 'Hydrocluster' theory. This theory is based on a model that accounts for the force balance between the hydrodynamic forces imposed by a shearing flow and forces arising by interparticles interactions. According to this theory at low stresses (below the critical value) interparticle interactions, either electrostatic or Brownian, allow the particles to easily flow past each other; this results in a 'low viscosity' state. As the stress is increased, lubrication forces between the particles grow until, when the lubrication and interparticles forces are of the same order of magnitude, the particles in suspension 'jam' into a stress-bearing cluster, commonly referred as a 'hydrocluster'; this is what creates the increase in the suspension viscosity. This theory was first suggested by Brady [13] on the basis of Stokesian Dynamics simulations and was consequently supported through rheo-optical experiment by Wagner [12] and D'Haene [11]. Neutron scattering was also used by Laun [6] to probe the fluid microstructure in both the shear thinning and shear thickening region. The microstructure was found to be highly dependent on the particle size distribution which obscured the results.

2.1.2.3. Scaling Models

Scaling models are useful to understand the shear thickening phenomena and to be able to predict the fluid response. Bender and Wagner [8] proposed a scaling based on the ratio between Brownian and hydrodynamic forces. From Bachelor [20] we obtain an expression for the Brownian force as:

$$F_{Brow} = -k_B T \frac{\partial \ln g(r)}{\partial r} \tag{2.1}$$

where k_B is Boltzmann's constant, T absolute temperature, and g(r) is the equilibrium pair distribution function which is proportional to the probability of finding the center of mass of a second particle a distance r away to a given central particle [21]. We can also express the hydrodynamic force as:

$$F_{Hydro} = {3\pi\mu a^3\dot{\gamma}} \big/ {2h} \tag{2.2}$$

where μ is the solvent viscosity, a is the particles size, $\dot{\gamma}$ is the shear rate, and h is the characteristic distance between particles. We then define a dimensionless critical stress as the ratio between hydrodynamic and Brownian forces as follows:

$$\tau_{crit}^{Br} = \frac{F_{Hydro}}{F_{Brow}} = \frac{3\pi\mu a^3\dot{\gamma} \big/ 2h}{-k_B T \left.\dfrac{\partial \ln g(r)}{\partial r}\right|_{r=2a+h}} \tag{2.3}$$

The hydrodynamic force can also be adjusted to account for the effect of the 'surrounding particles'. If we multiply equation (2.2) by the suspension reduced viscosity $\eta \big/ \mu = \left(1 - \phi \big/ \phi_{\max}\right)^{-2}$ as first defined by deKruif [22] we arrive to an expression for the scaling model as presented by Bender and Wagner [8].

$$\frac{\tau_{crit} a^3}{k_B T} = \frac{-h}{3\pi}\frac{\eta}{\mu_0}\left(\frac{\partial \ln g(r)}{\partial r}\right) \tag{2.4}$$

where τ_{crit} is the dimensional critical stress for the onset of shear thickening. Bender and Wagner used this scaling to collapse all their data for bimodal dispersions as illustrated in Figure 2.1.3; irrespective of the mixing composition they found that shear thickening occurred at a τ_{crit} of 10 [8].

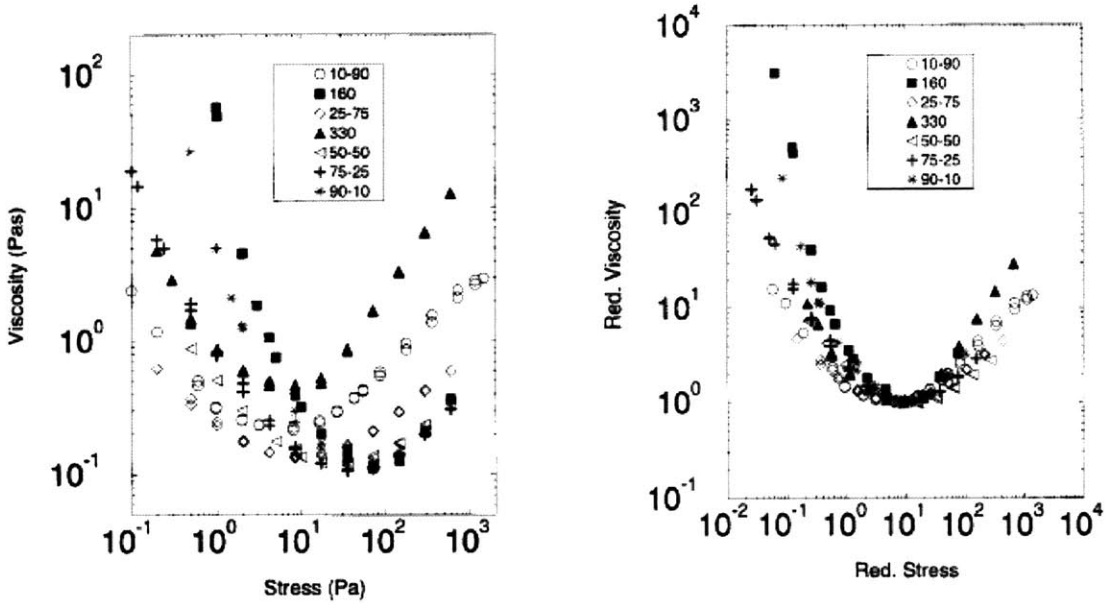

(a) (b)

Figure 2.1.3:(a) Viscosity vs. stress plotted for two monodisperse suspensions and the bimodal mixtures at ϕ =0.64. (b) Reduced viscosity, η/μ, vs. reduced stress $\sigma_{crit}a^3/k_BT$. The labels indicate the mixing of small (160 nm) to large (330 nm) particles by volume percent [8].

Similar scalings can also be obtained for electrostatically stabilized particles in which the electrostatic forces are dominant over Brownian forces. By using the Derjaguin approximation (in the limit of very dense suspensions) of the Poisson-Bolzmann equation [23], we can obtain a relation for the electrostatic forces:

$$F_{electro}(h \rightarrow 0) = 2\pi\varepsilon_0\varepsilon_r\psi_S^2\kappa\, a/2 \tag{2.5}$$

where ε_0 is the permittivity in vacuum, ε_r is the relative permittivity, ψ_S is the potential at the surface, and $1/\kappa$ is the Debye length. The scaling between the two forces then becomes:

$$\tau_{cr}^{elec} = Pe_{cr}^{elec} = \frac{F_{Hydro}}{F_{elec}(h \rightarrow 0)} = \frac{3\pi\mu a^3\,\dot{\gamma}/2h}{2\pi\varepsilon_0\varepsilon_r\psi_S^2\kappa\, a/2} \tag{2.6}$$

An important relation to note is that the dimensionless stress or Peclet number have different dependence on particle size based on the type on interparticle interaction;

in fact, for Brownian particles $\tau_{crit} \sim a^{-3}$, but for electrostatically stabilized particles the critical stress scales as $\tau_{crit} \sim a^{-2}$. The interesting point emerging from this analysis is that, according to this scaling, one can then control the onset of the thickening effect, τ_{crit}, in both ER and STF by varying the particles size, the smaller the particles, the greater τ_{crit}.

2.1.3. Description of the Shear Thickening Phenomenon

The complexity in modeling the rheological behavior of shear-thickening fluids arises from the great number of variables that affect the magnitude of the shear-thickening effect, the onset of it (the critical stress) and the yield-stress of the fluid. Many studies have successfully correlated the effect of some of the key parameters on the fluid rheology and the reviews from Laun [6], Barnes [3] and Powell [2] summarize many of these findings. The rheology of a shear thickening fluid is a function of the particle size, shape and size distribution, the particle density, charge, and roughness, and in some cases the chemical interaction between the particle surface and the carrier fluid. Additionally, as shown in equation (2.4) the onset of the thickening phenomenon is a function of the number of particles present in the fluid (the volume fraction),which affect the average particle distance *h*, the fluid viscosity, and the Brownian energy. In the following sections we will try, when possible, to describe each variable dependence separately.

2.1.3.1. Volume Fraction Dependence

The rheology of shear thickening fluids depends significantly on the volume fraction (ϕ) of the suspension. In order to observe shear-thickening effects the volume fraction needs to be high enough that the particles 'feel' each other's presence, that is, the particle force field and behavior is affected by the presence of surrounding particles. These interparticle forces depend on the particle charge as well as the polarity of the fluid; it is therefore hard to define a critical volume fraction at which shear thickening is observed to occur. As the volume fraction increases we note three different trends in the rheology of the suspension (Figure 2.1.4)

1. An increase in the overall viscosity as volume fraction is increased.
2. A shift of the critical stress or critical shear rate, $\dot{\gamma}_{crit}$ at which shear thickening occurs; as ϕ increases the critical stress decreases.
3. An increase in the magnitude of the viscosity jump as the volume fraction increases.

The increase in viscosity with volume fraction is expected, and for the case of dilute suspensions, this dependence has been known and studied extensively. As first introduced by Einstein and then extended by Batchelor [24], the viscosity relation for hard spheres suspensions follows the relation:

$$\eta = \eta_s \left(1 + 2.5\phi + 6.2\phi^2 + O\left(\phi^3\right) + ...\right) \tag{2.7}$$

where the first order term in ϕ represents the contribution from viscous dissipation of single spheres in fluids, the second order term is the contribution from two-particles hydrodynamic interactions, the third order term comes from three-body hydrodynamic interaction, and so on.

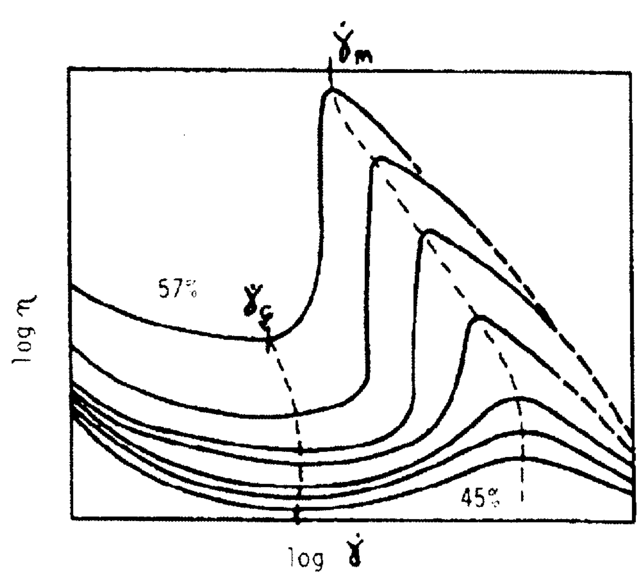

Figure 2.1.4 Schematic representative of viscosity versus shear rate for shear-thickening systems, with approximate phase volume as parameter. Also shown are the loci of $\dot{\gamma}_c$ and $\dot{\gamma}_m$, the shear rates at the beginning and the end of the shear thickening region. [3]

An attempt to extend Batchelor result of equation (2.7) for higher volume fractions resulted in the Krieger-Dougherty equation [21]:

$$\eta = \eta_s \left(1 - \frac{\phi}{\phi_m}\right)^{-[\eta]\phi_m} \tag{2.8}$$

where $[\eta]$ is the intrinsic viscosity, η_s is the solvent viscosity and ϕ_m is the maximum packing volume fraction. Equation (2.8) is a general empirical expression for suspensions of particles of spherical or other shape. The experimental values for $[\eta]$ and ϕ_m for a variety of particles shape have been tabulated by Barnes [25]. At high volume fractions the relation becomes more complex and even small changes in volume fraction result in large variation of viscosities. Additionally, at very high ϕ the viscosity becomes extremely sensitive to the roughness inhomogeneity, shape of the particles [21].

It has also been shown that critical stress for the onset of shear-thickening decreases with increasing ϕ. This means that if the number of particles in suspension decreases, and therefore they are farther apart from each other, one needs to impose a greater stress to increase the size of the hydrocluster and therefore achieve the thickening of the suspension. This change in critical stress is not linear in ϕ; by comparing and analyzing the rheological data from different authors, Barnes [3] has shown that the rate of change in the critical shear stress, τ_{crit}, is very high at lower ϕ (below $\approx$ 45%) then plateaus around 50 %, where particles are very close to each other and it is easy to form hydroclusters. The rate of change in the critical shear stress changes rapidly also at ϕ greater than 50% where the suspension is in the closed packed limit and it is in a jammed glassy solid state. This is illustrated in Figure 2.1.5.

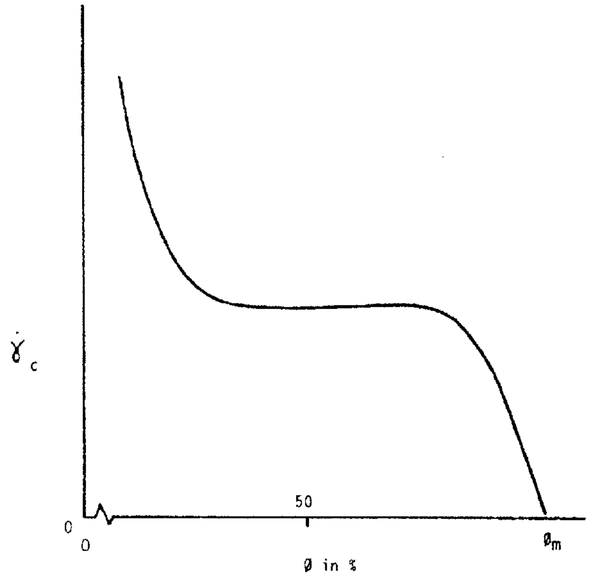

Figure 2.1.5 Schematic of the dependence of critical shear rate for the onset of shear thickening ($\dot{\gamma}_c$) as a function of the phase volume of the disperse phase (ϕ)[3]

2.1.3.2. Particle Size Dependence

Many studies have focused on the particle size dependence of suspension rheology and on the prediction of the critical stress. Barnes [3] and also Hoffman [5] reported tables with a summary of some of these studies of the type and size of particles together with the value of critical stress. For completeness one of these table is shown in Table 2.1.1; the values of particles sized varied between 27 nm to 200 μm, while the corresponding critical shear rates varied between $5x10^{-3}$ to $1.5x10^{4}$ s^{-1}.

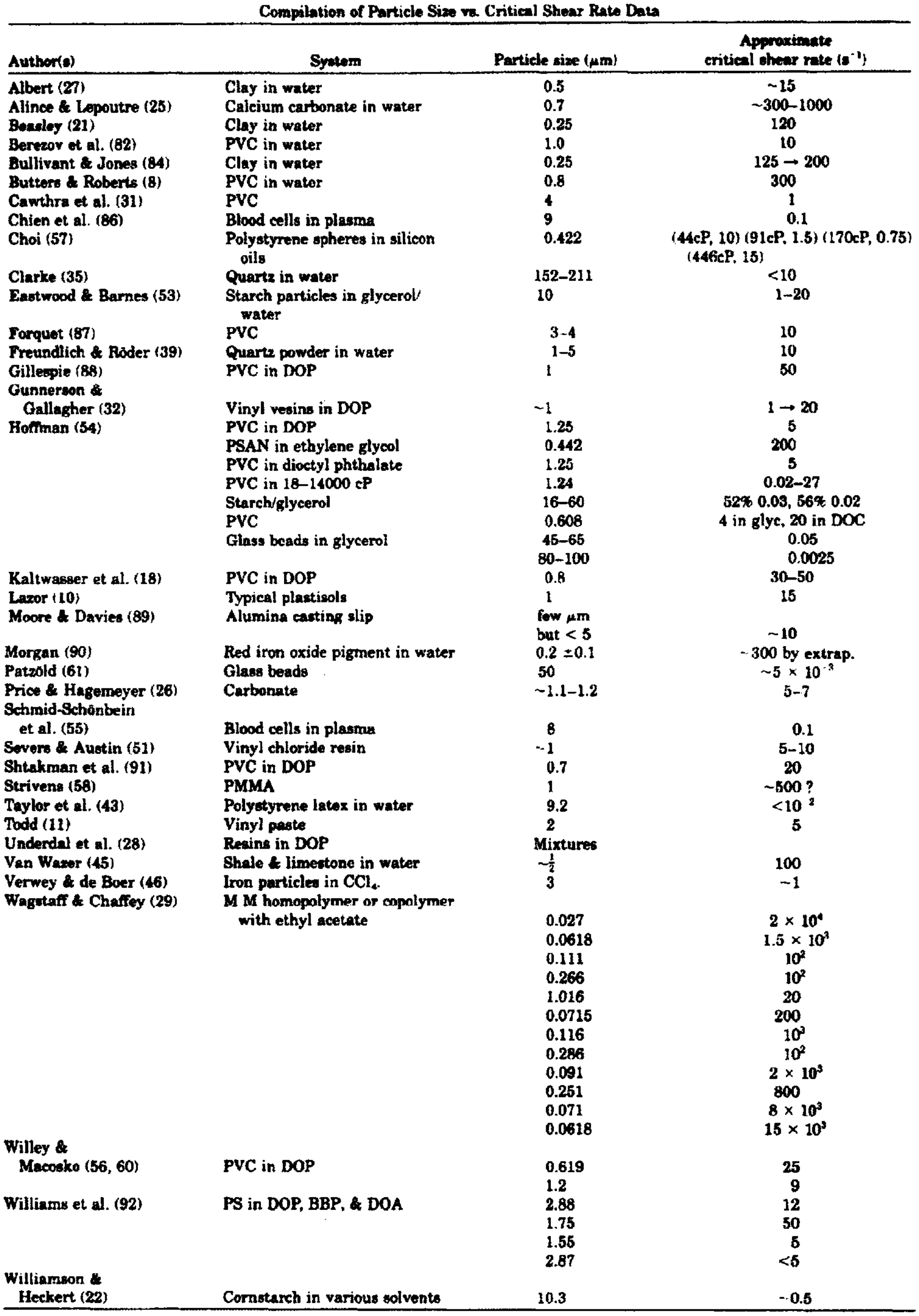

Compilation of Particle Size vs. Critical Shear Rate Data

Author(s)	System	Particle size (μm)	Approximate critical shear rate (s^{-1})
Albert (27)	Clay in water	0.5	~15
Alince & Lepoutre (25)	Calcium carbonate in water	0.7	~300–1000
Beasley (21)	Clay in water	0.25	120
Berezov et al. (82)	PVC in water	1.0	10
Bullivant & Jones (84)	Clay in water	0.25	125 → 200
Butters & Roberts (8)	PVC in water	0.8	300
Cawthra et al. (31)	PVC	4	1
Chien et al. (86)	Blood cells in plasma	9	0.1
Choi (57)	Polystyrene spheres in silicon oils	0.422	(44cP, 10) (91cP, 1.5) (170cP, 0.75) (446cP, 15)
Clarke (35)	Quartz in water	152–211	<10
Eastwood & Barnes (53)	Starch particles in glycerol/ water	10	1–20
Forquet (87)	PVC	3–4	10
Freundlich & Röder (39)	Quartz powder in water	1–5	10
Gillespie (88)	PVC in DOP	1	50
Gunnerson & Gallagher (32)	Vinyl vesins in DOP	~1	1 → 20
Hoffman (54)	PVC in DOP	1.25	5
	PSAN in ethylene glycol	0.442	200
	PVC in dioctyl phthalate	1.25	5
	PVC in 18–14000 cP	1.24	0.02–27
	Starch/glycerol	16–60	52% 0.03, 56% 0.02
	PVC	0.608	4 in glyc, 20 in DOC
	Glass beads in glycerol	45–65	0.05
		80–100	0.0025
Kaltwasser et al. (18)	PVC in DOP	0.8	30–50
Lazor (10)	Typical plastisols	1	15
Moore & Davies (89)	Alumina casting slip	few μm but < 5	~10
Morgan (90)	Red iron oxide pigment in water	0.2 ±0.1	~300 by extrap.
Patzöld (61)	Glass beads	50	$\sim 5 \times 10^{-3}$
Price & Hagemeyer (26)	Carbonate	~1.1–1.2	5–7
Schmid-Schönbein et al. (55)	Blood cells in plasma	8	0.1
Severs & Austin (51)	Vinyl chloride resin	~1	5–10
Shtakman et al. (91)	PVC in DOP	0.7	20
Strivens (58)	PMMA	1	~500 ?
Taylor et al. (43)	Polystyrene latex in water	9.2	$<10^{2}$
Todd (11)	Vinyl paste	2	5
Underdal et al. (28)	Resins in DOP	Mixtures	
Van Wazer (45)	Shale & limestone in water	$\sim\frac{1}{2}$	100
Verwey & de Boer (46)	Iron particles in CCl_4.	3	~1
Wagstaff & Chaffey (29)	M M homopolymer or copolymer with ethyl acetate	0.027	2×10^{4}
		0.0618	1.5×10^{3}
		0.111	10^{2}
		0.266	10^{2}
		1.016	20
		0.0715	200
		0.116	10^{3}
		0.286	10^{2}
		0.091	2×10^{3}
		0.251	800
		0.071	8×10^{3}
		0.0618	15×10^{3}
Willey & Macosko (56, 60)	PVC in DOP	0.619	25
		1.2	9
Williams et al. (92)	PS in DOP, BBP, & DOA	2.88	12
		1.75	50
		1.55	5
		2.87	<5
Williamson & Heckert (22)	Cornstarch in various solvents	10.3	~0.5

Table 2.1.1 Comparison of particle size vs. critical shear rate for a number of studies [3]

According to the scaling model presented in earlier in Equation (2.3) and equation (2.6), we would expect that for monodisperse spherical particles, the critical shear stress be proportional to a^{-2} for electrostatically stabilized particles and a^{-3} for Brownian suspension.

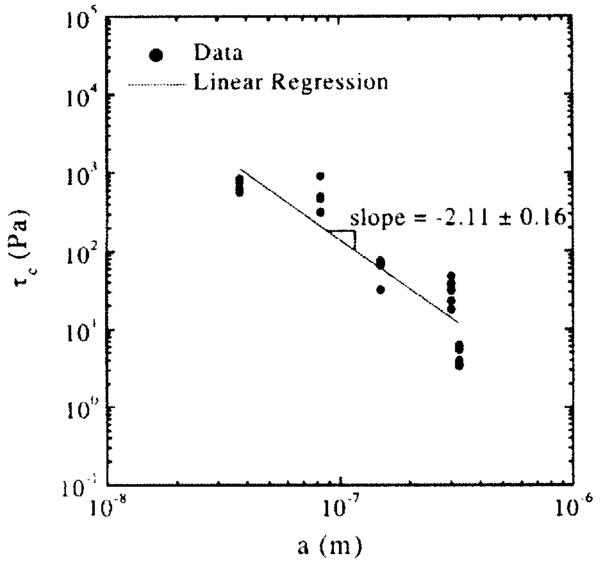

Figure 2.1.6: Critical shear stress plotted against particle radius for monodisperse silica particles. The line is a power law regression with slope of –2.11±0.16. [10]

These scalings have been confirmed through experimental results from Wagner, at least for electrically stabilized particles, as illustrated in Figure 2.1.6. Barnes [3] has also shown this relation by comparing the work of many authors in his review (see Figure 2.1.7) and also found a relation of a^{-2}. His data is more scattered because a collection of work of many authors with different 'controlled conditions', as the charge and chemistry of the particles, solvent viscosity etc., can all affect the critical stress.

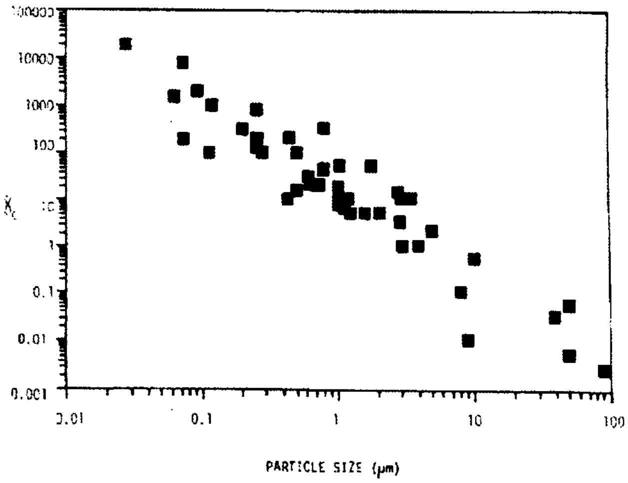

Figure 2.1.7 Critical shear rate as a function of average particle size.[3]

This finding is of particular interest from a design and application point of view. In fact, this allows one to 'tune' the shear-thickening fluid, in order to select the appropriate critical stress, for the intended application by choosing the right particle size.

2.1.3.3. Particle Size Distribution Dependence

The particle size distribution of the particles in suspension also affects the maximum value of volume fraction, ϕ_m. If the particles are of different size they can pack more efficiently because smaller particles can fit within the voids between the larger particles; which allows for greater volume fractions. If comparing two different suspensions with the same volume fraction, but one with monodisperse and the other polydisperse particles, the monodisperse suspension will show a stronger shear thickening effect at a lower critical stress[3]. This again relates to the fact that polydisperse suspensions pack more efficiently and particles (at constant ϕ) are therefore farther apart from each other. Consequently, the broader the particle size distribution, the higher the critical shear stress and less severe the shear thickening [3].

Particular attention has also been given to bimodal suspensions and their rheology. Some early work on the dependence of size ratio carried out by Wagstaff & Chaffey [26] has shown that a size ratio of 4 to 1 or greater, greatly reduces the shear thickening of the suspension. Additionally, Bender and Wagner [8] showed that they were able to control, and increase the critical stress by increasing the ratio of small to large particles. The particles used in this study were monodisperse silica spheres, which were electrostatically stabilized. Similar results, but for sterically stabilized particles were presented by D'Haene [27].

2.1.3.4. Particle Shape Dependence

The shape of particles in a suspension has also a great impact on the resulting rheology. In fact, non-spherical particles tend to align with the flow field and show much greater elastic effect, including normal stress differences, that spherical particles suspensions [21].

Suspensions of anisotropic particles also exhibits non-Newtonian behavior, as shear thinning at relatively low ϕ, compare to the one for spherical particles suspensions; in fact spherical particles suspensions start to exhibit shear thinning behavior at volume fractions $\phi > 30\%$.

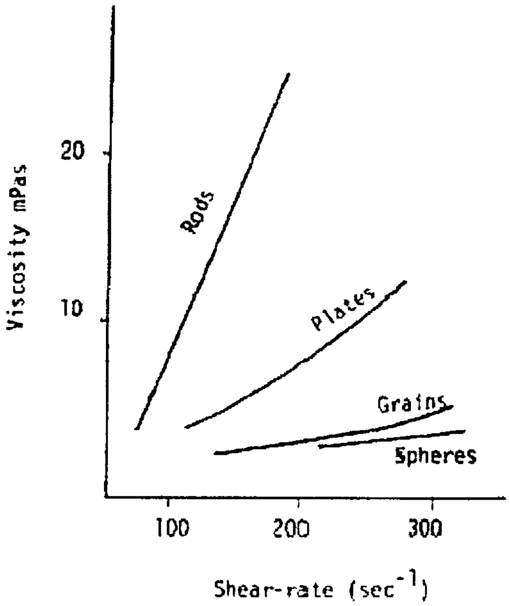

Figure 2.1.8: The effect of particle shape on shear thickening at volume fraction of 20% [3]

For high volume fraction suspensions there is no complete, quantitative studies on the effect of particle shape on suspension rheology, but some qualitative studies have been conducted. As Barnes notes in his review article, the rheology of suspensions of anisotropic particles shows a smaller critical stresses for the onset shear thickening and the thickening is also observable at lower volume fractions than for spherical particles suspensions. Figure 2.1.8 illustrates an example of the rheological behavior of suspensions made of different shapes particles at a constant volume fraction of 20%.

Egres [28] also presented some work on acicular precipitated calcium carbonate particles and showed that increase in particles aspect ratio (in ratio that ranged between 2-7) enhances the shear thickening effect that can be observed at much lower volume fraction than for spherical particles.

2.1.3.5. Particle-Particle Interaction Dependence

Interparticle interactions are extremely important in determining the shear thickening response of a suspension. Flocculated suspensions will not show any shear thickening [3], but instead they will exhibit shear thinning, as shown schematically in Figure 2.1.9.

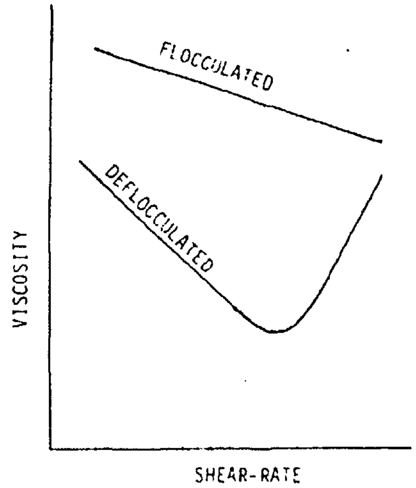

Figure 2.1.9: Schematic representation of the effect of chemically induced flocculation on shear thickening. [3]

To observe shear thickening, the particles in the suspension need to be neutral (or what is commonly referred as Brownian or hard spheres) or repel each other (electrostatically charged particles) as seen in the scaling presented in section 2.1.2.3. Suspensions of hard spheres tend to show less severe shear thickening if compared to electrostatically charged particles. Figure 2.1.10 illustrates the different rheological responses of silica particles with and without a surface charge; the higher the surface charge the more severe the shear-thickening effect is found to be.

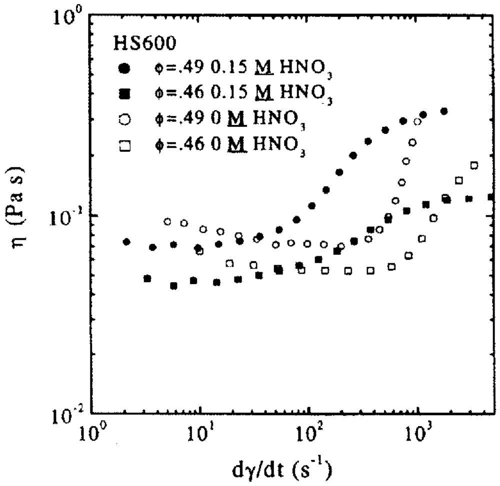

Figure 2.1.10: Comparison of viscosity data between a dispersion of 600 nm silica particles with 0.066 M HNO_3 and 0 M HNO_3 plotted against applied shear rate [29].

This effect is due principally to the fact the surface charge or grafted layer of polymers (for sterically stabilized particles) on the particles surface, does not allow particles to get too close to each other. This can be viewed as having particles with effective size $a+\Delta$, where a is the particle radius and Δ is the thickness of the layer. This varies the effective volume fraction which can then be expressed as:

$$\phi = \phi_0 \left(1 + \frac{\Delta}{a}\right)^3 \tag{2.9}$$

where ϕ_0 is the volume fraction of the hard spheres. In principle by increasing the particle charge or polymer layer thickness the effective volume fraction increases and the shear thickening effect can be augmented at lower nominal volume fractions.

2.1.3.6. Dependence on the Viscosity of Carrier Fluid

As described by Batchelor expression, equation (2.7), and then extended for higher volume fraction by the Krieger-Dougherty equation (2.8) the viscosity of a shear-thickening suspension is directly related to the viscosity of the carrier fluid. “All things being equal, doubling the continuous phase viscosity doubles the suspension viscosity" [3]. This is also supported by the scaling model presented in section 2.1.2.3, where, in both cases (electrostatically stabilized or Brownian particles) the Peclet number depends linearly on the background viscosity.

Some difficulty arises from obtaining exact experimental measurements of the effect of solvent viscosity due to the fact that changing solvents also affects the interparticle interactions and it may be difficult to separate the two effects. Heating has been used to test the dependence of the shear-thickening effect on the carrier fluid viscosity, but particular attention needs to be given to the effect of particle swelling and the effect of the particle Brownian energy increase [3].

2.1.4. Rheology of Shear Thickening Fluids

2.1.4.1. Steady shear rheology

As described earlier in this chapter the steady state rheology of a shear thickening suspension is characterized by a shear thinning region at low stresses followed by shear thickening (see Figure 2.1.1) and the details of the rheology are influenced by the suspension volume fraction and particle characteristics. These results are representative of the equilibrium structure that forms under shear stress, but do not illustrate any of the time dependent response of the suspension.

2.1.4.2. Dynamic Shear rheology

Only recently [6, 30, 31] authors have began to study the dynamic response of shear-thickening fluids. Small-amplitude oscillatory shear is applied to the sample where the strains and strain rates are of the following forms:

$$\begin{aligned}\gamma(t) &= \gamma_0 \sin(\omega t) \\ \dot{\gamma}(t) &= \omega\gamma_0 \cos(\omega t)\end{aligned} \tag{2.10}$$

where γ_0 is the strain magnitude and w is the frequency. The material response can then be separated into two parts: one that is in phase with the strain, generally called storage modulus $G'(w)$, and one in phase with the strain rate $G''(w)$, generally called loss modulus as follows:

$$\sigma(t) = \gamma_0\left[G'(w)\sin(wt) + G''(w)\cos(wt)\right] \tag{2.11}$$

The storage and loss modulus can be written in term of viscosity as:

$$\eta' = \frac{G''}{w} \qquad \eta'' = \frac{G'}{w} \tag{2.12}$$

and the complex viscosity is then defined as:

$$\begin{aligned}\eta^* &= \eta' - i\eta'' \\ |\eta^*| &= \sqrt{\left(\eta'^2 + \eta''^2\right)}\end{aligned} \tag{2.13}$$

Under dynamic loading the complex viscosity of these concentrated suspensions increases at a critical combination of $\omega\gamma_0$, which is referred as strain-thickening. Their viscoelastic response can be used to estimate the suspension relaxation time and also the minimum strain requirements to initiate shear thickening. Some controversy in the applicability of the modified Cox-Merz rule or Delaware-Rutgers rule [32] for dense suspension is still ongoing. This rule relates the steady state viscosity to the dynamic fluid response as follows:

$$\left|\eta^*(\omega\gamma_0)\right| = \eta(\dot{\gamma})\Big|_{\dot{\gamma}=\omega\gamma_0} \tag{2.14}$$

where η^* is the complex viscosity, ω is the oscillation frequency, γ_0 is the oscillation maximum strain, η the steady state viscosity, and $\dot{\gamma}$ the steady state shear rate.

Ragavan and Khan [30] have shown that for their fumed silica suspension of ϕ that varied between 3 %-10%), the modified Cox-Merz rule applies (see Figure 2.1.11), while Wagner [31] has argued that the dynamic and steady response should superimpose (follow the Delaware-Rutgers) only in the shear thinning regions and should not apply in the highly non-linear shear thickening regime; this agrees with their experimental data shown in Figure 2.1.12.

It has also been suggested [6, 30] that there is a minimum strain of order 1 below which shear thickening does not occur (independently of the frequency of oscillation). This is consistent with the idea that one needs to move the particle at least past each other (a distance on the order of the particle size for the case of high volume fraction) in order to see shear thickening. Some authors [31] do not agree and have suggested that the trend in experimental data can be explained by slip.

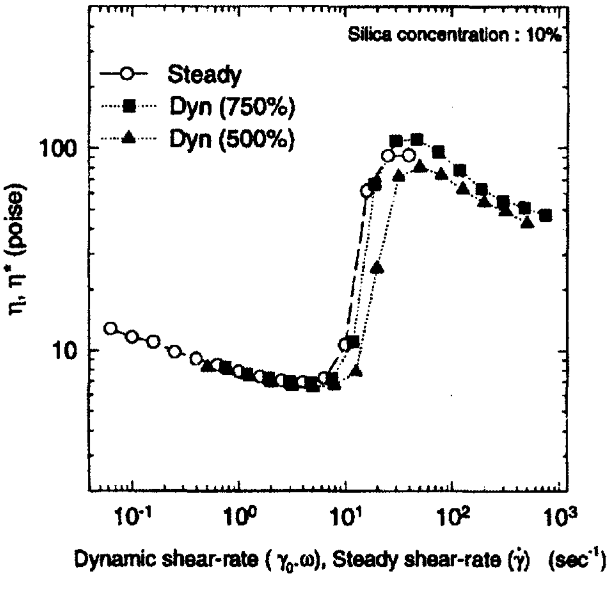

Figure 2.1.11: Comparison of steady and dynamic data for a 10% fumed silica suspension. Here, the complex viscosity η^* is plotted against the maximum dynamic shear rate $\omega\gamma_0$, where γ_0 is the appropriate strain amplitude in the frequency sweep [30].

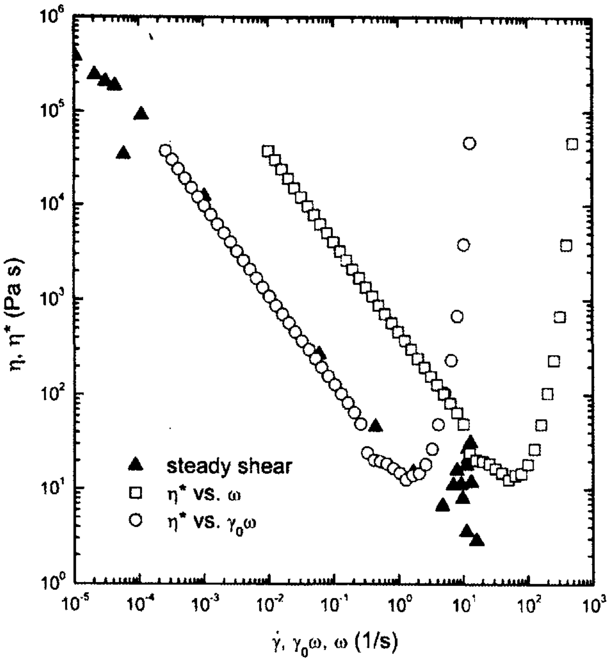

Figure 2.1.12: Application of the Cox-Merz and Delaware-Rutgers rules for 60 vol. % aqueous silica dispersion [31]. The dynamic shear data superimposed to the steady shear data only in the shear thinning region and not in the shear thickening one.

2.1.4.3. Extensional rheology

The extensional behavior of concentrated suspensions is an aspect of their rheology that has not been explored. Measuring the transient extensional flow rheology is a very active field in polymer solution, but very limited experimental work has been done on concentrated suspensions. Numerical simulations have been carried out by Sami [33] on dense suspensions and have shown that the planar extensional viscosity of these fluids relate to the shear viscosity as follows:

$$\eta_e\left(Pe_e\right) = 4\eta_s\left(\sqrt{2}Pe_s\right) \tag{2.15}$$

where *Pe* is the Peclet number defined as the ratio between hydrodynamic and Brownian forces, 4 is the equivalent Trouton ration for planar extension and $\sqrt{2}$ is the prefactor for the strain rate scalar invariant in planar extension; this is illustrated in Figure 2.1.13.

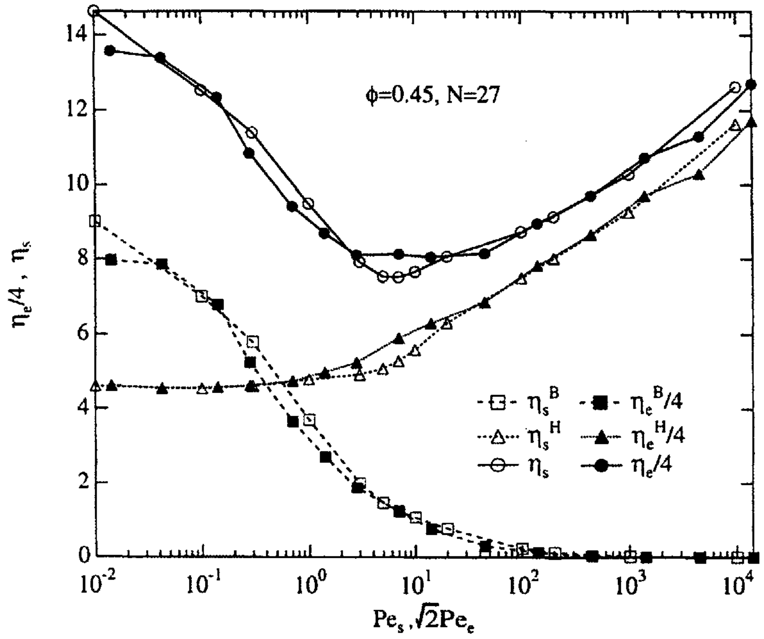

Figure 2.1.13: Shear and extensional viscosity plotted against Peclet number. Open symbols refer to shear viscosities while full symbols to extensional viscosities. Plotted are also the hydrodynamic and Brownian contributions of these viscosities as a function of Pe. [33]

2.1.5. Applications

The rheological response of shear thickening fluids to an imposed stress and the associated energy absorption capability make them very good candidates for composite materials for human protection applications. In fact, they can absorb energy through the mechanism of viscous dissipation and during their thickening transition. Additionally, they can remain at low viscosity and therefore they can be flexible during normal operation and thicken when needed. These fluids are particularly interesting because they do not require an external activation mechanism, as magneto-rheological or electro-rheological fluids do, rather they 'self-activate' under stress. A number of authors have tried to exploit the mechanical and rheological property of such fluids in ingenious ways; a few examples are highlighted below.

2.1.5.1. Hip Padding

One of the first proposed applications of shear-thickening fluids was a hip-protection garment patented by Hayes and Robinovitch [34]. This specific design consisted of a series of pouches filled with shear-thickening fluids which formed a sheet that can be inserted in a garment (see Figure 2.1.14). The final product is flexible and comfortable to wear under normal circumstances, but hard and energy absorbent in the case of a fall (or high imposed stress).

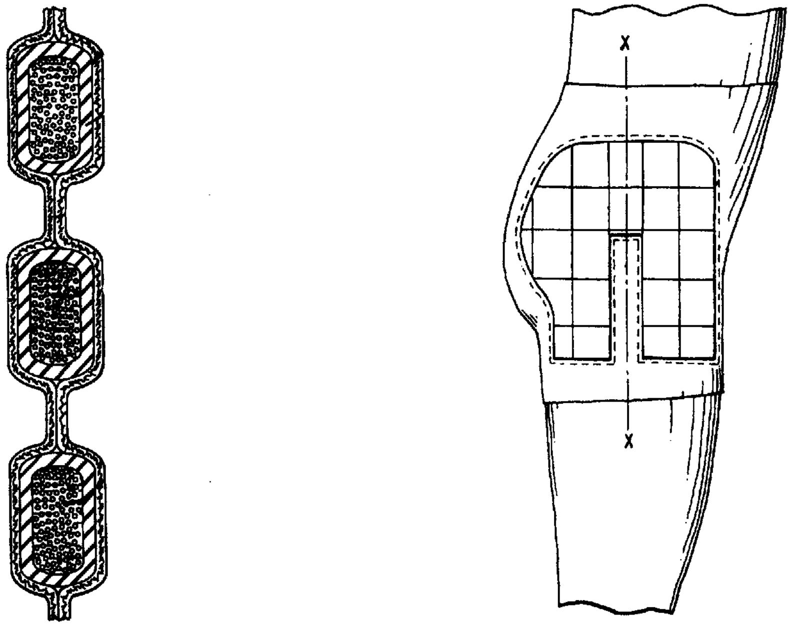

(a) (b)

Figure 2.1.14(a) Schematic of pouches filled with shear thickening fluid. (b) Garment made of shear-thickening filled pouches.

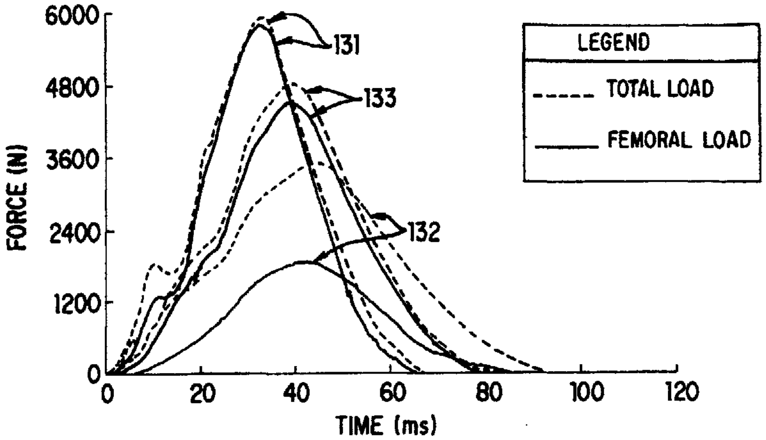

Figure 2.1.15: Plots of Load vs. Time for three different impacts. The broken line represent the total load, the solid line the load experience by the femur. Impact 131 refers to impact to unpadded surrogate pelvis, 132 impact after affixing a pelvis device according to U.S. patent 4,573,216, and 133 impact to surrogate pelvis protected by with shear thickening fluid composed garment [34].

Experimental results of impact tests have shown that the garment is able to reduce the femoral load to about 50 % of its total load by dissipating the impact energy though the shear-thickening of the fluid.. Figure 2.1.15 illustrates the force resultant for impacts on surrogate pelvis. The highest load is seen for number 131 which refers to the impact of unpadded surrogate pelvis, while number 133 refers to the STF based garment presented.

2.1.5.2. Ballistic Protection

One of the most recent applications for these fluids was presented by Wetzel and Wagner [31] who incorporated a shear thickening fluid in a multilayer composite for use as a body armor for ballistic protection. Their composite was made of multiple layers of Kevlar sheets impregnated in shear thickening fluid. Ballistic testing on these multilayer structures showed that the ballistic penetration resistance was enhanced by the presence of STF impregnated Kevlar, as compared to Kevlar or shear thickening fluid alone. This effect is shown in Figure 2.1.16 where two clay witnesses, made from modeling clay confined into a mold and then compressed with a mallet, are shown after been impacted by a bullet. The clay witness shown in Figure 2.1.16(a) was protected by a pouch of shear thickening fluids and four layers of Kevlar while the one in Figure 2.1.16(b) was protected by 4 layers of Kevlar all impregnated with shear thickening fluid. This illustrates that impregnating the layers of Kevlar with STF offers much more ballistic protection.

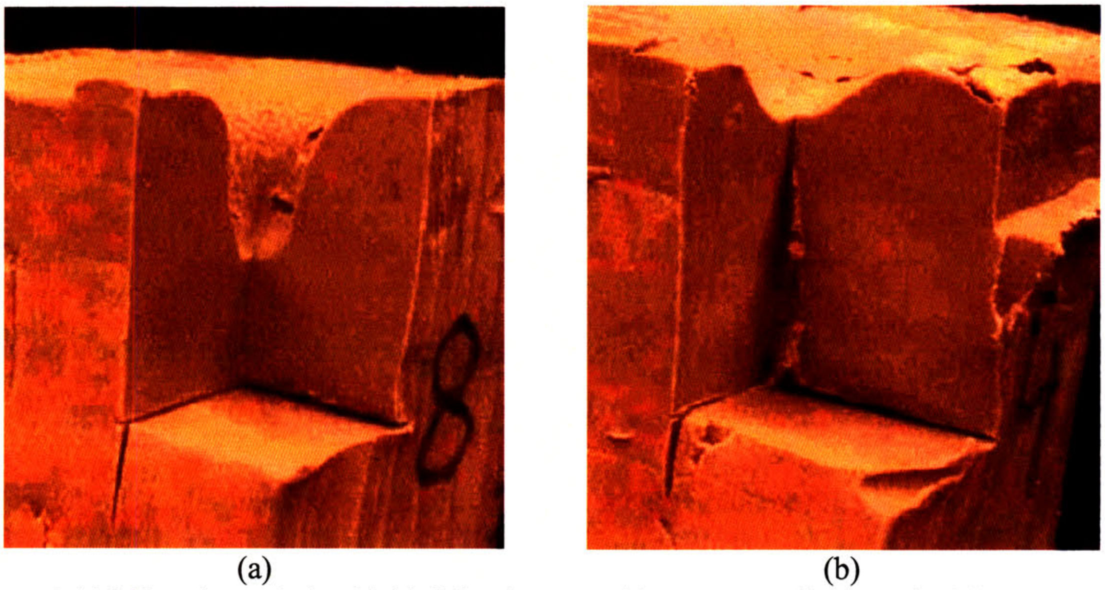

(a) (b)

Figure 2.1.16 Clay witnessed placed behind shooting target. (a) was protected by a pouch of shear thickening fluids and four layers of Kevlar , (b) was protected by 4 layers of Kevlar all impregnated with shear thickening fluid [31].

2.2. Cellular Solids: Review

Cellular solids are assemblies of cells with solid edges and faces packed together so that they fill space [35]. When the structure of these cellular materials is made of parallel, prismatic cells, which form a two-dimensional structure, they are called honeycombs. Example of honeycomb structures can be found in nature in bee's honeycombs and cork. When the cells are polyhedra and therefore form a three-dimensional structure, they are called foams; examples of foams include sponges, cancellous bones, corals, breads etc.

2.2.1. Structure and Properties of Cellular Solids

2.2.1.1. Cell Structure

The shape and structure of a cell is of particular importance because it directly affects the material properties of the resulting foam. Honeycomb two-dimensional structures are made of parallel, prismatic cells; most cells are hexagonal, but square, triangular or random cells can also be made, see Figure 2.2.1.

Foams on the other hand can be classified as open-cell or closed-cell. In the case of open-cell foam the solid material is concentrated into struts that form the cell edges. For the case of closed-cell, a thin film of the material is also present in each cell wall. The difference in structure between these two types of foams is also illustrated in Figure 2.2.2.

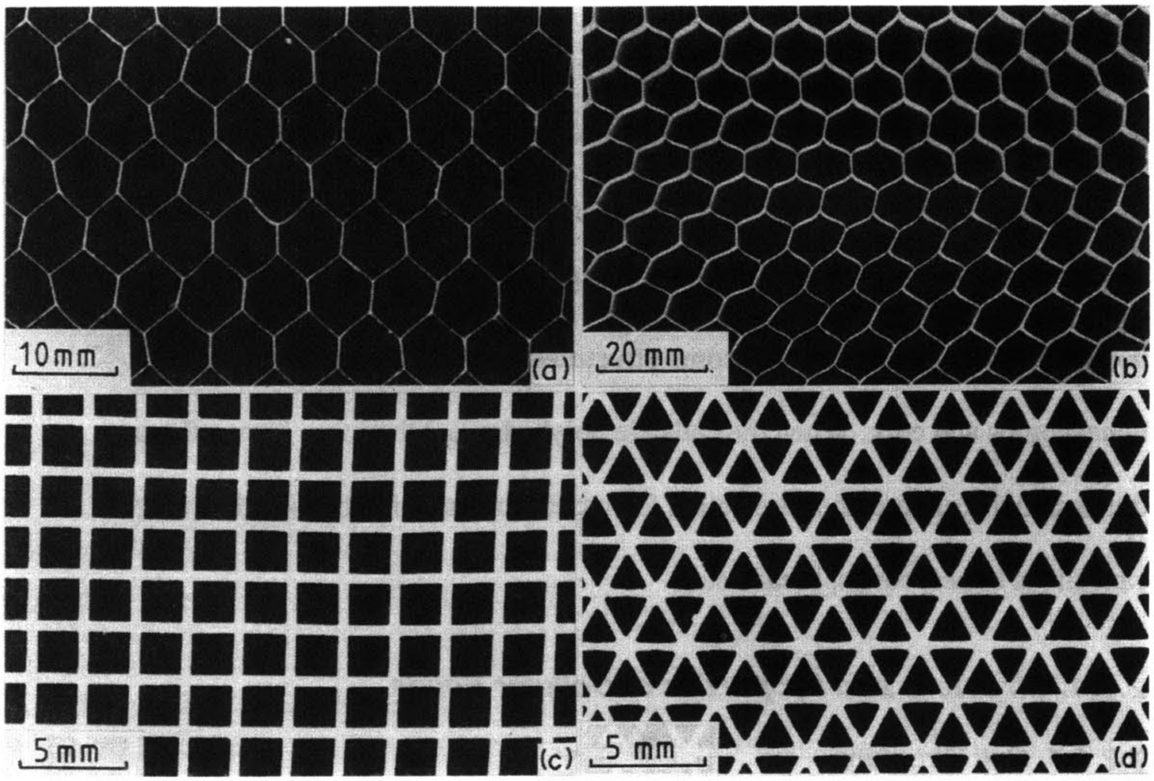

Figure 2.2.1:Two-dimensional cellular material: (a) aluminum honeycomb, (b) paper-phenolic resin honeycomb, (c) ceramic honeycomb with square cells, (d) ceramic honeycomb with triangular cells [35].

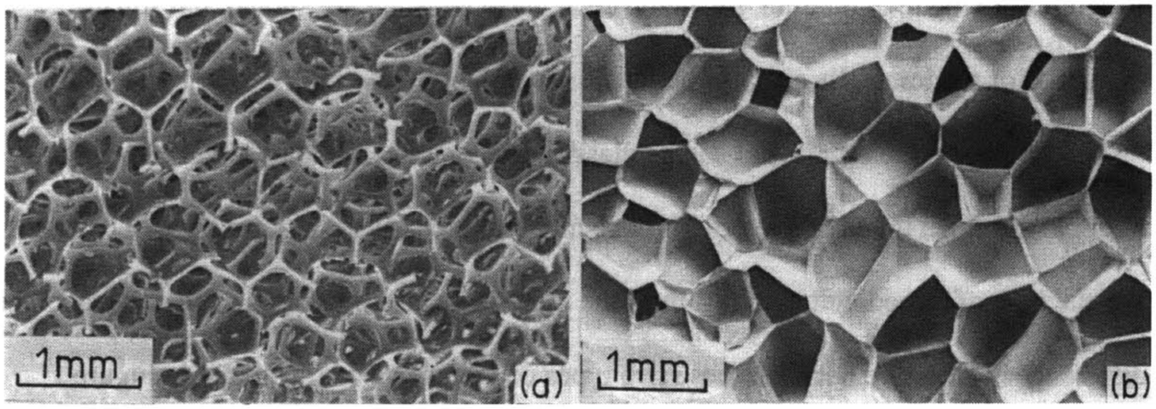

Figure 2.2.2: Three-dimensional cellular material: (a) open-cell polyurethane foam, (b) closed-cell polyurethane foam [35].

2.2.1.2. Properties of Cellular Solids

"The mechanical response of…foam is controlled by the way in which cell elements behave cooperatively under localized strain…" [36]. The material property of foams depends on at least two factors: the geometry of their structures and the properties of the material they are composed of.

The most important structural characteristic of a foam is its relative density, which is defined as (ρ*/ρs) , where ρ* is the density of the cellular material, and ρs is the density of the solid from which the foam is made. The cell size and shape can be related to the relative density, but the relation varies depending on the type of foam, open or closed cell. If we define the cell edge l and the cell wall thickness t as seen in Figure 2.2.3, then the relation between relative density and cell size can be expressed as

$$\frac{\rho^*}{\rho_S} = C\left(\frac{t}{l}\right)^n \tag{2.16}$$

where n = 2 for open-cell foam and n = 1 for honeycombs and closed-cell foams. The constant C depends on the shape of the cell and is of order 1 [35].

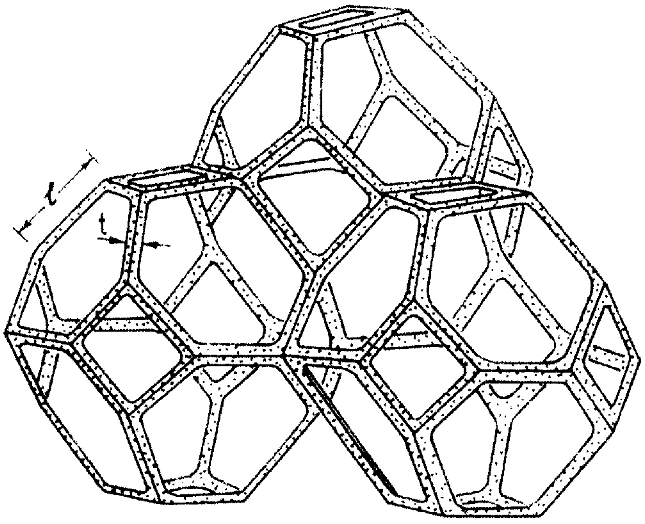

Figure 2.2.3: The packing of polyhedra to fill space: kaidecahedra [35].

Another characteristic of foam is its porosity, the fraction of open space, which is simply defined as $1-\left(\rho^{*}/\rho_{s}\right)$.

The cell shape is also important because it is related to the isotropy or anisotropy of the foam. Random shaped cells will result in foams that have isotropic material properties as, for example, polymeric foams. Elongated cells instead result in highly anisotropic material properties as in wood or cancellous bone [35].

Additionally, as one would expect, the material properties of the foam also to depend on the material properties of the solid from which the foam is made, such as its density ρ_s, Young's modulus E_s, and plastic yield strength, σ_{ys}. Constitutive models for the mechanical properties are discussed below.

2.2.2. Mechanics of foam

We focus our attention on three-dimensional foams because they are more suited for our intended energy absorption application. Most man-made foams are used for energy absorption for impacts or for the construction of lightweight materials, additionally they are widely used as thermal insulators, in the construction of floating devices and as filters. Because of their widespread use, the mechanics of foams have been well studied and documented.

2.2.2.1. Mechanics of Foam Compression

The material response of a typical elastomeric foam is characterized by an initial linear regime followed by a long plateau which ends in a densification region. This is illustrated schematically in Figure 2.2.4.

The initial linear regime is associated with the bending of the cell wall and characterized by a modulus E^*. By modeling the open cell wall as a cubic array, a simple scaling to relate the modules E^*, $G^*$and v^* to the relative density of the foam can be derived:

$$\frac{E^*}{E_S} = C_1\left(\frac{\rho^*}{\rho_S}\right)^2 \tag{2.17}$$

$$\frac{G^*}{E_S} = C_2\left(\frac{\rho^*}{\rho_S}\right)^2 \tag{2.18}$$

$$v^* = C_3 \tag{2.19}$$

Details of this model and scaling arguments can be found in Ashby and Gibson [35]. By comparing the scaling with experimental data it is found that for open cell foam $C_1 \approx 1$, $C_2 \approx 3/8$, $C_3 \approx 1/3$. A detailed discussion of a micromechanical model for open cell foam can be found in Hilyard and Cunningham [36].

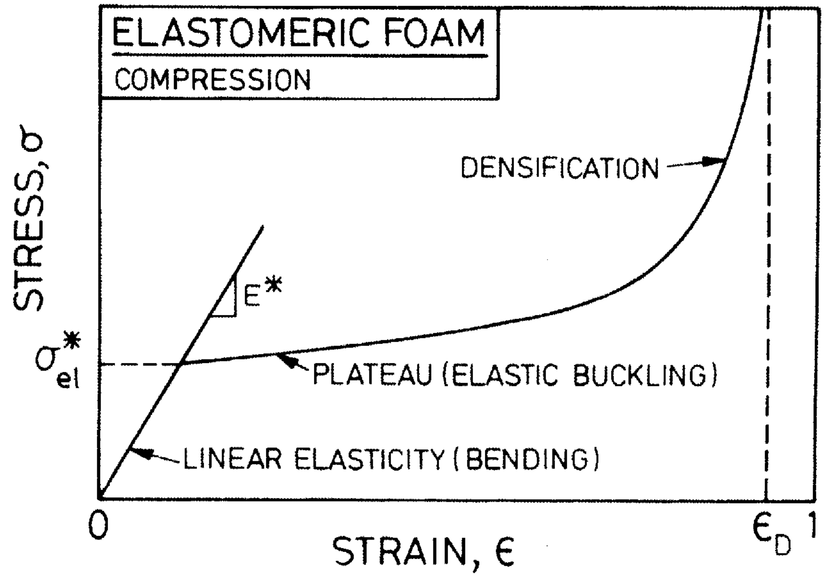

Figure 2.2.4: Schematic compressive stress-strain curves for foams, showing the three regimes of linear elasticity, collapse and densification for an elastomeric foam [35].

Following the elastic region the stress-strain curve flattens into a plateau at a stress σ_{el}^{*} called the elastic collapse stress which, as the word suggests, is associated with the progressive collapse of the cellular structure. This value of stress is particularly important because it is in the region where most of the energy absorption occurs. Following similar scaling arguments as those developed for the modulus, we can derive a relation between the elastic collapse stress σ_{el}^{*} and the relative density as follows:

$$\frac{\sigma_{el}^{*}}{E_S} = C_4\left(\frac{\rho^{*}}{\rho_S}\right)^2\left(1+\left(\frac{\rho^{*}}{\rho_S}\right)^{1/2}\right)^2 \tag{2.20}$$

Again, if comparing the prediction with actual data for open cell foam $C_4 \approx 0.03$ was found [35].

As the foam is collapsed the cell walls are brought closer and closer together until the cells are crushed together. At this strain, usually denominated ε_D, densification strain, the stress rapidly increases approaching E_S, the modulus of the solid material. The densification strain is not exactly the porosity of the foam as one may expect, see Figure 2.2.5(d), but from experimental results was found it to be

$$\varepsilon_D = 1 - 1.4\left(\frac{\rho^{*}}{\rho_S}\right) \tag{2.21}$$

A schematic of the foam microstructure at the various states of compression is illustrated in Figure 2.2.5.

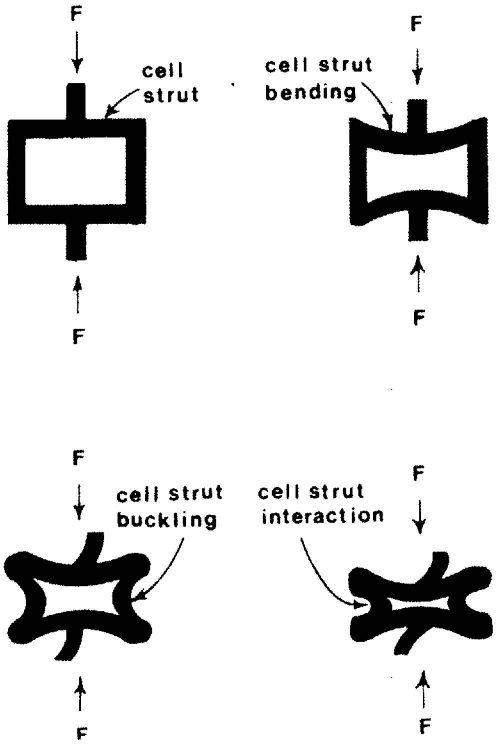

Figure 2.2.5: Schematic representation of the deformation of the cell struts at different levels of the compression, (a) F=0, (b) bending of strut element in the elastic regime (c) buckling of struts normal to the force, (d) interaction of cell struts at densification. [36]

2.2.2.2. Fluid-Filled Open Cell Foam

When foams are filled with a viscous fluid their material properties are, as expected, affected by the presence of the fluid. As the foam is compressed the fluid is squeezed out, and the additional stress contribution is proportional to the viscosity of the fluid. Additionally, the presence of the fluid adds a greater strain rate dependence on the fluid-solid material properties. A relationship between the fluid stress contribution and the material properties can be derived [35] by treating the foam as a porous medium. According to Darcy's law:

$$v = \frac{K}{\mu}\frac{dp}{dx} \qquad (2.22)$$

where v is the velocity of the fluid, μ is the fluid viscosity and dp/dx the pressure gradient. From the geometry in Figure 2.2.6 (unconstrained compression), we can estimate the fluid flux through the vertical faces of the foam

$$q = \frac{VL}{2H} = \frac{\dot{\varepsilon}L}{2} \tag{2.23}$$

where $\dot{\varepsilon}$ is the strain rate defined as:

$$\dot{\varepsilon} = \frac{V}{l} \tag{2.24}$$

By substituting (2.23) into Darcy's law, and making some estimates about K and dp/dx we arrive to the final relation:

$$\sigma_f^* = \frac{C\mu\dot{\varepsilon}}{1-\varepsilon}\left(\frac{L}{l}\right)^2 \tag{2.25}$$

where C is a geometric constant of order unity, ε is the strain, l is the cell-edge length. The total stress in the plateau region for a fluid filled foam can then be found by adding the two stress contributions as

$$\sigma_{tot} = E_s C_4 \left(\frac{\rho^*}{\rho_S}\right)^2 \left(1 + \left(\frac{\rho^*}{\rho_S}\right)^{1/2}\right)^2 + \frac{C\mu\dot{\varepsilon}}{1-\varepsilon}\left(\frac{L}{l}\right)^2 \tag{2.26}$$

This scaling and modeling presented here only considers the effect of the presence of a Newtonian fluid; the analysis becomes more complex if the fluid is non-Newtonian. Some previous work has been carried on the effect of non-Newtonian fluid flowing through incompressible porous material and has been summarized by Pearson [37] in a review article. These models are very complex and necessitate numerical simulation to account for the material microstructure and the non-Newtonian properties of the fluid.

The combination of compressibility and non-Newtonian fluid rheology has not been considered to date.

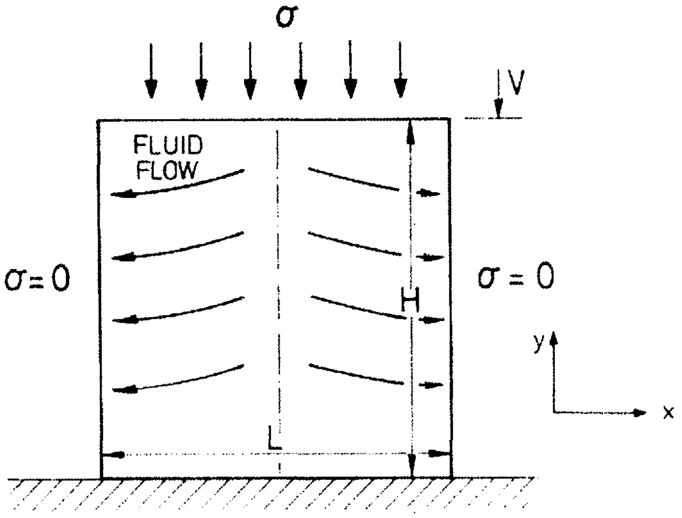

Figure 2.2.6: The compression of a fluid-filled, open-cell foam. The pressure gradient, of order σ/L, expels the fluid through the two vertical faces [35].

2.2.2.3. Poroelastic Model

A different way of looking at the problem of fluid flow through a deforming solid matrix comes from the application of poroelastic models. Poroelastic models were first introduced by Biot [38] and are now commonly used to study wave propagation in fluid saturated soils [39-41] as well as, more recently, in studying the mechanical response of biological tissue [42-44]. These three dimensional models often require complex computer simulations that account for pore microstructure as well as solid deformations, and in the case of biological tissue, the matrix surface charges. For our case a simple one-dimensional model can be derived by accounting for the force and momentum in a solid matrix filled with a viscous fluid as shown in Figure 2.2.7. In this model the sides of the matrix are constrained by frictionless walls to allow for a purely one dimensional model.

By assuming that the solid matrix behaves as a Hookean solid we can first write the constitutive relation for the matrix:

$$\sigma_{11} = H\varepsilon_{11} - p \qquad (2.27)$$

where σ_{11} is the stress in the vertical direction, H is the bulk modulus in compression, ε_{11} is the vertical strain, and p is pressure. Additionally we can apply Darcy's law, which in 1D is written as

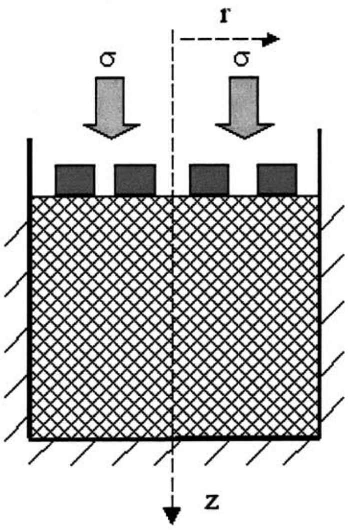

Figure 2.2.7: Geometry for a simple 1D poroelastic model. The sides of the cylinder are constrained by frictionless walls as it is the bottom, the top surface is porous to allow for water flow.

$$v_f = -\frac{K}{\mu}\frac{\partial p}{\partial x} \qquad (2.28)$$

where v_f is the fluid velocity, K represents the permeability of the solid matrix, μ is the fluid viscosity and $\frac{\partial p}{\partial x}$ the pressure gradient. Mass conservation is written as:

$$v_f = -\frac{\partial u}{\partial x} \qquad (2.29)$$

where u is the solid matrix displacement. The negative sign in the expression accounts for the fluid flowing always in the opposite direction (due to the fluid incompressibility) than the solid matrix displacement. Finally the momentum balance is written as:

$$\frac{\partial \sigma}{\partial x} = \rho \frac{\partial^2 u}{\partial x^2} \tag{2.30}$$

where ρ is the density of the solid matrix. These equations can be combined to obtain the well-known Telegraph equation.

$$\rho \frac{\partial^2 u}{\partial t^2} + \frac{\mu}{K} \frac{\partial u}{\partial t} = H \frac{\partial^2 u}{\partial x^2} \tag{2.31}$$

2.2.2.4. Energy Absorption of Foams

The popularity of elastomeric reticulated foams comes from their ability to absorb energy at a relatively constant stress. Their mechanical response to impact, combined with the lightweight properties, makes them perfect for this type of application. Figure 2.2.8 illustrates a typical stress-strain curve of an elastomeric foam; the energy absorption or the work done (per unit volume) by the foam is represented by the area under this curve. Most of the energy is absorbed along the flat plateau, and therefore at constant load and can be calculated as

$$W = \int_0^{\varepsilon} \sigma d\varepsilon \tag{2.32}$$

and because the stress is almost constant throughout the compression we can estimate it to be

$$W = \sigma^* \varepsilon_f \tag{2.33}$$

If the foam is also filled with a Newtonian fluid then the total work needs to also account for the squeezing of fluid phase and can be estimated with the following expression:

$$W_{fluid} = \int_0^{\varepsilon_f} \sigma_f^* d\varepsilon = C\mu\dot{\varepsilon}\left(\frac{L}{l}\right)^2 \left(\frac{1}{1.4\rho^*/\rho_S}\right) \tag{2.34}$$

where σ_f^* is described by equation (2.25) and the final strain ε_f is set equal to the densification strain as described in equation (2.21).

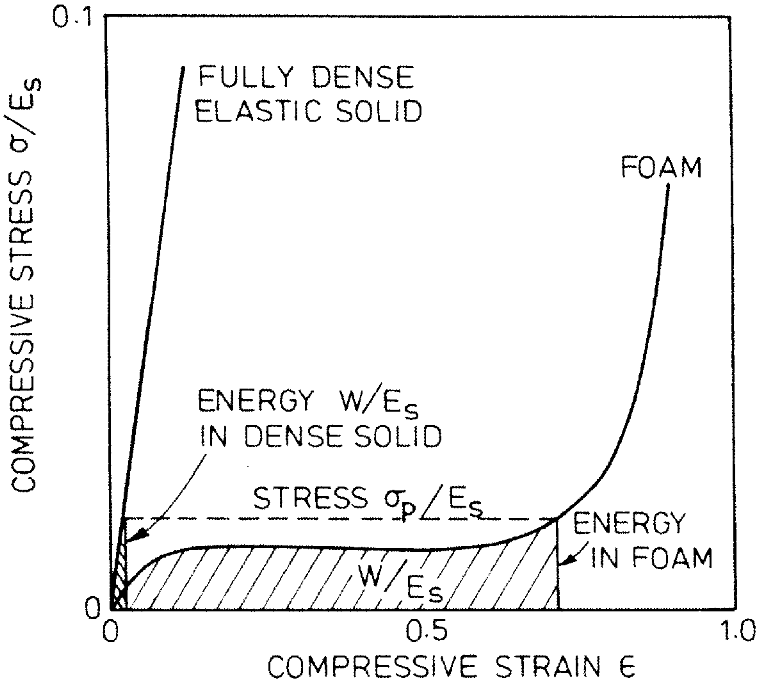

Figure 2.2.8: Stress-strain curves for an elastic solid and a foam made from the same solid, showing the energy per unit volume absorbed at a pear stress σ_p [35]

2.2.2.5. Optimization Criteria

Choosing a particular foam for an application requires not only knowledge of the foam material properties but also the amount of energy that needs to be absorbed, the rate of impact and the maximum allowable stress. Peak stress is in fact the parameter that is of most concern, for example: even if a particular foam has the capacity of absorbing a great amount of energy during impact, if its plateau stress is greater than the one allowable by the system, the stress will grow and exceed the system maximum stress before the foam has a chance to reach the plateau and absorb the impact energy. For example, in the hip padding system described in section 2.1.5.1 the load for STF protected hip reaches a peak of around 4400N. If the femur can only sustains loads below that limit, the femur will break before the foam reaches its peak and it has a chance of absorbing the impact energy.

For these reasons it is useful to construct an optimization curve. This is commonly done by integration of the stress-strain curve to find the work done by the foam and replotting the data as normalized work vs. normalized stress for different strain rates (Figure 2.2.9(b)). The optimum energy absorbed is in the region of the curve inflection, which corresponds to the beginning of the densification region. An optimization line is drawn to connect the inflection points of different strain rate characterizations (broken line in Figure 2.2.9(b)). A number of these lines can be also derived for different density foams and a complete energy absorption diagram can be constructed as in Figure 2.2.9(c).

When foams are filled with a fluid, optimization becomes more complex. As seen earlier the fluid contribution to stress depends on both strain and strain rate and, especially if the fluid viscosity is relatively high, there is no clear transition between the plateau and densification region. Nevertheless we can still represent the stress-strain response in a similar fashion. For this case there is no clear optimization line but what we find is an area of optimization.

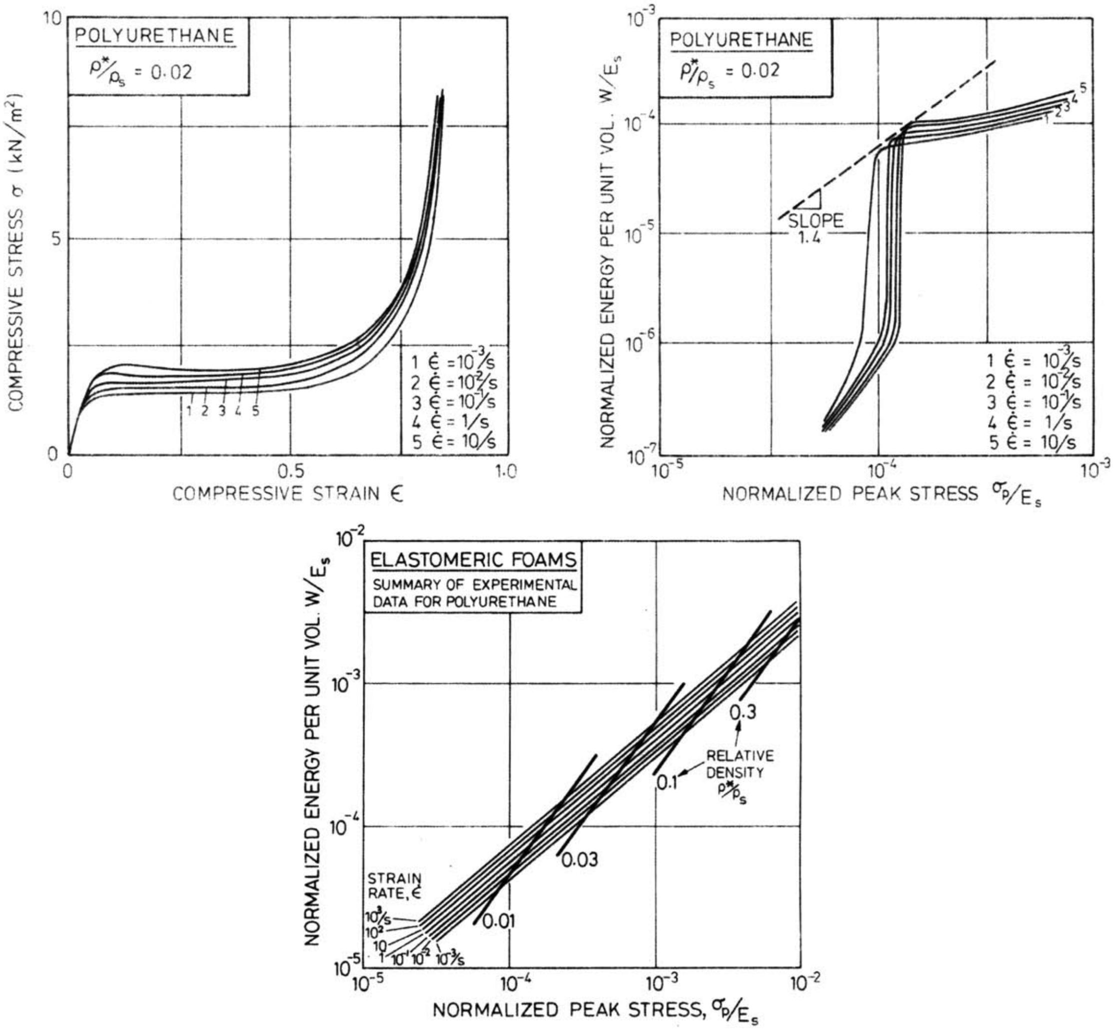

Figure 2.2.9: (a) Stress-strain curves for elastomeric foam with $\rho^*/\rho_s = 0.02$, at five strain rates. (b) Energy absorption curves constructed from stress-strain curves. The envelop (broken line) gives a contour of constant relative density: it's slope about 1.4. (c) an energy-absorption diagram for an elastomeric foam. Although it was constructed using data from polyurethane, it is broadly typical of all elastomeric foams [35].

There are a number of other ways to characterize energy absorption. Some of the most popular methods are to use Cushion or Jensein factors; more details can be found in Gibson and Ashby [35].

2.2.3. Testing Apparatus for Material Properties of Foams

As explained earlier in section 2.2.2.2 by equation (2.25) the material properties of reticulated foams and especially fluid-filled foams, are functions of strain rates. To be able to characterize these over a wide range of strains rates (many orders of magnitude) a number of different apparatus and techniques are necessary. Table 3.1 illustrates some of the most common testing apparatuses and the typical strain rates ranges that they are able to achieve. In the present work three different instruments were used: the Texture Analyzer, drop tower impact tester, and split Hopkinson pressure bars.

Texture Analyzer	Servohydraulic frames	Drop Test	Hopkinson Pressure Bar	Taylor Impact Bar
$\dot{\varepsilon}=10^{-4}-10^{0}s^{-1}$	$\dot{\varepsilon}=10^{-1}-10^{1}s^{-1}$	$\dot{\varepsilon}=10^{0}-10^{3}s^{-1}$	$\dot{\varepsilon}=10^{2}-10^{4}s^{-1}$	$\dot{\varepsilon}=10^{4}-10^{5}s^{-1}$

Table 3.1. Strain rates ranges achievable by different testing techniques and apparatuses.

2.2.3.1. Texture Analyzer

The Texture Analyzer (TA.XT Plus) by Stable MicroSystem (SMS) is a mechanical tester widely used for 'low strain rate', typically in the range of 10^{-6}-10^{0} 1/s, characterization of solids or semi-solid materials. The apparatus comes with interchangeable fixtures (see Figure 2.2.10) for a variety of applications, as for example, food industry, pharmaceutics, electronics, adhesive etc. The apparatus employs a load cell that can measure forces up to 50 kg with resolution of 0.1 g. The moving top plate can achieve velocities from 0.01-40 mm/s, with linear or exponential velocity profiles, and the vertical displacement is measured with a resolution of 10^{-3} mm.

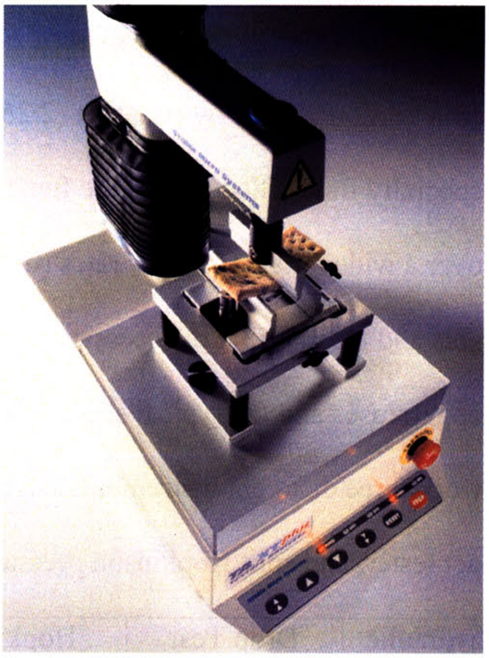

Figure 2.2.10: The Texture Analyzer, a low strain rates mechanical tester with interchangeable fixtures. http://www.stablemicrosystems.com

2.2.3.2. Dynatup Drop Tower

Drop Tower Impact tests were carried out using a Dynatup 9850 from Instron (see Figure 2.2.11). Drop Towers are commonly used to determine impact resistance of plastic, metal composites, rubber, etc. This specific model includes a spring assisted velocity accelerator that can achieve impact velocity of 20 m/s and impact energies of 1600J. The load cell is able to record forces up to 45 kN, at a speed of 5MHz. The tup, used to penetrate the sample, and bottom fixture can be modified to either produce a 'penetration impact,' as for example to test sheets of composites or a simple compression, with a wide and flat tup see Figure 2.2.12.

Figure 2.2.11: Dynatup. Drop tower apparatus for low to medium impact energies. www.instron.com

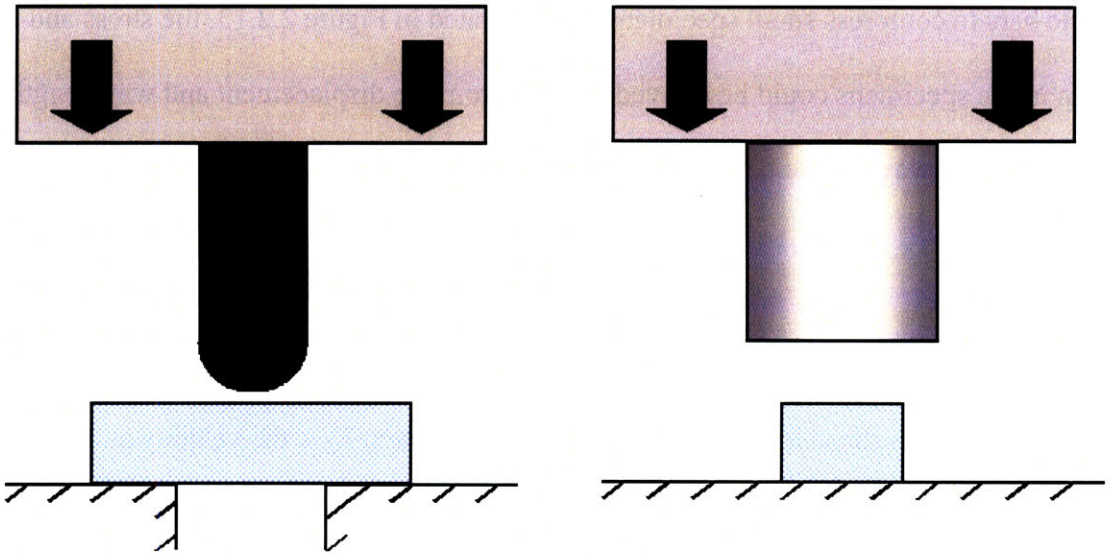

Figure 2.2.12 (left) original set up of Dynatup for sample penetration. (right) modified Dynatup set up for unconstrained compression experiments.

2.2.3.3. Split Hopkinson Pressure Bars

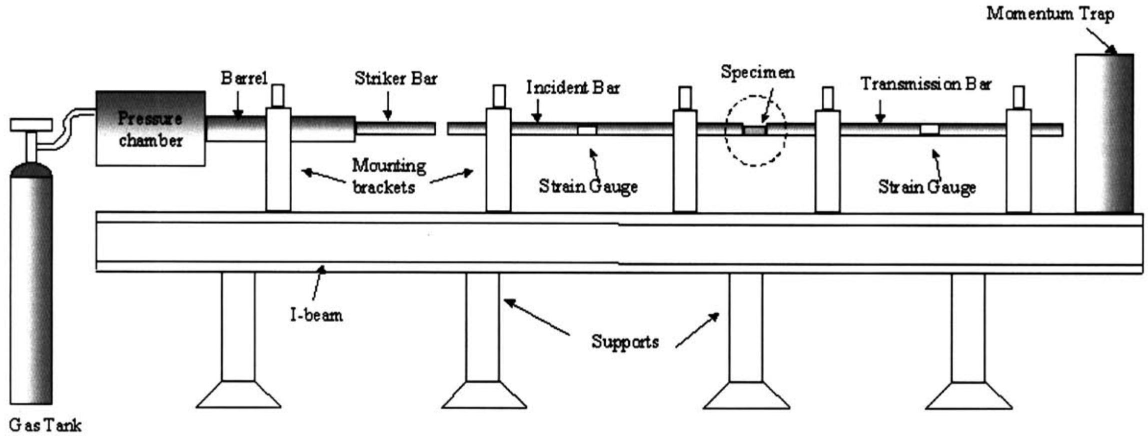

Figure 2.2.13: Schematic of split Hopkinson pressure bars. The striker bar is propelled into the incident bar where the specimen, sandwiched between the incident and transmission bars, is compressed. The compression waves in the bars are measured by strain gauges as a function of time.

The split Hopkinson pressure bars apparatus is commonly used for material characterization in uniaxial compression at very high strain rates (10^2-10^4 s^{-1}). This method was first developed by Hopkinson in 1914 who calculated that by using long elastic bars to compress small specimens, as illustrated in Figure 2.2.13, the stress and strain in the specimens could be derived directly from the displacement and wavelength of the pressure wave in the bars. More specifically the strain rate of the specimen is defined as:

$$\frac{d\varepsilon}{dt} = \frac{V_1 - V_2}{L} \tag{2.35}$$

where V_1 is the velocity at the incident bar interface, V_2 is the velocity at the transmission bar interface and L is the length of the specimen. V_1 and V_2 can be defined as a function of the bars properties and strains as follows:

$$V_1 = C_0\left(\varepsilon_I - \varepsilon_T\right) \tag{2.36}$$

$$V_2 = C_0\varepsilon_T \tag{2.37}$$

where C_0 is the wave speed inside the bars and is defined as $\sqrt{\frac{E}{\rho}}$ and ε_I, ε_R, ε_T are the incident, reflected and transmitted strain respectively. By substituting 3.20 and 3.21 into 3.19 we obtain the following expression:

$$\frac{d\varepsilon(t)}{dt} = \frac{C_0}{L}\left[\varepsilon_I(t) - \varepsilon_R(t) - \varepsilon_T(t)\right] \tag{2.38}$$

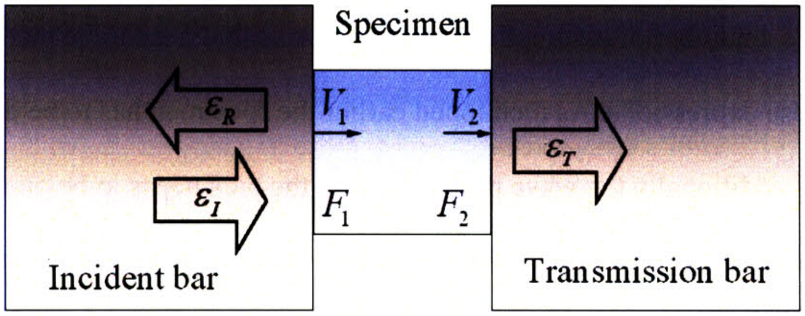

Figure 2.2.14: Schematic of specimen sandwiched between two pressure bars.

Similarly we can define the stress at the specimen/bars interface as:

$$\sigma(t) = \frac{F_1 + F_2}{2A} \tag{2.39}$$

where F_1 and F_2 can be written as $F_1 = E\left[\varepsilon_1(t) + \varepsilon_R(t)\right]A_0$ and $F_2 = EA_0\varepsilon_T(t)$, E is the bar modulus, A is the diameter of the bar and A_0 is the specimen diameter. Combining these equations we derive at the following expression:

$$\sigma(t) = \frac{E}{2}\frac{A_0}{A}\left[\varepsilon_I(t) + \varepsilon_R(t) + \varepsilon_T(t)\right] \tag{2.40}$$

After impact, stress waves propagate through the sample and only after some time, the time for the sample to reach equilibrium, the sample will be deforming uniformly. If deforming uniformly the following relation holds:

$$\varepsilon_I(t) + \varepsilon_R(t) = \varepsilon_T(t) \tag{2.41}$$

When this relation is substituted in equation 3.22 and 3.24 we obtain:

$$\frac{d\varepsilon(t)}{dt} = \frac{-2C_0}{L}\varepsilon_R(t) \tag{2.42}$$

$$\sigma(t) = E\frac{A_0}{A}\varepsilon_T(t) \tag{2.43}$$

These two expressions are the fundamental basis used for the calculation of stress and strain rates in the specimen. Strains are obtained by integration of equation (2.42) in time. There are a number of assumptions and conditions that need to be met in order to be able to use these expressions. As mentioned earlier the specimen has to be deforming uniformly and additionally the wave propagation in the bars needs to be one-dimensional. The latter condition can usually be achieved by using very long bars, at least 10 times their diameter, and a ratio of radius to wavelength $R/\lambda \ll 1$.

This method was originally used for the high rates characterization of metals and ceramics but recently scientists have tried to modify this technique to measure the characteristic of much softer material like foams [45-47] and biological tissue. The major problem with the characterization of these softer materials is that their impedance is much smaller than the impedance of steel or aluminum. This impedance mismatch doesn't allow the incident wave to be transmitted to the sample (most of the wave is reflected back) and it results in a transmission signal that is too small to measure. For this reason hollow aluminum bars [48] with higher sensitivity strain gauges [49] or polymeric bars [50, 51] have recently been use.

2.3. Blast Waves

2.3.1. Introduction to Blast Waves

Blast waves are created by expanding high-pressure gases which compress the surrounding air creating a pressure pulse that travels in all directions [52]. As the air is compressed the temperature rises which affects the speed of propagation of the wave. This effect creates a steepening of the pressure wave which culminates into the creation of a shock front. Figure 2.3.1 illustrates the formation of the shock wave as function of the distance traveled. The transmission and reflection of blast waves has been studied extensively; in particular, the military has shown great interest in the behavior of blast waves that encounter obstacles, as in battlefields, or that are reflected back and forth in an enclosed space [53], as for example, inside a tanker. There are two main types of waves: free-field and complex. Free-field waves or simple waves are characterized by a very steep increase in pressure until a peak value is reached. The peak is followed by an exponential decay which sometimes reaches pressures below atmospheric (underpressure) before returning to normal, see Figure 2.3.2b. One of the most important characteristics of a simple blast wave is the rate of pressure rise, which has been linked to lung blast injuries [54], but also important are the peak pressure, pulse duration, impulse and magnitude of the underpressure.

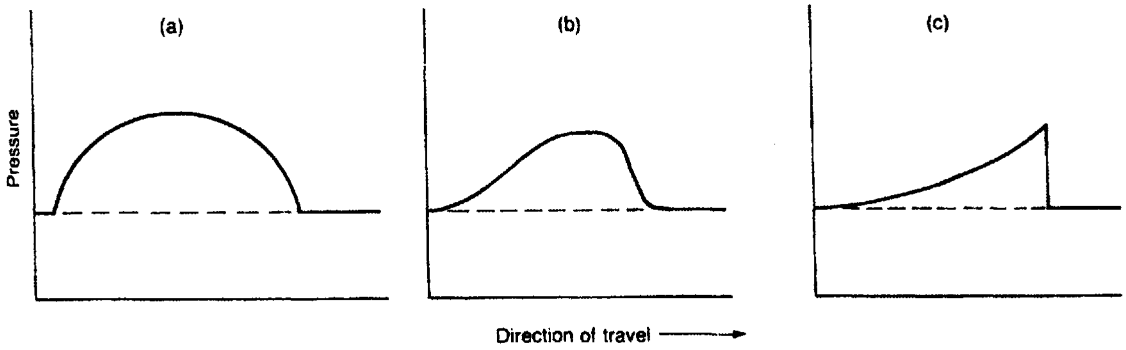

Figure 2.3.1: Steepening of pressure pulse to form a shock-wave. Illustrative pressure vs. distance relationships at successive times (a), (b) and (c) [55].

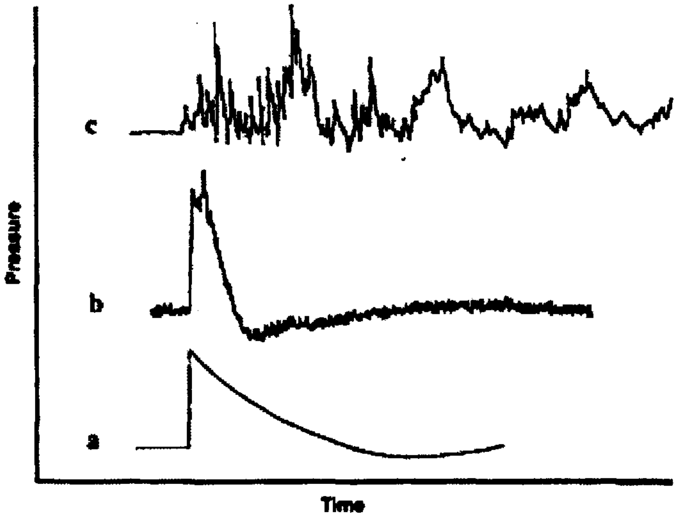

Figure 2.3.2: Three pressure time histories: (a) idealized wave or classic Friedlander, (b) Simple free-field wave, (c) Complex wave [56].

Complex waves are best described as a series of non-uniform shocks, as illustrated in Figure 2.3.2c, and are usually created when simple waves interact with obstacles, walls or enter an enclosure [57].

As blast waves propagates away from the epicenter their peak pressure attenuates rapidly [55]. Near the source the peak overpressure decreases with the cube of the distance from the explosion, but, at greater distances, it decreases more slowly until the peak overpressure decreases almost linearly with distance. A sketch of blast waves profile illustrating the relationship between overpressure and range is shown in Figure 2.3.3. According to the Rankine-Hugoniot equations for an ideal blast-wave, the shock front velocity can be express as:

$$V = c_o \left(1 + \frac{\gamma + 1}{2\gamma} \frac{p_s}{p_o} \right)^{1/2} \tag{2.44}$$

where c_o is the ambient speed of sound, p_s is the peak static overpressure p_o the ambient pressure and γ is the heat capacity ratio [55]. Similarly, the air density behind the blast front is related to the undisturbed air density ρ_o as follow:

$$\rho = \rho_o \left(\frac{2\gamma p_o + (\gamma + 1) p_s}{\gamma p_o + (\gamma - 1) p_s} \right). \tag{2.45}$$

If the explosion occurs above ground the reflection of the blast wave will interact with the initial incident wave to form what is called a Mach Stem, see Figure 2.3.4. On ground level, the Mach Stem is nearly vertical, the overpressure acts horizontally and have a greater magnitudes than the original blast waves; a more detailed discussion regarding Mach Stems is given by Iremonger [55].

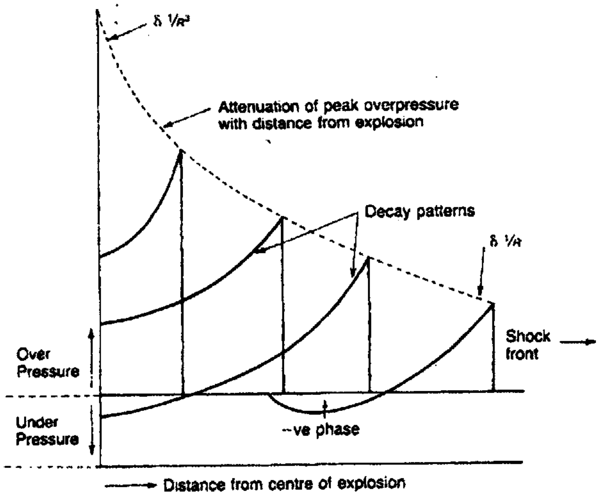

Figure 2.3.3. Blast-waves profiles at increasing distances form center of explosion showing attenuation with range [55].

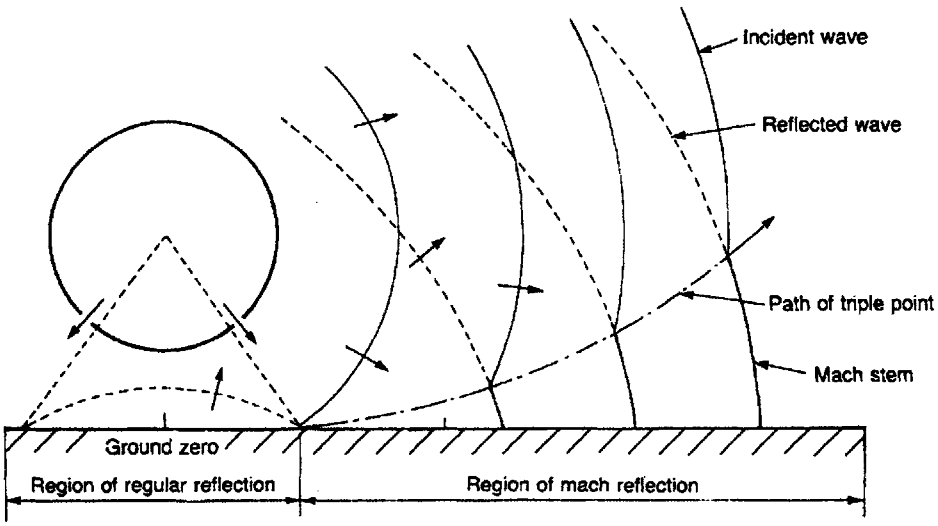

Figure 2.3.4. Mach Stem creation from an above-ground explosion [55].

2.3.2. Lung Blast Injuries

The interaction of blast waves and their effect on the human body has been studied since the 1950s; decades of animal studies and tests on human volunteers have resulted in the development of an extended body of literature and various injury criteria. Blast injuries can be divided into three main categories: primary, secondary and tertiary. Primary blast injuries (PBI) are caused directly by the blast wave and its interaction with the victims' organs. These injuries are generally confined to a small area surrounding the blast epicenter [53], as the magnitude of the blast waves decays quickly. Secondary blast injuries are caused by flying fragments which cause both blunt and penetrating injuries. These are the predominant form of injuries as flying debris or shrapnel can travel long distances and therefore have a greater 'injury area' well beyond that of PBI. Table 2.3.1 shows the type of blast injuries that are commonly seen as a function of distance from the blast. Tertiary injuries are caused by the displacement of the body due to the pressure wave or blast winds. Other additional types of injuries that can occur due to blast are burn and inhalation of toxic fumes [53].

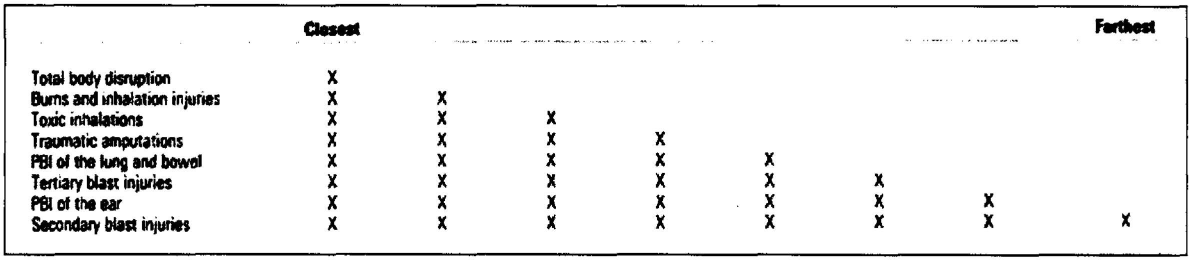

	Closest							Farthest
Total body disruption	X							
Burns and inhalation injuries	X	X						
Toxic inhalations	X	X	X					
Traumatic amputations	X	X	X	X				
PBI of the lung and bowel	X	X	X	X	X			
Tertiary blast injuries	X	X	X	X	X	X		
PBI of the ear	X	X	X	X	X	X	X	
Secondary blast injuries	X	X	X	X	X	X	X	X

Table 2.3.1: Expected injuries to unprotected victims at relative distances from a high-explosive detonation in open air [52].

Primary blast injuries can occur in many of the major organs: brain, ears, heart, etc. [56], but are most common in air filled organs. In organs containing gas PBI occur when, due to a rapid acceleration of the body, a stress-wave propagates into the underlying tissue causing, in the case of the lungs, pulmonary contusion [52]. Stuhmiller [58] has shown that all major air-containing organs have similar injury threshold, even though, under multiple exposure the GI track was found more susceptible to injuries. The injuries usually occur at the site of the approaching blast wave but can be diffuse when the victim is located in a confined space [56]. Victims from blast in enclosed spaced are also at greater risk of PBI because solid surfaces can reflect blast waves and magnifies the overpressure by 2 to 20 times [55].

As mentioned earlier, Primary Blast Injuries do not only occur in air-filled organs but can cause damage to the brain, heart or limbs. Hull and Cooper [59] have shown though modeling that limb amputation injures and fractures in explosions were in fact primary blast injuries caused by the coupling of the shock wave with the tissue. Cernak et al. [60] have studied more than 1300 patients injured by explosive munitions admitted to the Military Medical Academy in Belgrade. Their study showed that PBI caused long-term neurological problems and could also be linked to some aspects of Post Traumatic Stress Disorder. Heart problems have also been reported after exposure to blast overpressure as cardiac arrhymia, cardiac contusions and coronary artery obstruction from air emboli [56].

2.3.3. Lung Blast injury Mechanism

Some debate still exists as to the principal injury mechanism for lung blast injuries is: the gross compression of the chest wall or the coupling of the stress waves with the chest cavity. It is believed that, for short duration waves (about 1ms), the coupling of stress waves into the thorax is the main injury mechanism, while, for long duration blast (above 100 ms)it is the gross compression of the chest [54]. According to Cooper [54] the coupling mechanisms can be summarized as:

1) Rapid acceleration of the chest creates a coupling between the stress wave and the thorax.
2) A pressure wave, whose magnitude is proportional to the velocity of the chest wall, is propagated into the lungs.
3) The wave creates pressure differential across alveoli that induce rupture. The magnitude of the pressure differential is proportional to the rate of pressure rise of the wave.
4) The stress wave will reflect and reinforce within the chest and create concentration points of injuries.

The stress concentration points are additionally aggravated by the fact, as suggested by Fung [61] and subsequently supported by numerical simulation [62], that the curvature of the thoracic wall contributes to the focusing of the energy in the lung.

Cooper [63] has shown, as illustrated in Figure 2.3.5, a correlation between the peak acceleration of the wall with the severity of the lung injury, for anesthetized pigs the injury threshold was determined to be about 10^4 m/s^2.

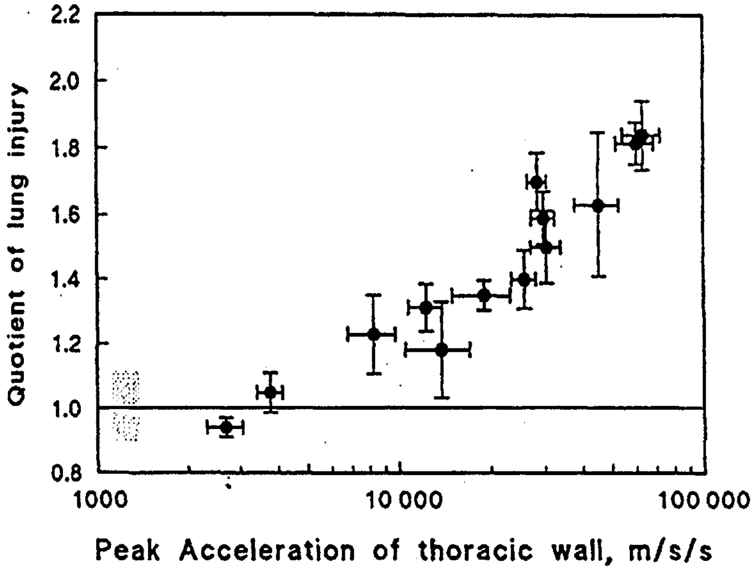

Figure 2.3.5: Correlation between the peak acceleration of the thoracic wall and severity of lung injury for short-duration waves [63].

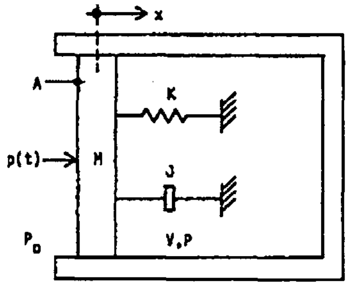

A = effective area
M = effective mass
V = gaseous volume of the lungs at zero displacement
x = displacement
J = damping factor
K = spring constant
P_0 = ambient pressure
p(t) = external overpressure blast load
P = $P_0[V/(V - A \cdot x)]^g$ = intrathoracic (or lung) pressure
g = polytropic exponent for gas in lungs

Parameter	Units	70-kg Body	Scaling Factor
M	kg	2.03	$(m/70)$
J	Ns/m	696	$(m/70)^{2/3}$
K	N/m	989	$(m/70)^{1/3}$
A	m^2	0.082	$(m/70)^{2/3}$
V	m^3	1.82×10^{-3}	$(m/70)$
g	—	1.2	—

Figure 2.3.6: (Top) Mathematical model of the thorax. (below) Model parameters for a 70 kg mammal [64].

In order to understand the injury mechanism some attempts have been made to model the chest wall cavity with a spring-mass-damper system [64]. A sketch of the system used by Alexlsson & Yelverton with the numerical values of the parameters for the modeling is given in Figure 2.3.6. The system is governed by the following equation:

$$M\frac{d^2x}{dt^2}+J\frac{dx}{dt}+Kx=A\left[p(t)+P_o-\left(\frac{V}{V-Ax}\right)^g P_o\right] \tag{2.46}$$

By using this model combined with their results from animal blast testing they were able to correlate the peak inward chest wall velocity to the level of injury caused by both ideal and complex blast waves. An empirical relation between the wall velocity and the injury level, Adjusted Severity of Injury Index (ASII), was described as followed:

$$ASII=(0.124+0.117V)^{2.63} \tag{2.47}$$

where V is the chest wall velocity. The relation between ASII and the level of injury is given in Table 2.3.2. Alexlsson & Yelverton [64] also conducted a number of animal studies (using anesthetized sheep) in a rectangular blast chamber. Higher chest wall velocities and therefore greater level of injuries were recorded at the corner of the blast chamber even though this position was farther away from the charge than, for example, along the walls of the chamber.

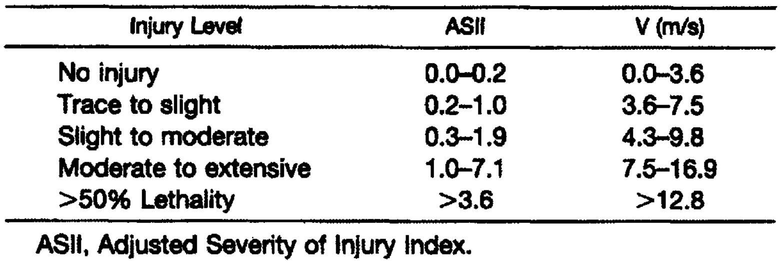

Injury Level	ASII	V (m/s)
No injury	0.0–0.2	0.0–3.6
Trace to slight	0.2–1.0	3.6–7.5
Slight to moderate	0.3–1.9	4.3–9.8
Moderate to extensive	1.0–7.1	7.5–16.9
>50% Lethality	>3.6	>12.8

ASII, Adjusted Severity of Injury Index.

Table 2.3.2: Injury levels with corresponding ASII and maximum inward chest wall velocity [64]

Similarly Stuhmiller [65] described the chest wall using a single degree of freedom model and used it to calculate the amount of irreversible work done by the loading of a blast wave. In this model he treated the lung as a closed chamber with a piston on one of its side, see Figure 2.3.7, which is described by the following equation:

$$m\frac{dv}{dt} = P_{load}\left(t\right) - \rho c_o v - p_o\frac{x}{L} \tag{2.48}$$

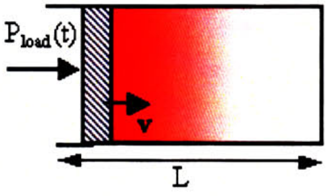

Figure 2.3.7: Pleural dynamic model. Sketch of the model used to represent the lung.

where m is the mass divided by the chest wall area, v is the velocity, x is the displacement, L is the ratio of lung volume to chest wall area, c_0 and p_0 are the speed of sound and pressure in the undisturbed lung respectively and P_{load} is the external pressure loading. The displacement information from Eqn. (2.48) can then be used to calculate the normalized work W* done by the system as:

$$W^* = \frac{W}{p_o V} = \frac{1}{p_o L}\int_0^\infty \rho_o c_o v^2 dt \tag{2.49}$$

The model was then used to calculate the normalized work for a large number if animal experiments that had been conducted and published since the 1970's; this was found to correlate very well, as shown in Figure 2.3.8. The solid lines in the graph correspond to the level of injury varying form trace to severe.

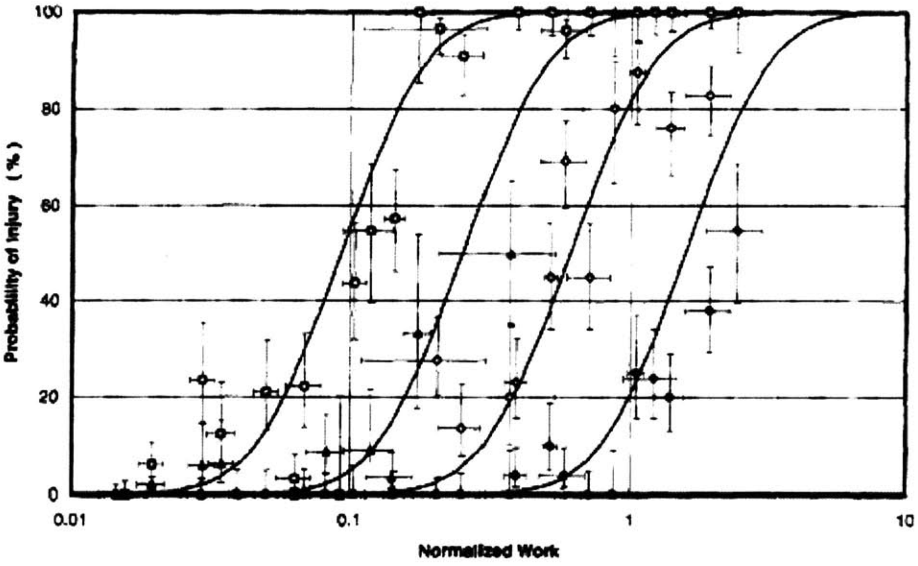

Figure 2.3.8: Correlation of incidence of injury with normalized work. (empty triangle) trace or greater, (full triangle) slight or greater, (empty circle) moderate or greater, (full circle) severe [65].

2.3.4. Blast protection

There has been a lot of interest from the scientific community and especially from the military on a better understanding of blast injuries and protection. The military interest in the topic is obvious, but also recently some of their new shoulder fired weapons were reported to create blasts that exceed current exposure standards [58]. This is obviously undesirable since it restricts the amount of weapon-training that soldiers are allowed to follow before going into combat [65]. In fact current textile armor and rigid body armor are very effective against fragment injuries but offer no protection against Primary Blast Injuries [54, 63].

The purpose of personal blast protection against PBI is to reduce the peak acceleration of the body wall [54]. Certain considerations must be taken into account when designing a blast protection garment. Total coverage of the thorax is essential [54, 63], as stress waves can enter the chest wall through the underarm and the back of the body. Laminating of layers has to be done with extreme caution as this can create resonant frequencies that can be excited and interfere with the mitigation mechanism [63]. Lastly, flexibility and weight limits must be considered to create protection garments that are practical in both a battlefield and civilian environment.

Various animal studies have been conducted to aid the design of blast protection gears and to better understand the mechanism of blast injuries. Experiments on anesthetized rats exposed to short-duration waves showed that neither rubber nor viscoelastic foams reduced the incidence of lung damage; on the contrary studies found that such materials significantly augment the injuries [66]. The use of a hard plate also did not reduce the magnitude of the injuries but when placed in front of the foam the composite system was able to substantially reduce the level of injuries; the results are shown in Figure 2.3.9. Similar results were found for resin-bonded Kevlar on top of foam in experiments with both rats and larger animals, such as pigs (Figure 2.3.10)[63]. This demonstrated that for short duration waves the coupling of the wave with the thorax is the predominant mechanism of injury and the concept of impedance mismatch can be used to effectively reduce injuries to the lungs. For more details on the concept of impedance mismatch see Cooper's work [54] on stress wave decouplers.

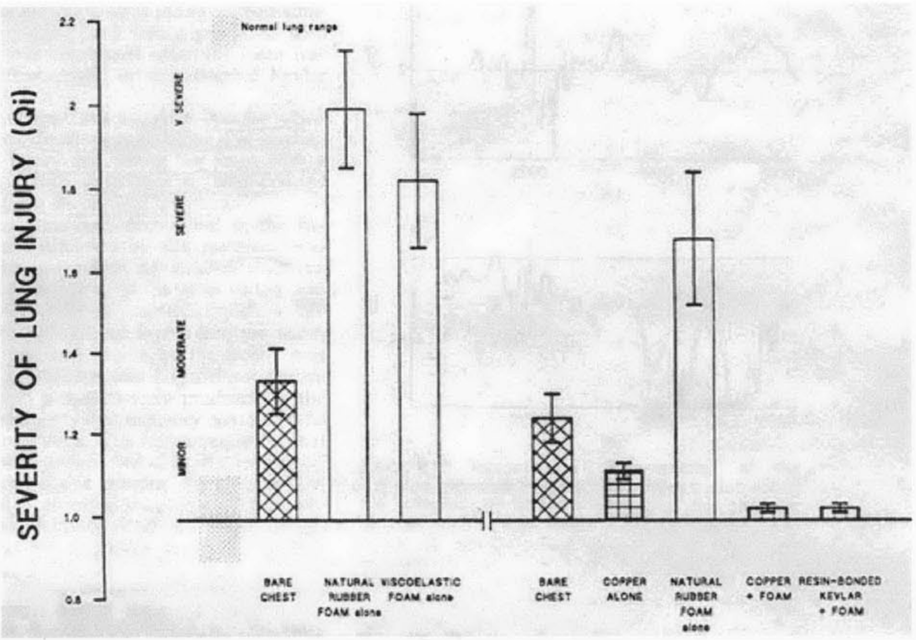

Figure 2.3.9: Severity of lung injuries in rats exposed to short-duration waves (1.7 ms) with various covering materials. Qi is the severity of lung injury and it is calculated as the ratio of the lung weight (injured and filled by blood) to the predicted normal weight [63].

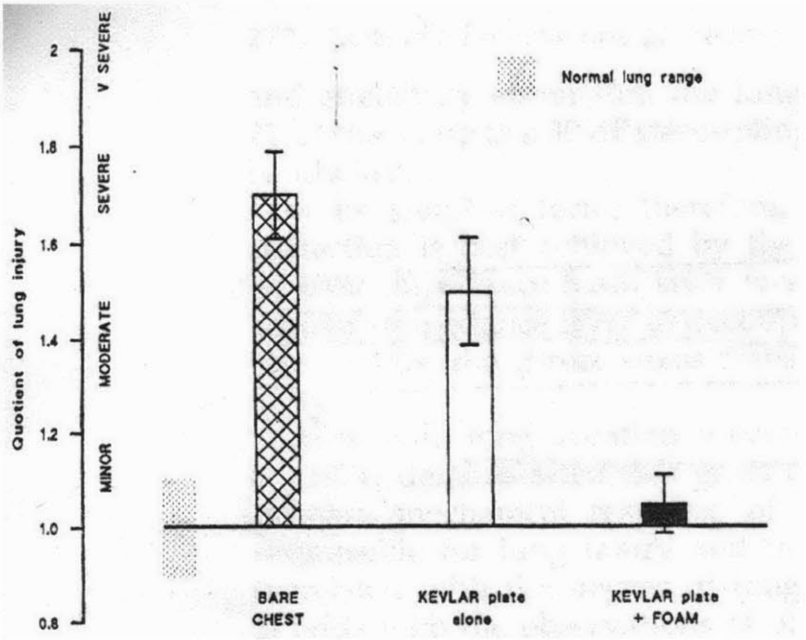

Figure 2.3.10: Protection from short-duration blasts by resin-bonded Kevlar on anesthetized pigs. Qi is the severity of lung injury and it is calculated as the ratio of the lung weight (injured and filled by blood) to the predicted normal weight [63].

2.3.5. Polymeric Foams under Blast Loading

The use of polymeric foam for blast wave attenuation has been studied extensively since the 1970s. One of the commonly found properties is that under certain conditions foams will actually amplify the magnitude of the peak pressure and therefore should not be used alone, as a single layer, for blast protection. A detailed study on the material response of closed-cell foams [67] subjected to blast waves with Mach numbers between 1.2-2.7 has revealed that for a single layer of foam the blast pressure is dramatically reduced, 60 -70 % when the deformation of the foam is within its stress plateau region, see section 2.2.2.1 for description. On the other hand, if the thickness is not large enough to attenuate the wave, the foam will collapse (enter densification region) which will result in the amplification of the peak pressure. The thickness of the sample also affects the duration of the transmitted wave, as thicker samples increase the duration of the pulse; this is illustrated in Figure 2.3.11.

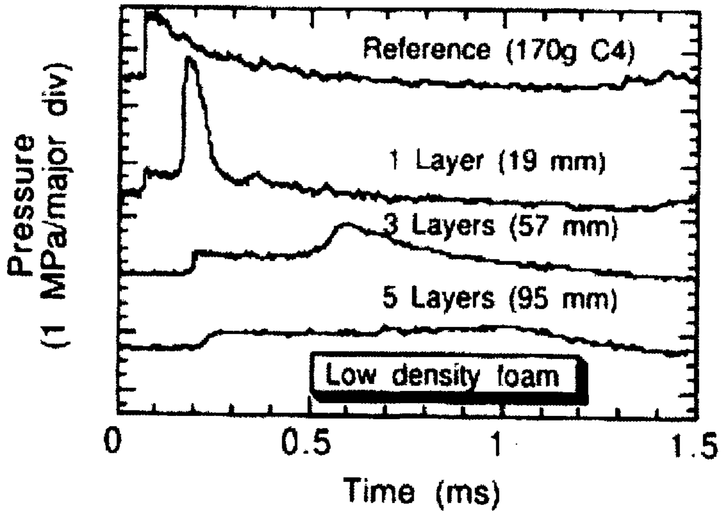

Figure 2.3.11: Effect of foam layer thickness on the reflected pressure recorded behind low-density polyethylene foam for 170 g C4 charge [67].

Ouellet et al. [68] has found similar results for a number of different types of foam and have also shown that weak waves, which do not deform the foam beyond its linear region (see section 2.2.2.1) also get amplified.

2.3.6. Shock Tube Apparatus

Shock tubes have been widely used to study nonstationary problems in fluid mechanic such as transition through shock fronts, waves interactions, subsonic, transonic and supersonic flows, shock loading of structures etc...[69]. A shock tube usually consists of a long tube closed at both ends that is separated into two chambers by a diaphragm. The diaphragm can be made from cellophane, paper or metallic foils. One of the chambers, the small one, is pressurized until the diaphragm bursts. This creates a shock wave that travels along the tube and a rarefaction wave that travels in the opposite direction. This is shown schematically in Figure 2.3.12. The air in the long chamber is compressed adiabatically by the wave and is assumed to have constant pressure, density, temperature, entropy and wave velocity. The rarefaction wave, on the other hand is assumed to expand the air isentropically. With these assumptions the relationships between pressures across the diaphragm and across the shock waves can be derived [70]. The results of the complete analysis of the flow in a shock tube are summarized in Table 2.3.3.

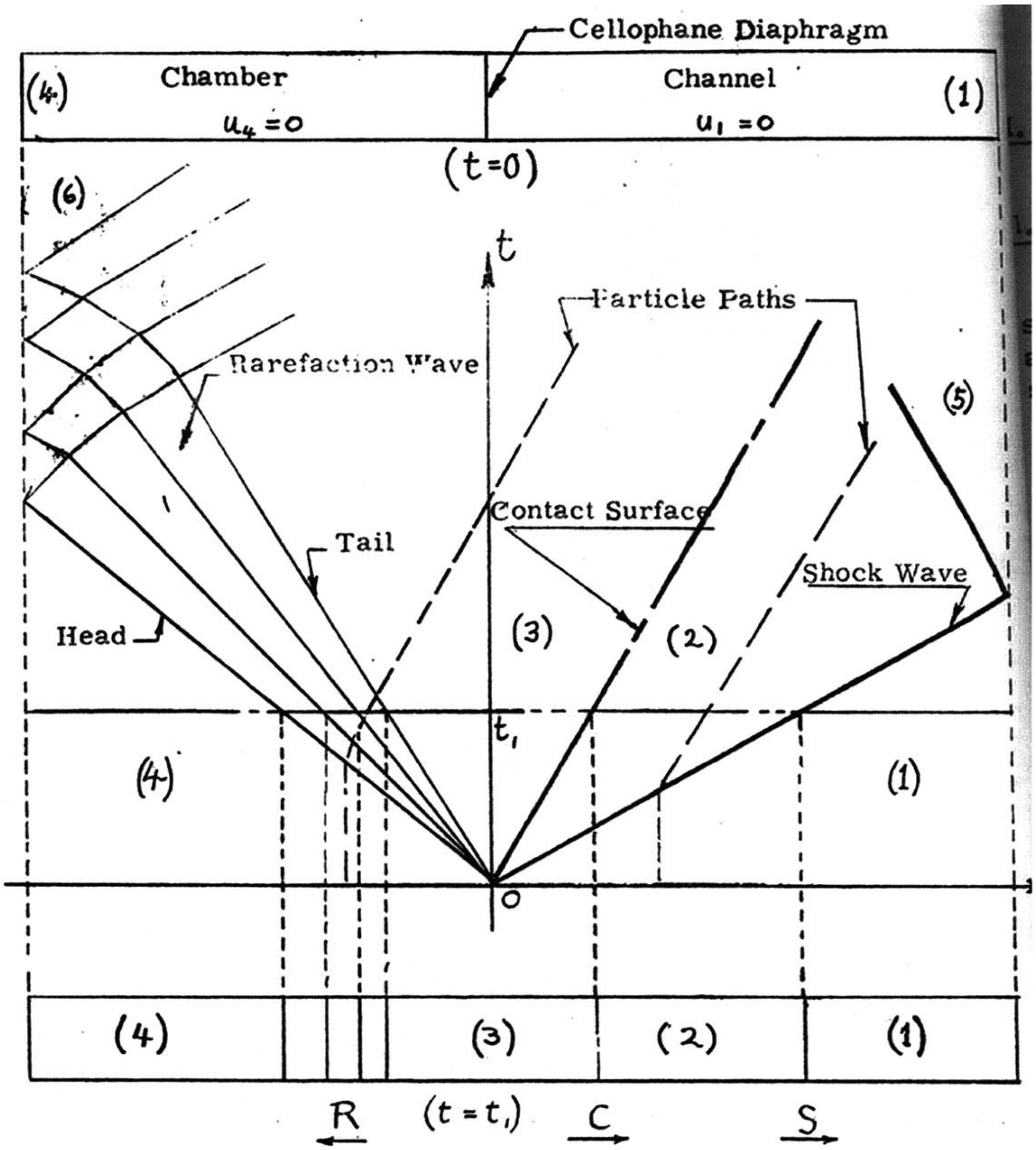

Figure 2.3.12: Theoretical diagram of the (x,t) plane showing the waves and the states in the shock tube from the instant the diaphragm ruptures [70].

Pressure Relations	$(P_{21}-1)\sqrt{\frac{\beta_4 E_{14}}{\alpha_1 P_{21}+1}}+(P_{14}P_{21})^{\beta_4}-1=0$ $P_{52}=\frac{\alpha_1+2-P_{12}}{1+\alpha_1 P_{12}}$
Density Ratio	$\Gamma_{34}=\frac{\rho_3}{\rho_4}=P_{34}^{1/\gamma_4}=\left[P_{14}P_{21}\right]^{1/\gamma_4}$ $\Gamma_{21}=\frac{\rho_2}{\rho_1}=\frac{1+\alpha_1 P_{21}}{\alpha_1+P_{21}}$ $\Gamma_{52}=\frac{\rho_5}{\rho_2}=\frac{1+\alpha_1 P_{52}}{\alpha_1+P_{52}}$
Speed of Sound/Temperature Ratio	$A_{34}=\frac{a_3}{a_4}=\left(\frac{T_3}{T_4}\right)^{1/2}=P_{34}^{\beta_4}$ $A_{21}=\frac{a_2}{a_1}=\left(\frac{T_2}{T_1}\right)^{1/2}=\left[\frac{P_{21}(\alpha_1+P_{21})}{1+\alpha_1 P_{21}}\right]^{1/2}$ $A_{52}=\frac{a_5}{a_2}=\left(\frac{T_5}{T_2}\right)^{1/2}=\left[\frac{P_{52}(\alpha_1+P_{52})}{1+\alpha_1 P_{52}}\right]^{1/2}$
Velocity of Shock wave	$M_1=W_{11}=\left[\beta_1(1+\alpha_1 P_{21})\right]^{1/2}$
Local Mach Number	$M_3=\frac{u_3}{a_3}=\frac{1}{\beta_4\gamma_4}\left[(P_{14}P_{21})^{-\beta_4}-1\right]$ $M_2=\frac{u_2}{a_2}=\frac{(P_{21}-1)}{\gamma_1\left[\beta_1 P_{21}(\alpha_1+P_{21})\right]^{1/2}}$
$\gamma=\frac{C_P}{C_V}$ $\alpha=\frac{\gamma+1}{\gamma-1}$ $\beta=\frac{\gamma-1}{2\gamma}$ E = internal Energy	

Table 2.3.3: Solution for flow in a shock tube with geometry illustrated in Figure 2.3.12 [70].

2.4. Traumatic Brain Injuries

2.4.1. Introduction to TBI

Traumatic Brain Injuries (TBI) are a major cause of mortality and morbidity in the US, with approximately 2 million new cases each year [72]; of these about 1.4 million require emergency visits and hospitalization [73]. The occurrence of TBI is sometimes referred as the “silent epidemic” since the problems arising from the injuries are normally not visible as memory, speech and cognitive impairment [73]. According to a report published by the CDC in 2004 [73], young children (ages 0-4) have the greatest rate of TBI related emergency visit followed by older adolescents (age 15 to 19) and older adults (ages 75 and older). Almost half of the injuries are caused by falls and motor-vehicle accidents [73] and more than 200,000 injuries occur during sport or recreational activities [71]. In fact sport related TBI have been recently increasing even with the use of protecting gears; this is considered an important public health problem as it affects many people and it has potentially disabling consequences. An estimate of the annual number of brain injuries from sports is given in Table 2.4.1 as it relates to the major sports and recreational activities. Additionally, a

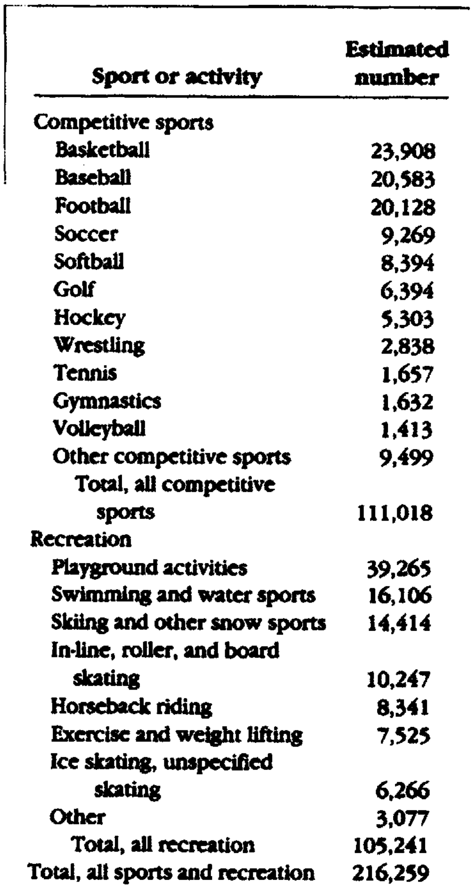

Sport or activity	Estimated number
Competitive sports	
Basketball	23,908
Baseball	20,583
Football	20,128
Soccer	9,269
Softball	8,394
Golf	6,394
Hockey	5,303
Wrestling	2,838
Tennis	1,657
Gymnastics	1,632
Volleyball	1,413
Other competitive sports	9,499
Total, all competitive sports	111,018
Recreation	
Playground activities	39,265
Swimming and water sports	16,106
Skiing and other snow sports	14,414
In-line, roller, and board skating	10,247
Horseback riding	8,341
Exercise and weight lifting	7,525
Ice skating, unspecified skating	6,266
Other	3,077
Total, all recreation	105,241
Total, all sports and recreation	216,259

Table 2.4.1: National Electronic Injury Surveillance System (NEISS) estimates of number of head injuries—US, 1995 [71].

greater number of wounded soldiers are coming back from Iraq and Afghanistan with brain injuries than in any other conflicts [74]. A study conducted between March to August of 2004 found that the incidence of injury to the head and neck of soldier in Iraq was 53% of the total number of injuries [75]. A table with the percentage of wound location for previous wars is given in Table 2.4.2. The cause of the increase in head and neck trauma is due to their vulnerability, as body armor evolves and becomes more sophisticated the head and neck remain relatively unprotected from large impacts/accelerations [75]. Whatever the cause of the injury, TBI are not only devastating for the victims and their family but they also place an enormous economical and social burden on society [72]. Since a cure for brain injuries is not currently available, it is especially important to develop ways to try to minimize their occurrence and severity.

WOUND LOCATIONS IN PREVIOUS CONFLICTS

	Wound Location (%)			
	Head and Neck	Chest	Abdomen	Extremity
World War II	25	13	9	53
Korean War	19	8	7	53
Vietnam War	15	8	5	55
Gulf War	20.3	5.8	9.3	90
Somalia	13.3	6.6	3.3	74.7

Table 2.4.2: Location of injuries sustained during previous wars. Percentages that add up to more than 100% reflect calculations based on multiple injury sites per patient [75].

Traumatic Brain Injuries are classified as mild, moderate and severe:

- Mild TBI or concussions cannot normally be seen on brain imagining and are classified as causing loss of consciousness that last for less than 1 minute or amnesia for less than 24 hours.
- Moderate TBI cause loss of consciousness that last 1 to 24 hr or amnesia for one to seven days.

- Severe TBI cause loss of consciousness for more than 24 hr or amnesia for more than a week.

Computed tomography (CT) is normally used for brain imaging but many forms of brain injuries are not detectable by CT scans, especially when injuries occur in the brainstem [76]; this results in difficult diagnoses and 'hard to predict' outcomes for patients with TBI. Magnetic Resonance Imaging (MRI) has been used recently to visualize the extent of the brain injuries but unfortunately MRI machines that are compatible with life support systems (as many of the patients required) are not readily available [76].

There are two types of injuries that are commonly encounter: focal and diffuse. Focal injuries are localized tissue damage such as contusion and intracranial haematomas while diffuse injuries are associated with axonal, neural injury and brain-swelling. Focal injuries are normally caused by short-duration, high rate loadings and can occur without the head being struck, as by indirect acceleration. A well known example of these types of injuries is Acute Subdural Heamatomas (ASDH) that result from shaken baby syndrome. Diffuse injury usually occurs under distributed loading conditions and they are created by lower rates of loading but of more prolonged duration. The most common diffuse injury, Diffuse Axonal Injury (DAI) is caused by the shearing of the axonal tissue where the extent of the damage depends both on the strain and strain rate experienced by the brain during impact [77].

2.4.2. Brain Injury Mechanism

The major mechanisms for brain injuries are the positive pressure, negative pressure, and shear stresses that are created in the brain when impacts or relative motion of the brain occur upon an impact [1]. The positive and negative pressures are associated with what are called the coup and countercoup: the positive pressure is found to contuse or bruise the brain, while the negative pressure exerts tensile loading or cavitations. Contusions due to coup and countercoup are usually seen on the surface of the brain; shear stresses, on the other hand, are normally associated with diffuse injuries, especially DAI and are found throughout the brain and at the brainstem. The shear stresses that develop in the brain are found to be a result of both angular and linear accelerations [1], while the pressure gradients within the intracranial cavity, and the location of the coup and countercoup, have shown correlation with the translational acceleration of the head [72]. This was confirmed by the study of concussions or mild TBI suffered by professional football players; a reconstruction of the kinematics from the impacts was used together with a finite element model of the head to study the mechanism of brain injury [72]. Zhang et al. were able to relate the shear stresses and the rotational acceleration in the brain due to an impact with the probability of injury; these relations are shown in Figure. 2.4.1.

Some studies [78, 79] have related the occurrence of brain injury to with the relative displacement of the brain inside the skull. Gilchrist [77] argues that the magnitude of the brain displacement and the degree of damage can be gauged by the ratio between the duration of the loading and the natural period of the brain:

- Ratio <1: the same impulse and duration will result in the same injury, even if the maximum force/acceleration varies over a wide range, i.e. the impact event has concluded before the structure reacts.
- Ratio > 1: the same maximum force/acceleration will result in the same injury, even if the impulse and duration varies over a wide range.

- Ratio ~ 1: neither the impulse or maximum force/acceleration alone can characterize the sensitivity and the entire force-time function must be considered.

A sketch of how increasing impact duration affects the peak acceleration is shown in Figure 2.4.2.

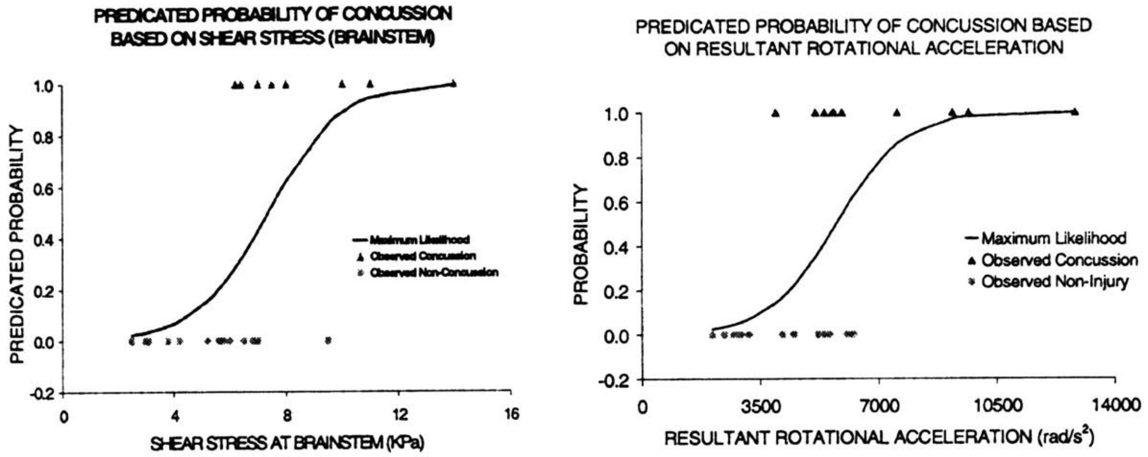

Figure. 2.4.1: Predicted injury probability based on shear stress on the brainstem predicted by the FE model and the input acceleration of the head [72].

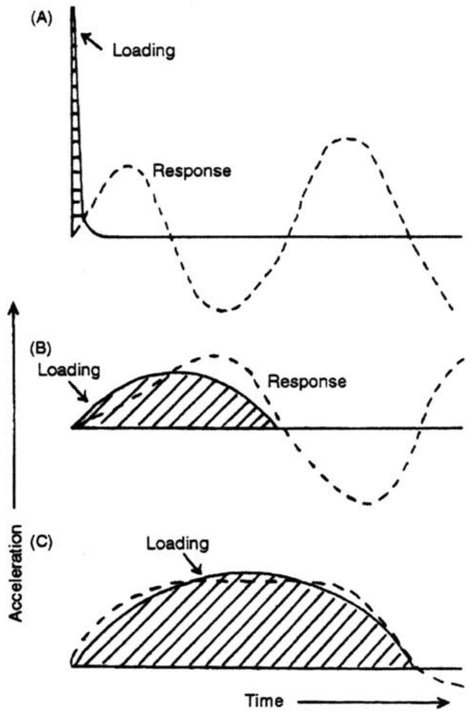

Figure 2.4.2: Loading response associated with a short duration impact (A), a medium duration impact (B) and a long duration impact [77].

Many studies have also been conducted in vitro [80, 81] to understand brain injuries at the cellular level, especially DAI. A study of a three-dimensional neural culture exposed to high strain rate injuries has shown that cell death is attributed to the stretching of neural components that arises as a result of a combination of strain and strain rates [81]. A study of the uniaxial stretching response of cell cultures has shown that local strains associated with injuries can be up to 70 % and strain rates of 90 s^{-1} [80]. This is somewhat higher than the limits proposed by Morrison [82] which correspond to macroscopic strain of 10-50 % and macroscopic strain rates of 10-50 s^{-1}; the difference is explained by the inhomogeneity of the brain tissue at small scale [80].

2.4.3. Human Tolerance to Injury

In the early studies of the dynamic loading effects on the brain, human cadaver, human volunteers and anesthetized animals were used to develop tolerance curves and criteria [83]. Some of these early experiments were carried out by Stapp who exposed a number of human volunteers to linear decelerations (up to 45g for 0.1-0.4 sec) on moving sleds. Eiband used this data and the results from animal experiments to develop a whole-body tolerance curve, shown in Figure 2.4.3, which related the max acceleration with the time duration of the event to the level of injury [83].

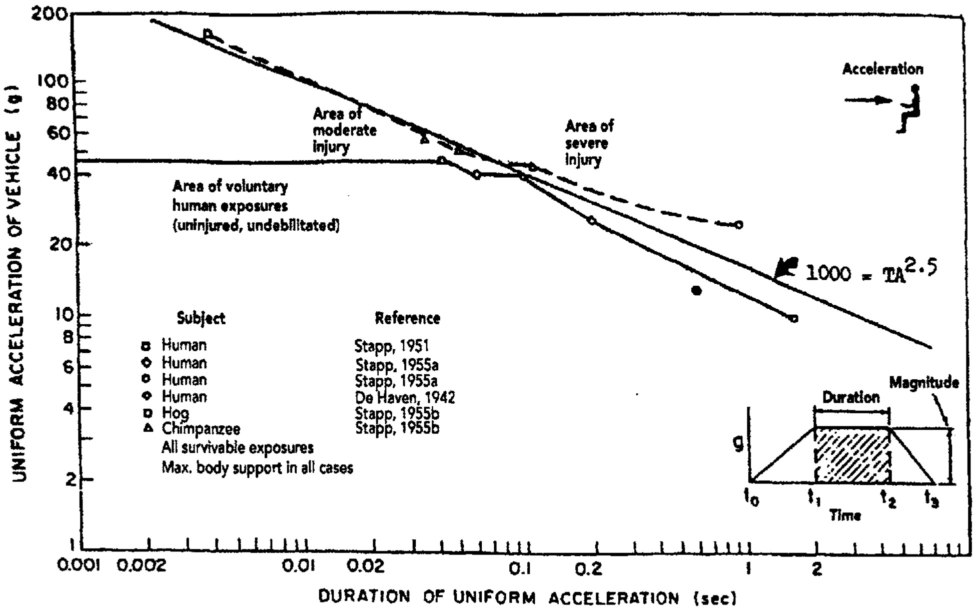

Figure 2.4.3: Whole body tolerance curve to frontal acceleration of a subject seated in a sled to a trapezoidal acceleration [83].

A more recent, commonly used brain injury tolerance criteria, the Head Injury Criterion (HIC), based on the Wayne State University tolerance curve (shown in Figure 2.4.4.) was developed by studying the effect of linear acceleration and its time duration on skull fracture and concussion from animals and human sled experiments. The HIC, as currently adopted by the US federal government, is as follows:

$$\mathrm{HIC} = \frac{\left[\int_{T_1}^{T_2} a(t)\,dt\right]^{2.5}}{(T_2 - T_1)} \leq 1000 \qquad (2.50)$$

where T_1 is the initial time of impact, T_2 is the final time and *a(t)* is the time varying acceleration. HIC is not injury specific, nor does it give any information about the severity of the injury and the load direction; additionally, angular velocities and accelerations have been shown to be as important as linear accelerations in causing brain injuries. Currently no criteria based on angular acceleration have been adopted, but many studies have been conducted and limits proposed; Table 2.4.3 summarizes some of the proposed limits for angular and linear acceleration.

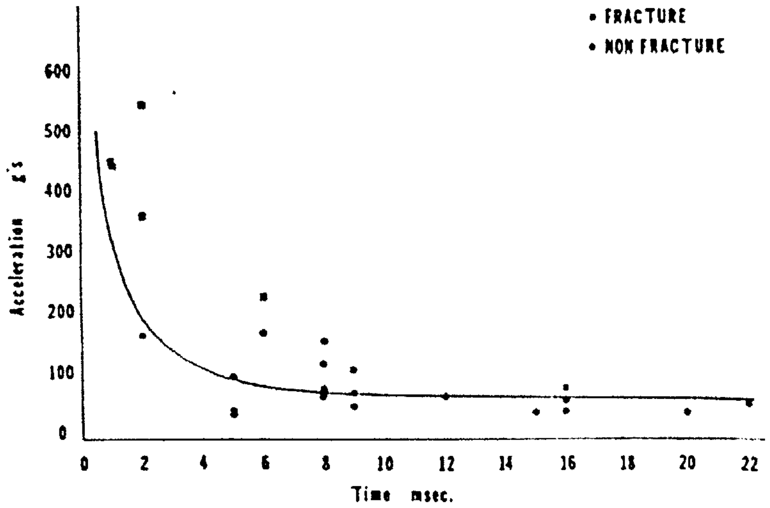

Figure 2.4.4: The Wayne State Tolerance Curve which illustrates the severity of injury as fracture (full squares) and non –fracture (full dots) as a function of linear acceleration (in g's) vs duration of the acceleration. The black line represent the transition between non-fracture to fracture [1].

Reference	Type of Tests	Proposed limits
Ommaya 1971 [84]	Primate Tests	1800 rad/s^2 60-70 rad/s
Lowehielm 1975 [85]	Cadaver tests and mathematical model	4500 rad/s^2 50-70 rad/s
Ewing 1975 [86]	Volunteers	1700 rad/s^2 32 rad/s
Pincemaille 1989 [87]	Volunteers Boxers	16000 rad/s^2 25 rad/s
Zhang 2004 [72]	Accident reconstruction and computational model	5900 rad/s^2 (50 % probability of injury)

Table 2.4.3 Summary of proposed tolerance limits for angular and linear accelerations.

As mentioned earlier the HIC is not injury specific, nor does it take into account the brain weight. Margulies and Thibault [79] developed a tolerance criterion for DAI in human that incorporates all these factors. By using animal model experiments, physical model studies and simulations of analytical model they were able to relate the injury in the brain to the structural response for any loading. Their results, shown in Figure 2.4.5, are found to be in agreement with data obtained found in the study of the effect of rotational acceleration in volunteer boxers [87]. Strains between 0.05-0.1 were found to be associated with severe TBI.

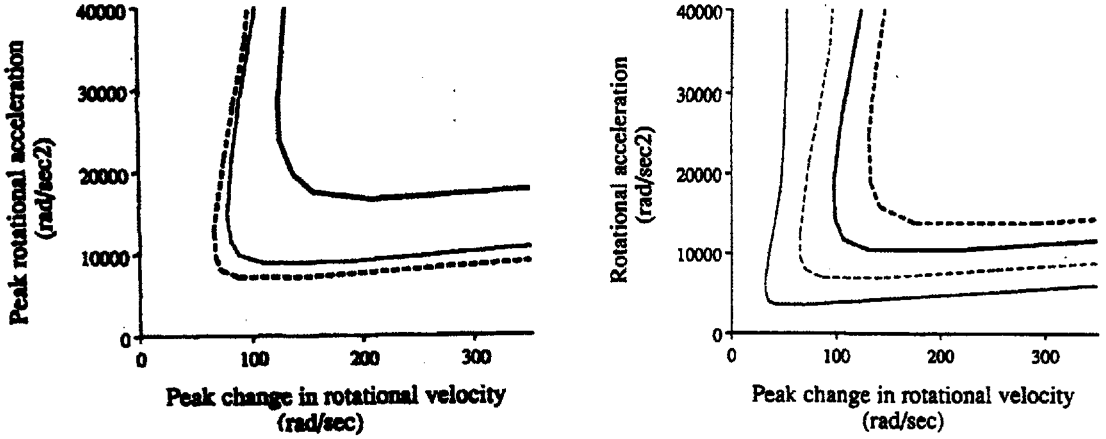

Figure 2.4.5: (right) DAI thresholds for a range of human brain masses. DAI tolerances for infant (500g, heavy solid line) and adult (1067 g solid line; 1400 g dashed line). (left) Influence of critical strain value on the DAI tolerance. Small critical strain may correspond to mild form of axonal injury. Critical strains: 0.05 (solid line), 0.10 (dashed line), 0.15 (heavy solid line), 0.20 (heavy dashed line) [79].

Recently, finite element computational models of the human head have replaced much of the animal and human volunteer testing. Some of these models are very complex, such as the one developed by Zhou et al. [88] which models the scalp, three layered skull, dura, falx, tentorium, pia, cerebral spinal fluid, venous sinuses, ventricles, cerebrum (gray and white matter) cerebellum, brain stem, and parasagittal bridging veins. These models are used to match the kinematics of head injuries, as experienced for example by football players [72], to understand the mechanism of injury and develop tolerance limits.

2.5. Conclusions

The background study conducted in the field of STF rheology, reticulated foams, TBI protection and blast wave mitigation has lead us to a number of issues that are relevant to this work:

1. The shear thickening mechanism of concentrated suspensions is dependent on a large number of parameters but the critical non-dimensional shear stress can be defined as: $\tau_{cr}^{elec} = Pe_{cr}^{elec} = \frac{3\pi\mu a^3 \dot{\gamma}/2h}{2\pi\varepsilon_0\varepsilon_r\psi_S^2\kappa\, a/2}$ as described by equation (2.6).
2. Open cell polyurethane foam can be used to magnify the stress response of any fluid by a factor proportional to $\left(L/l\right)^2$. Additionally, the stress contribution from the fluid is also proportional to $\eta\left(\dot{\varepsilon}_{loc}\right)$ and therefore is further increase by the use of STF.
3. Primary Blast injuries are caused by the interaction between the chest cavity and the stress wave that is transmitted to the chest as it is subjected to a blast wave. The parameter that has been linked to primary lung injuries is the rate of pressure

rise; in fact when the pressure gradient became too big for the alveoli to sustain, they burst and bleeding occurs.

4. Traumatic Brain Injury (TBI) is a serious and potentially fatal injury that results from rapid accelerations of the head, and subjects the brain to high intracranial pressure and shear stresses. Some attempts have been made to investigate the threshold velocity and acceleration for human tolerance but not a universally criteria specific to the head exist to date. A 50% probability of intracranial injury has been reported to be 50 MPa.

In the following work the combination of particles and solvent were picked to give the desired shear thickening fluid response; details on the fluid composition and its rheological properties are discusses in Chapter 3. To fully exploit the fluid potential for energy absorption we utilized reticulated open cell foams as the enveloping geometry. A discussion on the characterization of the foam and the fluid filled composite at low strain rates is given in Chapter 4. The possible application of these fluid filled composites for Traumatic Brian Injuries protection will be presented in Chapter 5. Particular attention has been given to match the experiments impact kinetic energies and loads with the magnitude of the energy resulting in TBI. Chapter 6 will discuss the application of these composites for Primary Blast Injuries. Shock tube experiments were used to create shock waves that matched both magnitude and duration of real blast.

3. Shear-thickening fluids: Rheology and Characterization

3.1. MATERIALS AND CHARACTERIZATION

3.1.1. Particles Characterization

The shear thickening fluids (STF) used in this study were composed of silica particles dispersed in ethylene glycol (EG). Two types of silica particles were used: one monodisperse and the other polydisperse. The monodisperse silica particles were supplied by Fuso chemical in powder form with a nominal diameter of 300 nm. A micrograph of the particles, taken by SEM, is shown in Figure 3.1.1 (a), and the corresponding particle size distribution (PSD) obtained by dynamic light scattering is shown in Figure 3.1.1(b). The density of the particles was determined to be ρ_s= 2.1 gr/cm^3, and their zeta potential in water, measured with a Brookhaven Zeta PALS, was found to be ζ= -77.6 mV.

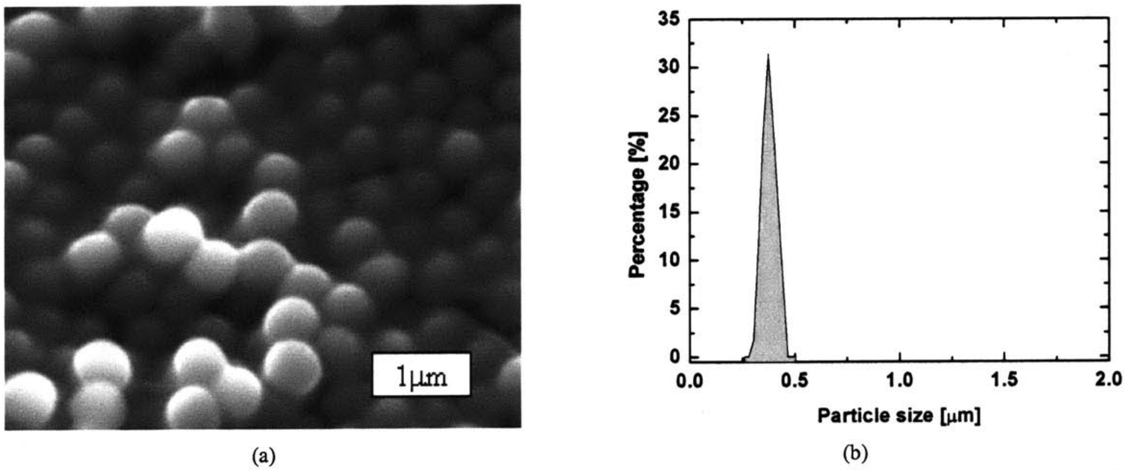

(a) (b)

Figure 3.1.1: (a) Micrograph of monodisperse silica particles with a mean diameter of d = 300 ± 31 nm. (b) Particle size distribution of the same silica particles.

The second type of silica particles, supplied in powder form by US Silica, is polydisperse and faceted in shape with nominal size of 1 μm. The density was measured to be 2.6 gr/cm^3 and the zeta potential ζ= -79.8mV. A micrograph and PSD of these particles are shown in Figure 3.1.2.

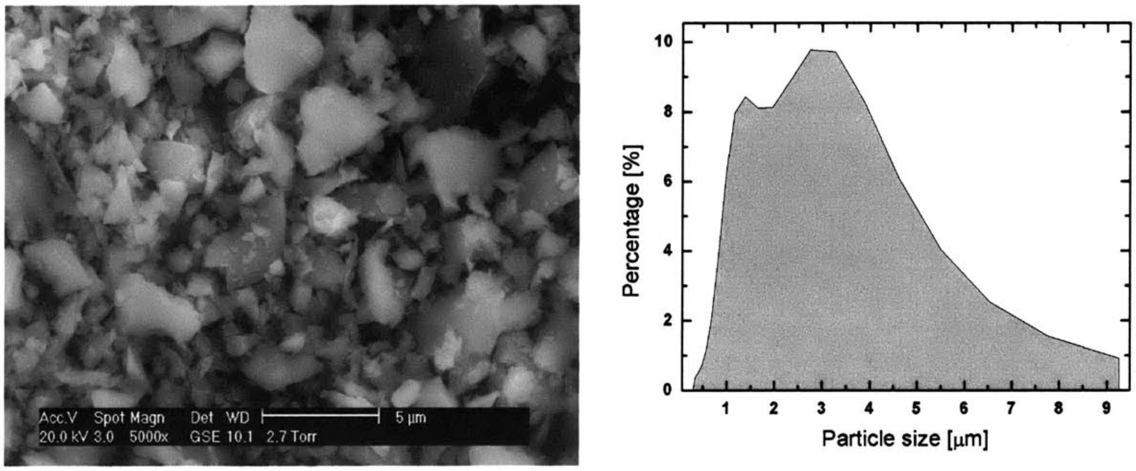

(a) (b)

Figure 3.1.2 (a) Micrograph of polydisperse silica particles with nominal diameter of 1 µm. (b) Particle size distribution of these silica particles.

3.1.2. Preparation Techniques

The two different types of particles were each individually dispersed in ethylene glycol. At first the particles were suspended at relatively low volume fraction (not greater than 20 %) through vigorous mixing (with a Vortex Mixer) followed by sonication to ensure complete dispersion. The lower volume fraction suspension was then centrifuged and the supernatant removed. The resulting centrifuged suspension is then diluted to the desired volume fraction and again, vigorous mixing and sonification were applied to ensure homogeneity. The monodisperse silica suspension final volume fraction was 60% and up to 47 % for the polydisperse one.

3.2. SHEAR RHEOLOGY

3.2.1. Steady Shear Rheology

Steady shear experiments were carried out with the AR2000 stress controlled rheometer with a plate-plate geometry. The polydisperse suspension was found to shear thicken at a volume fraction ϕ > 40%, and extreme shear thickening was observed at ϕ > 47%. This volume fraction is relatively low if compared to monodisperse spherical particles suspensions. In fact, the monodisperse suspension starts to show shear thickening at ϕ = 54% and extreme shear thickening does not occur until up to a volume fraction ϕ ≥ 58-61%. Figure 3.2.1 illustrates the viscosity of both suspensions at two volume fraction; the viscosity of the carrier fluid, ethylene glycol, is also plotted for reference.

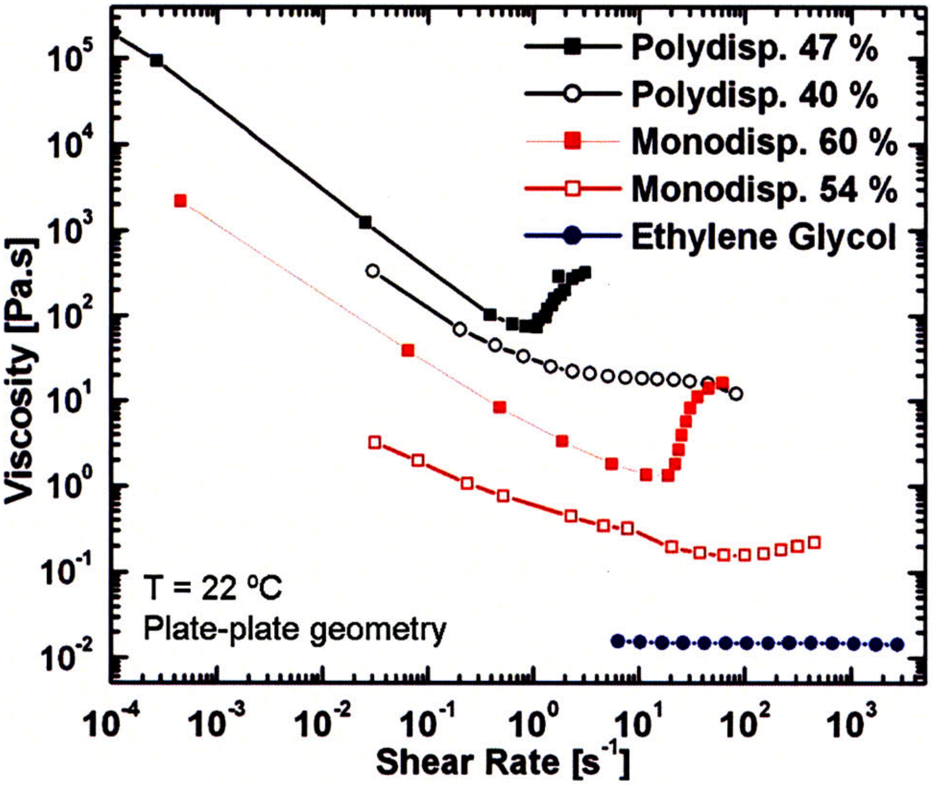

Figure 3.2.1 Rheological response of both silica suspensions in steady shear flow. The rheology of different volume fraction suspensions is shown to indicate the critical volume fraction for the appearance of shear thickening effect. (in blue) Viscosity of the solvent ethylene glycol.

The difference in volume fraction for the onset of shear thickening is primarily due to the different particle shape of the two suspensions, as discussed in section 2.1.3.4. In fact, the more faceted the particles are, the more likely it is for them to jam into each other and form hydroclusters even at relatively low ϕ.

A large difference in the magnitude of the viscosity of the two suspensions is also found. As shown in Figure 3.2.1, even at relatively low volume fraction ($\phi \approx 40$ % for polydisperse suspension and $\phi \approx 54$ % for the monodisperse one) the viscosity of the polydisperse suspension is two orders of magnitude greater than the monodisperse. This phenomenon is again related to the shape of the particles in suspension. Intuitively, it takes a greater stress to move the faceted particles past each other than to do the same for smooth spherical particles.

A third important difference between the two suspensions is the value of the critical stress for the onset of shear thickening. This is consistent with the fact, derived from scaling arguments as described in section 2.1.2.3, that suspensions of smaller particles will require a greater critical stress. Particularly for the electrostatically stabilized particles studied here we see from equation (2.6) that $\tau_{crit} \sim a^{-2}$; this has also been confirm through experimentations as shown by Maranzano [10] and reproduced in Figure 2.1.6. This trend is obviously not rigorously followed by the two suspensions because of different particles characteristics: charge, shape, surface roughness, etc.

The rheological data of both suspensions (at high ϕ) can be fitted to an appropriate generalized Newtonian fluid constitutive model. In order to capture the yield stress seen in both suspensions the Cross model [89] was utilized with a modification of the exponent *n* to account for the shear thickening of the suspension. The equation used is as follows:

$$\tau = K\dot{\gamma}^{n} + \frac{\dot{\gamma}(\eta_0 - \eta_\infty)}{1+\left(\dfrac{\dot{\gamma}}{\dot{\gamma}_c}\right)} \qquad (3.1)$$

where σ represent the shear stress and $\dot{\gamma}$ the shear rate. K, n, $\eta_0 - \eta_\infty$ and $\dot{\gamma}_c$ are found by fitting the model to the data and these values for both dispersions are reported in Table 3.2.1.

	K (Pa.s^n)	*n*	η_0-η_∞ (Pa.s)	$\dot{\gamma}_c$ (1/s)
Monodisperse	$5.0 \cdot 10^{-4}$	3.7	$4.5 \cdot 10^{3}$	$7.5 \cdot 10^{-4}$
Polydisperse	43	3.2	$3.5 \cdot 10^{5}$	$1.0 \cdot 10^{-4}$

Table 3.2.1: Fitted values of the modified Cross model for the monodisperse and polydisperse silica suspensions.

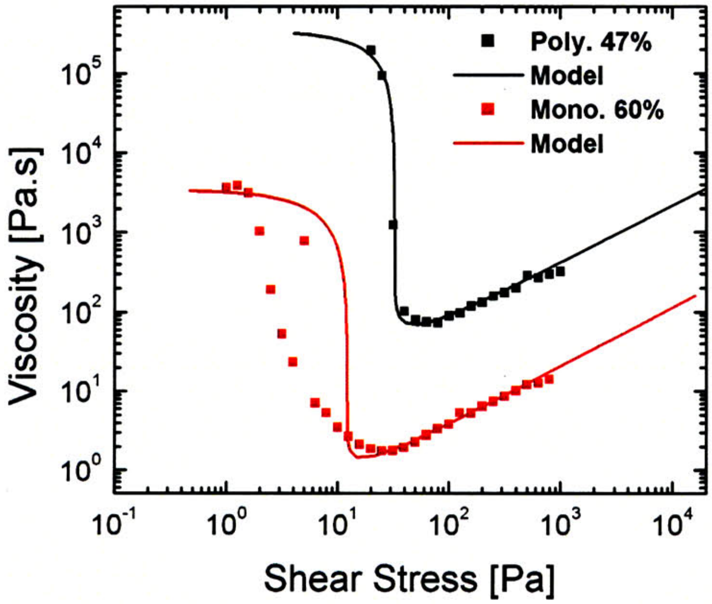

Figure 3.2.2: Steady shear rheology of both suspension measured with a plate-plate geometry at T= 22 °C and their Cross model fit.

The model predictions can be readily compared with the measured data by plotting the steady shear viscosity $\eta \equiv \tau / \dot{\gamma}$ as a function of the applied shear stress as shown in Figure 3.2.2. This modified model captures very well the behavior of the polydisperse suspension, but it does not correctly capture the more gradual viscosity drop of the monodisperse suspension in the shear thinning region at a shear stress $\tau \sim 10$ Pa.

The dependence of the viscosity of the shear thickening fluid on temperature was also studied. According to the scaling arguments derived in section 2.1.2.3 the shear thickening effect should depend on temperature as the onset of thickening directly depends on the carrier fluid viscosity. This is precisely what we observe in Figure 3.2.3 which illustrates the dependence on temperature for the monodisperse silica suspension.

The temperature dependence of the suspension viscosity can be collapsed onto a mastercurve by applying the proper scaling. The shear stress can be scaled with thermal energy to give the Peclet number, defined as $Pe = \frac{\tau a^3}{k_B T}$ in section 2.1.2.3, on the horizontal axis. The magnitude of the viscosity is scaled with the temperature shift factor, a_T ,to define a reduced viscosity as $\eta_r = \eta / a_T$, on the horizontal axis as shown in Figure 3.2.4.

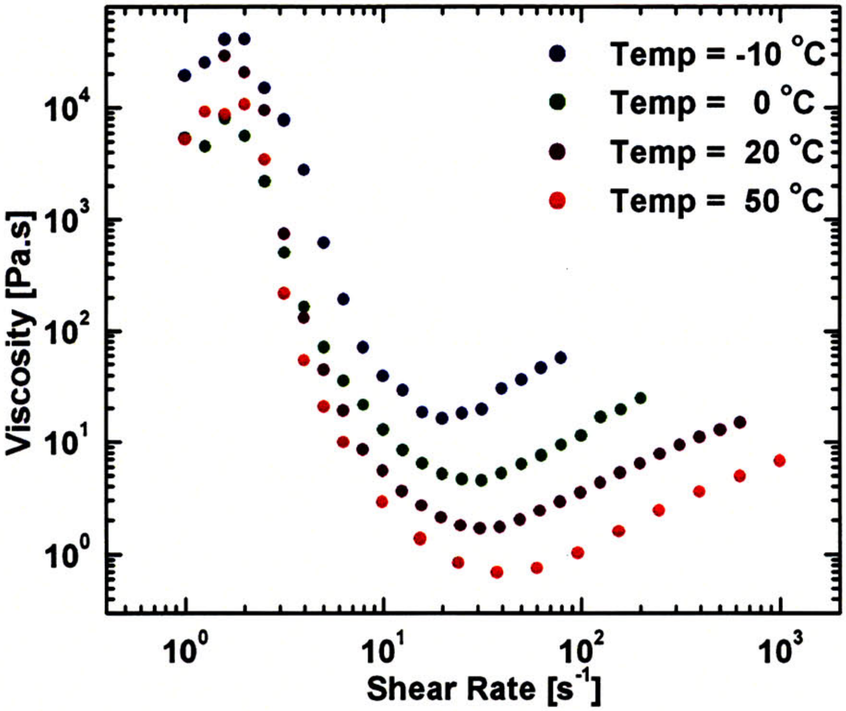

Figure 3.2.3: Temperature dependence on the viscosity of monodisperse silica suspension of volume fraction of ϕ = 60%

With the help of these scaling factors we find that the shift in the viscosity function $\eta_r(Pe)$ is coming directly and only from the variation of solvent viscosity with temperature. In fact as seen in the inset in Figure 3.2.4, the dependence of the shift factor on temperature for the fluid coincide with the dependence of the matrix fluid suspension, ethylene glycol.

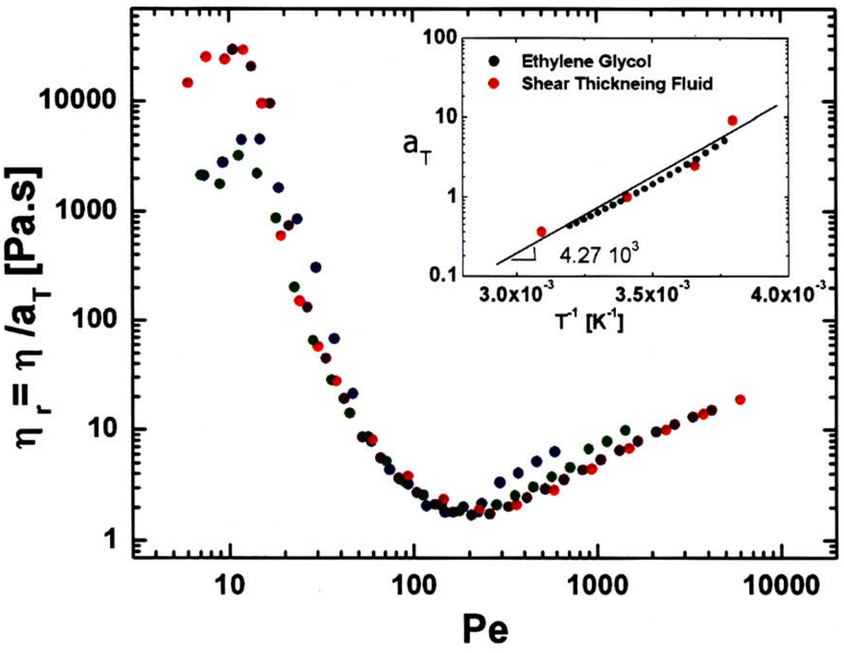

Figure 3.2.4: Rheology of the monodisperse silica suspension at various temperature plotted as reduced viscosity versus Pe at a reference temperature $T_0 = 20$ °C. (top-right) shift factor as a function of 1/T of the shear thickening fluids and the solvent ethylene glycol.

3.2.2. Dynamic Shear Rheology

The linear viscoelastic properties of the monodisperse silica suspension have also been extensively studied using oscillatory shear flow. These experiments show that the dynamic complex viscosity can be directly related to the steady shear viscosity as observed in constitutive models for yield stress materials. In particular when the magnitude of the complex viscosity, $|\eta^*|$, is plotted as a function of the product $\omega\gamma_0$ (corresponding to the magnitude of the maximum shear rate) the curve for the steady shear viscosity and complex shear viscosity superimpose as illustrated in Figure 3.2.5. The product $\omega\gamma_0$ represents the magnitude of the 'dynamic shear rate'. This correspondence is known as the Delaware-Rutgers rule [32], as described in section 2.1.4.2 which can be expressed as:

$$\eta(\dot{\gamma}) = \left|\eta^*(\gamma_0\omega)\right| \tag{3.2}$$

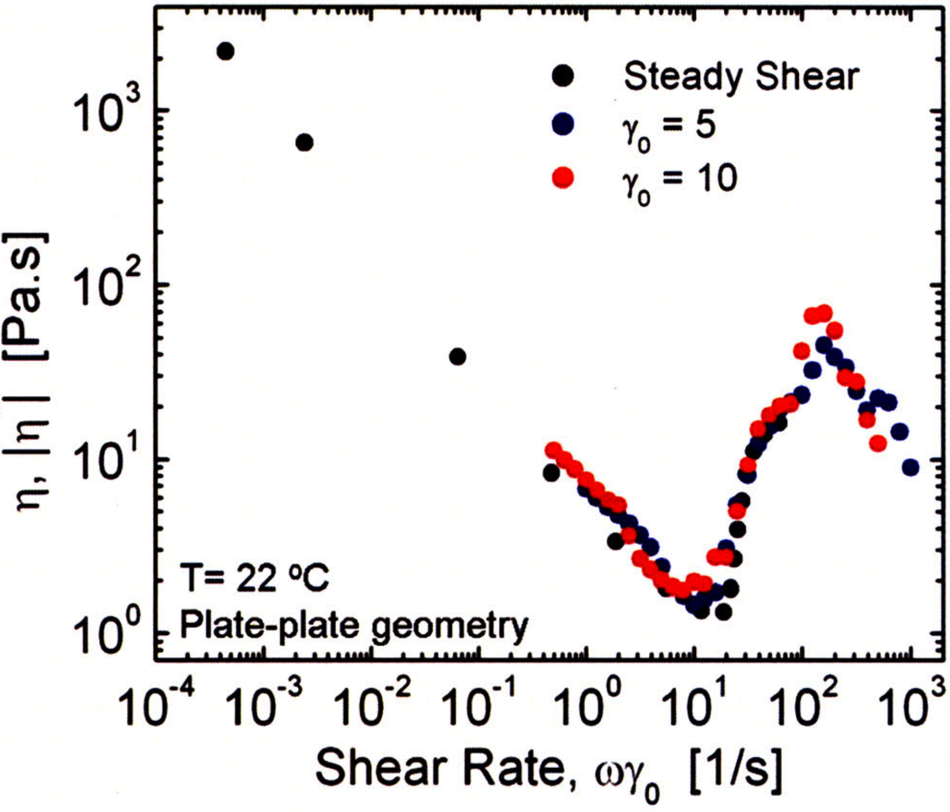

Figure 3.2.5: Dynamic shear response of monodisperse silica suspension, the dynamic response of the fluid is compared to the steady shear viscosity.

This finding is particularly important because it shows that there are two ways to achieve thickening; the first methods corresponds to shearing at a steady rate $\dot{\gamma} > \dot{\gamma}_{crit} \approx$ 10 s^{-1} and the second by imposing oscillatory shearing frequencies or strains at $(\gamma_0\omega) > \dot{\gamma}_{crit}$. There are of course many combinations of $\gamma_0\omega$ that can induce the fluid to thicken, and in order to study this in a more systematic way we represent the dynamic viscosity as both a function of strain and frequency using a Pipkin diagram [90] as seen in Figure 3.2.6. The value of complex viscosity is plotted as function of both parameters and the figure has been color coded; vertical lines in the plot corresponds to strain sweeps, while horizontal ones to frequency sweeps. This representation of the data also suggests that there is a limit on how small of a strain is necessary for the suspension to shear thicken. In fact, as found in various work on shear thickening studies by Wagner {Lee, 2003 #1} and Laun {Laun, 1991 #8} (but sometimes attributed to wall slip effects) a minimal strain of order unity is found to be necessary to achieve thickening of the suspension, see section 2.1.4.2. The contour plot of Figure 3.2.6 illustrated a region of shear thinning (bottom left) until a critical point is reached (critical shear rate) and the suspension shear thicken (upper right corner.) Contour lines with slope -1 are found to be of equal viscosity; this is related to the fact that a line of slope -1 corresponds to a set of equal "dynamic shear rate" $\omega\gamma_0$ as predicted by the Delaware Rutgers rule.

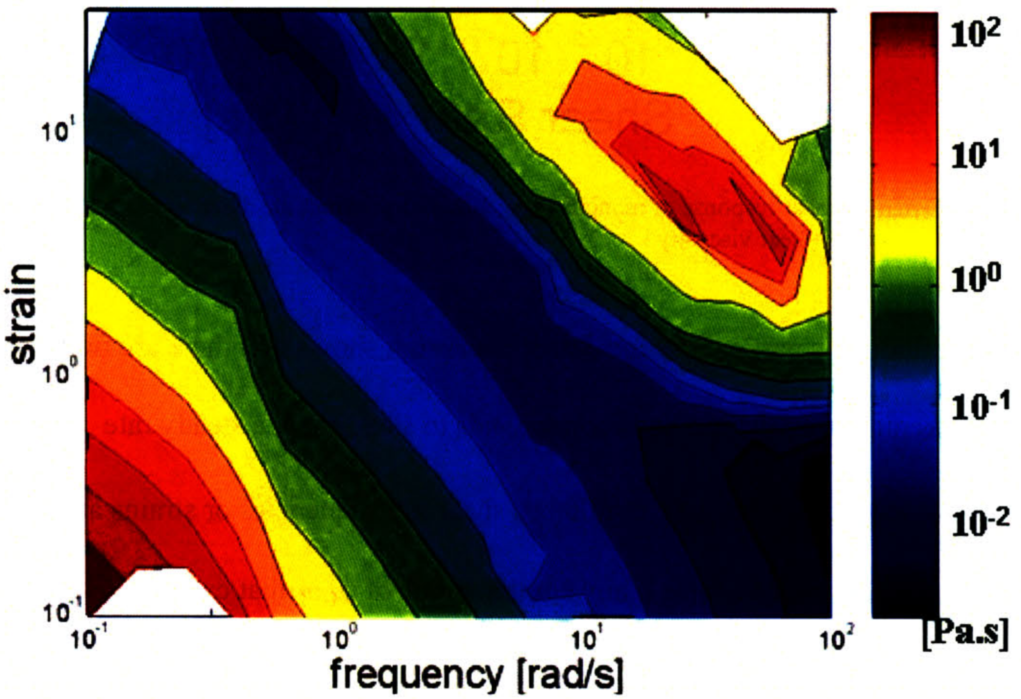

Figure 3.2.6: Pipkin diagram of dynamic viscosity as a function of both strain and frequency for 300 nm silica suspension at 60% volume fraction.

3.3. Extensional Flow Rheology

The extensional viscosity of the shear thickening fluids was measured with a filament stretching rheometer (FiSER), as shown in Figure 3.3.1. This instrument comprises of two circular plates, the bottom stationary, and the top able to move upward in an exponential trajectory. The fluid sample is loaded between the two plates and stretched axially. The bottom plate is attached to a load cell that records the axial force as a function of time. The instrument also measures the value of the midplane diameter by using a laser micrometer mounted on a separate moving stage. As the top plate moves, the laser micrometer stage travels at half the speed; this ensures that the laser micrometer always reads the midplane diameter. From the measured diameter reading we can calculate the rate of strain as follows:

$$\dot{\varepsilon}_{mid} = -\frac{2}{D_{mid}(t)}\frac{\mathrm{d}D_{mid}(t)}{\mathrm{d}t} \tag{3.3}$$

it is our goal to be able to measure extensional viscosity at constant strain rates, which means that the top plate needs to be moving up exponentially with position given by:

$$L = L_0 e^{\dot{\varepsilon} t} \tag{3.4}$$

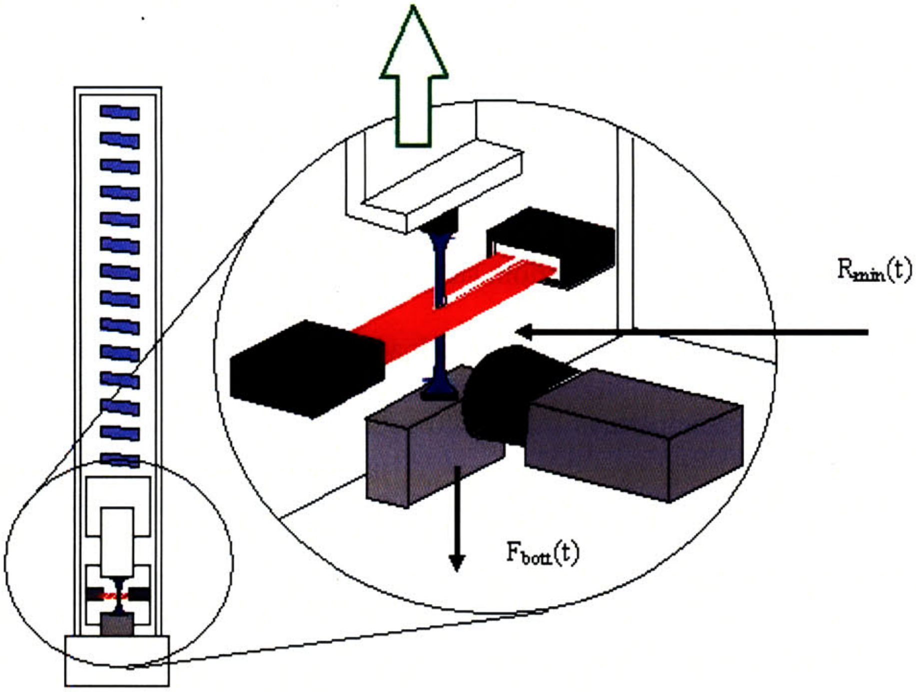

Figure 3.3.1: Filament stretching extensional rheometer (FiSER) reproduced from Shelley Anna (PhD thesis, 2001)

The force measurement readings at the bottom plate also need to be adjusted to account for gravity and surface tension effects. An expression for the force balance [91], can be used to estimate the contribution from each component to the total force experienced by the fluid. If inertia is neglected we can write:

$$\tau_{zz} = \frac{\rho(g+\ddot{L}/2)V_0}{2\pi R_s^2} + \frac{F_{bott} - \rho(g+\ddot{L}/2)V_0}{\pi R_s^2} + \frac{\sigma}{R_s}\left(1 + R_s R_s^{''}\right) \tag{3.5}$$

where $\ddot{L}$ is the acceleration of the plate, g is gravity, R_s is radius of the filament. By ignoring the axial curvature surface tension term that contains $R_s^{''}$ and by rearranging (3.5) we obtained and expression for the viscous force:

$$F_{viscous} = F_{bott} - \frac{\rho(g + \ddot{L}/_2)V_0}{2} + \pi\sigma R_s \tag{3.6}$$

By using the direct measures of diameter as function of time together with the viscous force measurements, curves of stress growth with strain or strain rate can then be constructed. Experiments carried out for the monodisperse silica suspension show two different flow regimes: at low extension rates the suspension responds as a viscous rate-thinning fluid, whereas beyond a critical extension rate, the suspension strain-hardens and ultimately fractures in a solid-like fashion. This behavior is clearly observable from the series of images taken during the experiments as shown in Figure 3.3.2. Curves of the filament diameter as a function of time for two different extension rates are shown in Figure 3.3.3.

The stress-strain behavior of the monodisperse silica suspension is shown in Figure 3.3.4 where each curve corresponds to a different nominal strain rate. The oscillation of the stress values seen at high extension rate can be related to the mechanical vibrations of the FiSER vibrations during high rate experiments. The characteristic stress for each extension rate was obtained by averaging the stress measurements (data before strain of 0.1 were not included into the averages calculation) as follows:

$$\tau_{avg} = \frac{\int_{0.1}^{\varepsilon_{\max}} \tau_{zz} \, d\varepsilon}{\left(\varepsilon_{\max} - 0.1\right)} \tag{3.7}$$

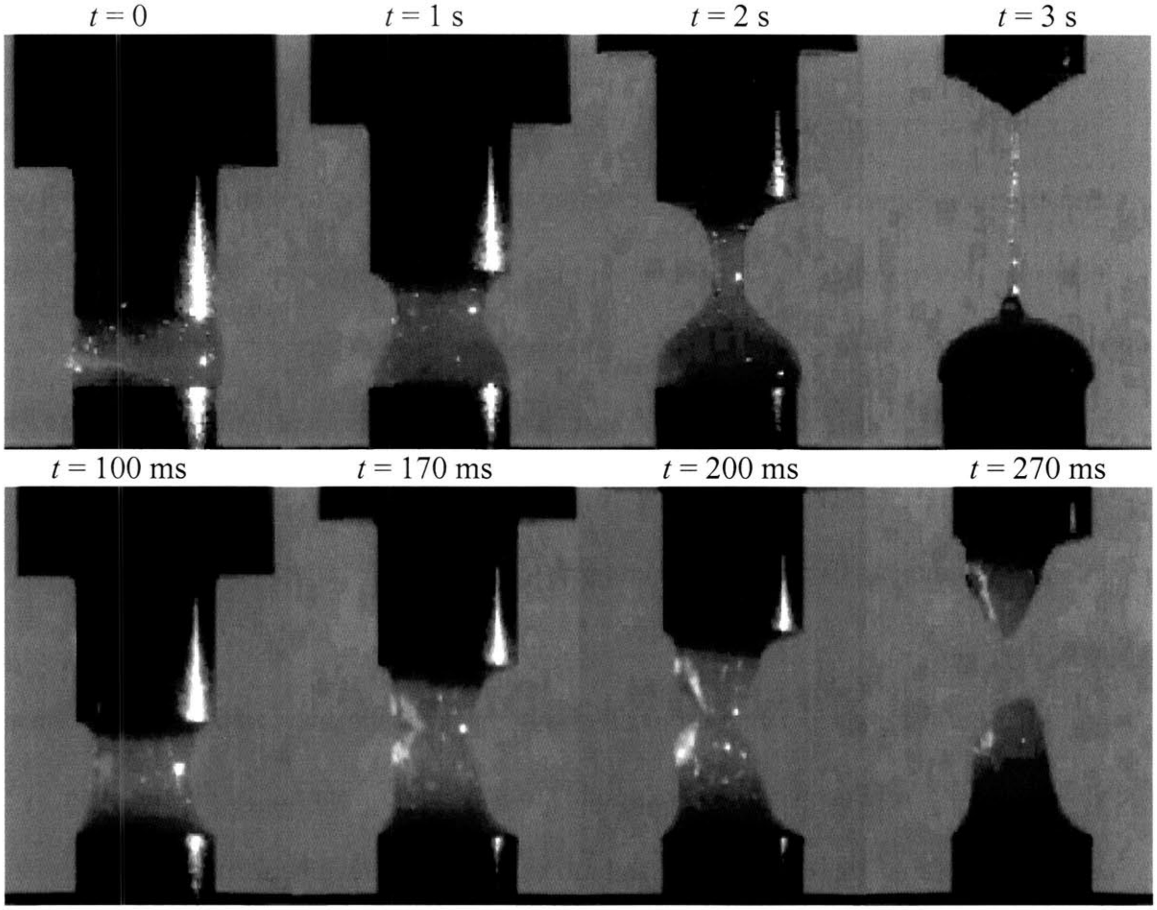

Figure 3.3.2: Video images from extensional flow experiments for the monodisperse silica suspension at ϕ of 60%, (Top) Imposed strain rate $\dot{E}$ =0.5 s^{-1}, (Bottom) Strain rate $\dot{E} = 6$ s^{-1}. The plate radius is 3 mm

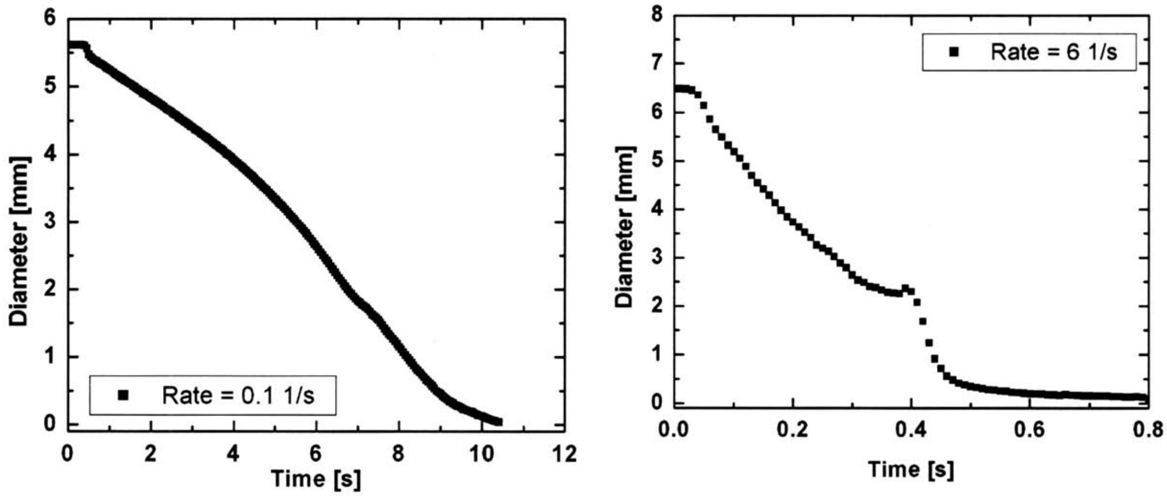

Figure 3.3.3 Diameter vs. time data for the monodisperse silica suspension at extension rate (a) $\dot{E} = 0.1$ s^{-1} and $\dot{E}$ (b)= 6 s^{-1}

The characteristic stresses obtained from Figure 3.3.4 were then used to find nominal extensional viscosities as:

$$\eta_E = \frac{\tau_{avg.}}{\dot{\varepsilon}_{nom.}} \tag{3.8}$$

The resulting values are plotted in Figure 3.3.5. We note that the values of viscosity measured in extension are comparable qualitatively to three time the shear viscosity as expected for a generalized Newtonian fluid, however there is a greater and earlier (at smaller strain rates) thickening response in uniaxial extension. This is not consistent with the computational finding from Sami {Sami, 1996 #9}, but one possible explanation for the difference may lay in the use of nominal strain rates rather than true strain rates, due to experimental limitations. In fact, we expect the true extensional strain rates to be greater than the nominal, which would effectively shift the viscosity-strain rate curve to the right, and also (because viscosity is calculated by dividing by strain rates) down closer to the shear viscosity curve.

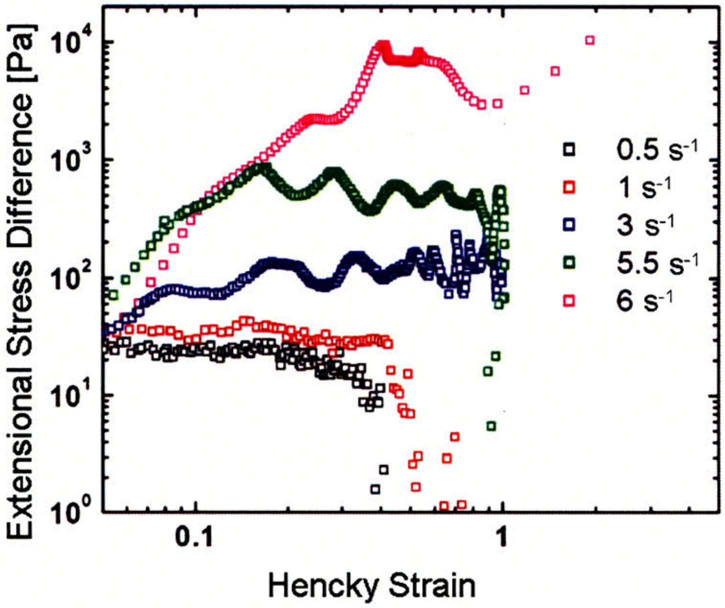

Figure 3.3.4: Extensional stress growth curves from extensional flow experiments of 60% volume fraction silica suspension. Extension rates ranges from 0.5-6 s^{-1}.

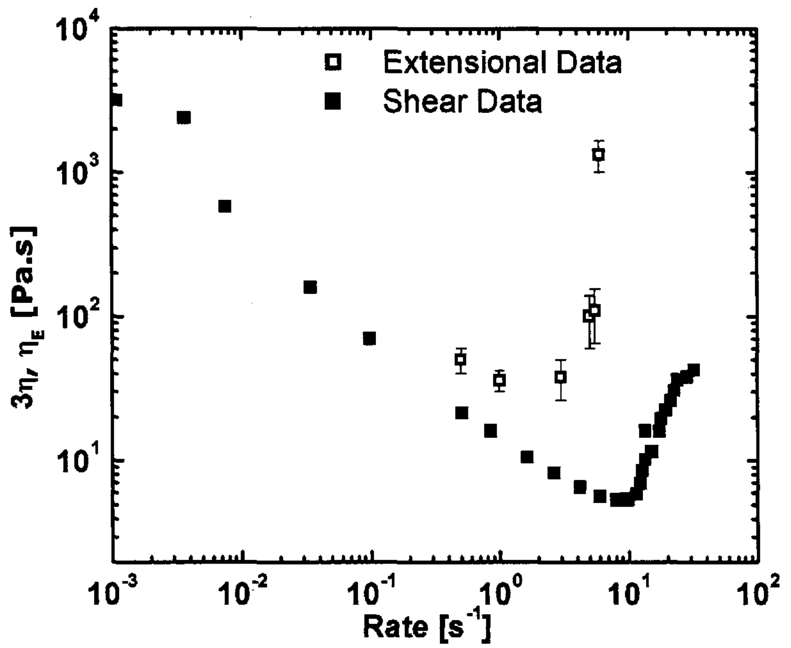

Figure 3.3.5: Comparison between nominal extensional viscosity and steady shear rheology for the monodisperse silica suspension at ϕ of 60%, shear rates have been divided by $\sqrt{3}$ to account for the strain second invariant, T = 22 °C.

3.4. SLIP

The effect of wall slip, commonly encountered in suspensions, has also been considered in this study. The presence of this phenomenon was detected in both the monodisperse and polydisperse suspensions. In order to minimize or possibly eliminates its effect, different roughened surfaces have been used to carry out rheological experiments.

The magnitude of slip occurring at the fluid-solid interface was quantified by applying the classic analysis by Yoshimura & Prud'homme {Yoshimura, 1988 #4}, and therefore the best slip-reducing surface found for each of the fluids.

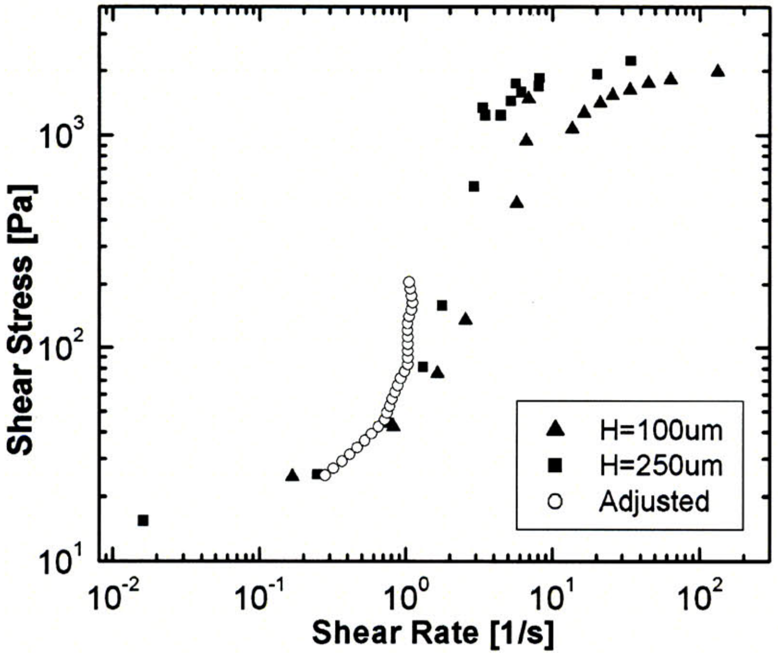

Figure 3.4.1: Steady shear rheology of the polydisperse suspension studied with a plate-plate geometry at T= 22 °C at different plate gaps. The data adjusted to account for slip according to the analysis by Yoshimura & Prud'homme is also reported.

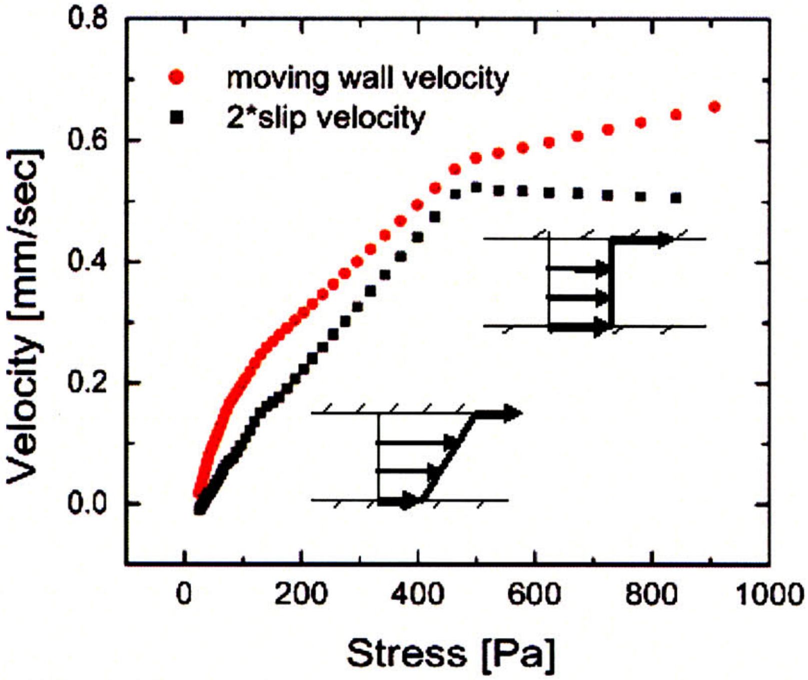

Figure 3.4.2: Wall slip velocity (calculated according to analysis by Yoshimura & Prud'homme) dependence on shear stress for a plate-plate geometry at T= 22 °C. The slip velocity increases until it reaches twice the moving wall velocity. (a) Velocity profile at r = R for stresses smaller than critical one. (b) Velocity profile at r = R for stresses greater than critical one.

As shown in Figure 3.4.1 the polydisperse suspension showed a significant amount of slip with all the surfaces studied. The one most efficient to reduce wall slip was obtained by gluing particles (same as used in the shear thickening fluid) to the surface. This was done by applying a thin coat of glue on the surface which was then covered with the particle; excess particles were shaken off and the surface was then UV cured. As expected, the slip velocity was found to vary linearly in shear stress until a critical value of stress was exceeded. After this critical stress the slip velocities showed no increase with stress: this behavior is shown in Figure 3.4.2. The velocity profile of the fluid at the outer radius can be sketched by looking at the speed of the moving wall as a function of stress. Below the critical stress the velocity profile is similar to the one sketched in Figure 3.4.2a, where the local shear rate in the fluid is reduced by the presence of wall slip. As the shear stress increases so does the slip velocity, which consequently reduces the 'real' shear rate. In fact according to the analysis by Yoshimura & Prud'homme the shear rate at the sample edges r = R is calculated as follows:

$$\dot{\gamma}_R = \frac{H_1\dot{\gamma}_{aR_1} - H_2\dot{\gamma}_{aR_2}}{H_1 - H_2} \tag{3.9}$$

where H_1 and H_2 are the two plates gaps and $\dot{\gamma}_a$ is the apparent shear rate at the outer radius of the plate. The wall slip velocity at the outer radius if than found as:

$$u_R = \frac{\dot{\gamma}_{aR_1} - \dot{\gamma}_{aR_2}}{2\left(\frac{1}{H_1} - \frac{1}{H_2}\right)} \tag{3.10}$$

At the critical stress the slip velocity approaches twice the wall velocity and the velocity gradient in the fluid approaches zero (see Figure 3.4.2b). After this point the fluid sample effectively moves in a 'solid body rotation'. Physically what is observed is the thickening of the fluid due to the increasing stress until a change in structure occurs at the critical stress, and the fluid 'jams' into a solid state. The presence of a small lower viscosity layer closest to the walls allows the top and bottom plate to slide and slip even if the fluid in between is in a solid state.

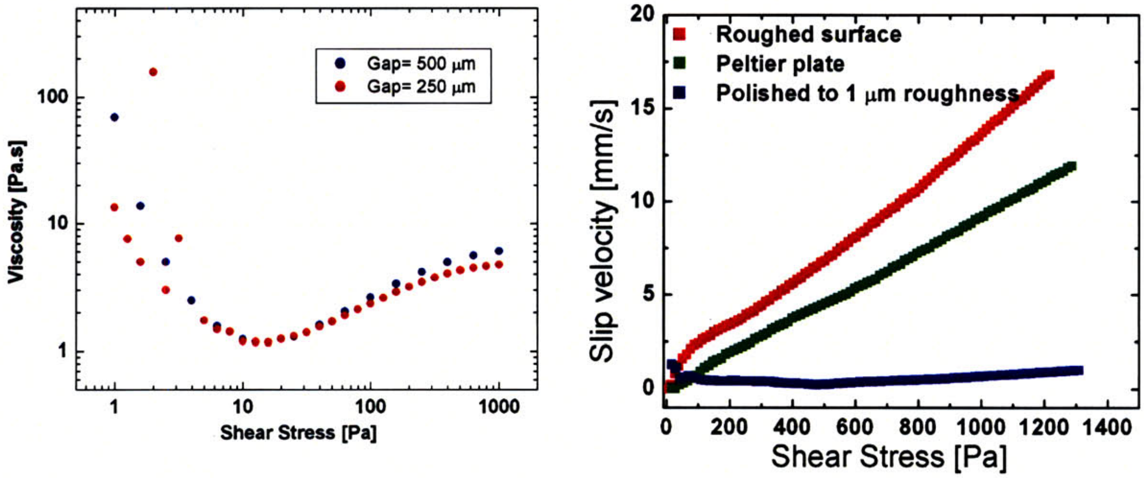

Figure 3.4.3 (a) Steady shear rheology of the monodisperse suspension studied with a plate-plate geometry (Peltier plate) at T= 22 °C at different plate gaps. (b) Wall slip velocities (calculated according to analysis by Yoshimura & Prud'homme) dependence on shear stress for a plate-plate geometry at T= 22 °C. The data for three different surfaces are shown.

A different behavior was observed for the monodisperse suspension; Figure 3.4.3(a) shows the steady shear rheology of the suspension at different plate gaps. The difference in the two results suggests that wall slip is present; Figure 3.4.3(b) illustrated the amount of wall slip at the outer radius of the sample for three different surfaces. As shown in Figure 3.4.3(b) a set of plates polished to a roughness of the order of microns was found to completely eliminate the presence of slip In fact, we found that in order to reduce or eliminate wall slip the roughness of the surface has to be very close to the size of the particles. A plot of the surface height for the 'roughen' surface is shown in Figure 3.4.4. The fact that this surface was not able to eliminate the wall slip for the polydispese suspension is probably due to the different shape and polydisperse nature of the suspension.

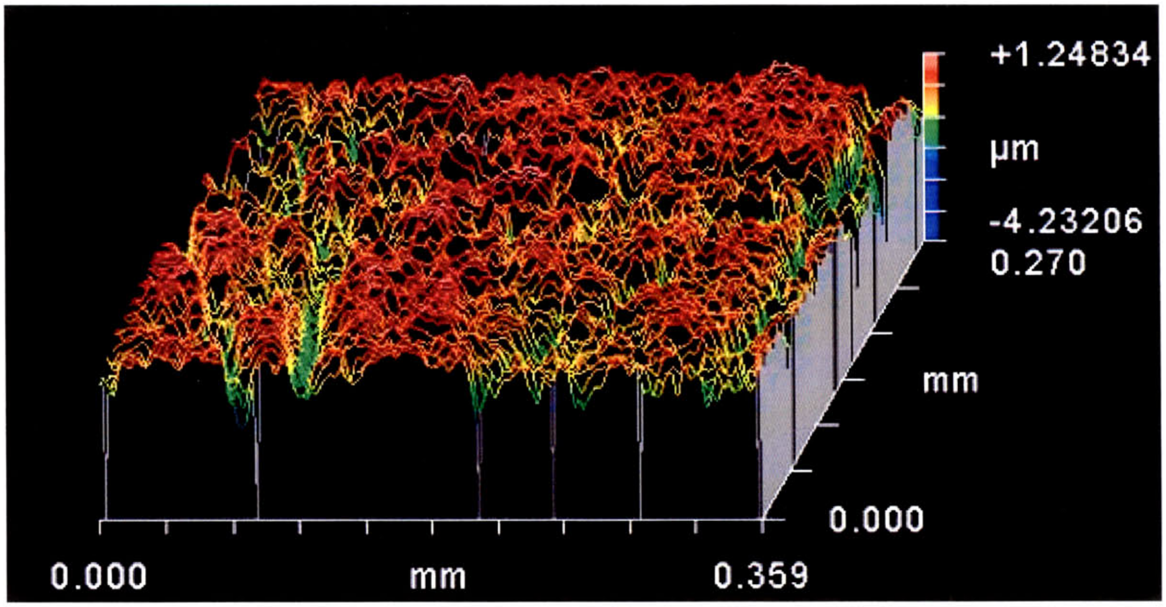

Figure 3.4.4: Plot of the surface height of the textured aluminum surface used in the rheological experiments to eliminate slip effect for the monodisperse suspension. Micrograph taken with a Zygo 3-D surface profiler.

4. Samples Characterization

4.1. Samples Specification and Preparation

The polyurethane foam used for composites was supplied by Crest Foam Industries (Moonachie, NJ) with the following product specifications: average cell size of 360 μm, density of 0.03 kg/m^3 and E_S= 70 MPa. Foam samples with pore sizes of 280 μm and 500 μm were also provided and utilized. Prior to testing, the samples were cut to size with a puncher to assure accurate dimensions and sample reproducibility. Two different sample sizes were used: for Texture Analyzer and Dynatup experiments the diameter measured 2.8 cm with a height of 2 cm, while for the split Hopkinson pressure bars a much smaller sample with diameter of 1.3 cm and height of 0.5 cm was used. The foam samples were impregnated with either glycerol or shear thickening fluid (monodisperse silica suspension at volume fraction ϕ = 60%) at different fluid fraction ψ, by suction forces. The volume fraction of fluid in the sample, ψ, was found by direct weighting prior and after impregnation. Figure 4.1.1 shows micrographs of the polyurethane foam and the same foam after being impregnated with a shear thickening fluid. As fluid is introduced into the foam it tends to collect around the cell walls, or trusses of the foam structure due to capillarity. As the amount of fluid is increased (by increasing the filling fraction ψ) the fluid starts to collect in between the pores, until the fluid fills the whole space. In order for the fluid to remain in place without draining, a small value of yield stress, τ_y, in the fluid is necessary. In fact we can estimate

$$\tau_y \geq \rho_{fluid} g l_{fluid} \tag{4.1}$$

where l_{fluid} is the max pore size. By plugging the values of yield stress and density for the monodisperse suspension we find that a pore size of about 1 mm is necessary in order for the fluid to remain in place.

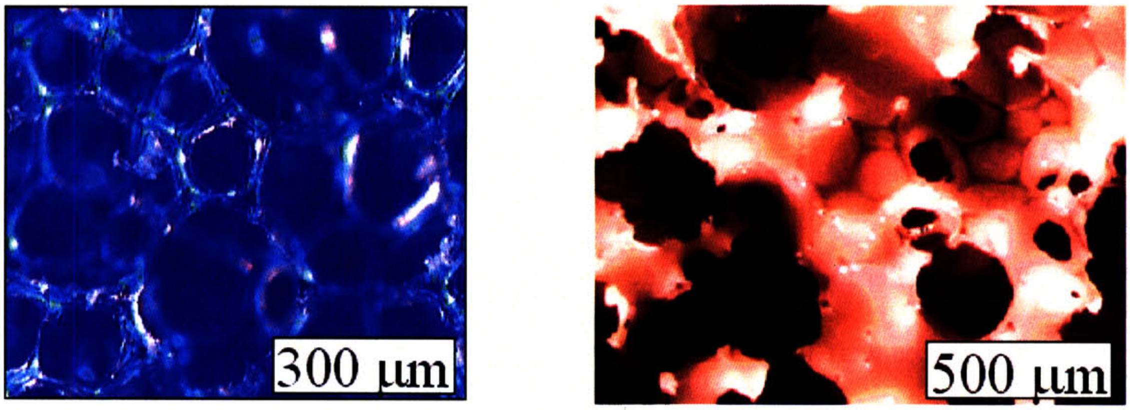

(a) (b)

Figure 4.1.1: (a) Micrograph of dry polyurethane open cell foam with an average cell size of 360 μm. (b) Polyurethane open cell foam impregnated with a monodisperse silica suspension at ϕ =60 %.

4.2. Quasi-Static Loading of Samples

4.2.1. Characterization of Unfilled Foam

The mechanical properties of unfilled dry polyurethane foam were characterized with the Texture Analyzer at constant strain rates that varied between 10^{-2}-1 s^{-1}. As expected the foam showed an initial linear elastic regime up to a strain of 10% followed by a long plateau characterized by a stress that varied between 3 to 6 kPa, depending on the strain rate. In fact, the stress-strain response of this viscoelastic polyurethane foam is weakly strain rate dependent as can be seen in Figure 4.2.1. After the long plateau region the foam densifies at a strain of about 80%.

The energy absorption characteristics of these foams were calculated by integration of the stress-strain curve. Optimization curves were then constructed according to the methods described in section 2.2.2.5 and are shown in Figure 4.2.2.

Foams with different cells size were also tested and, as expected, this feature did not affect the mechanical response of dry unfilled polyurethane foam.

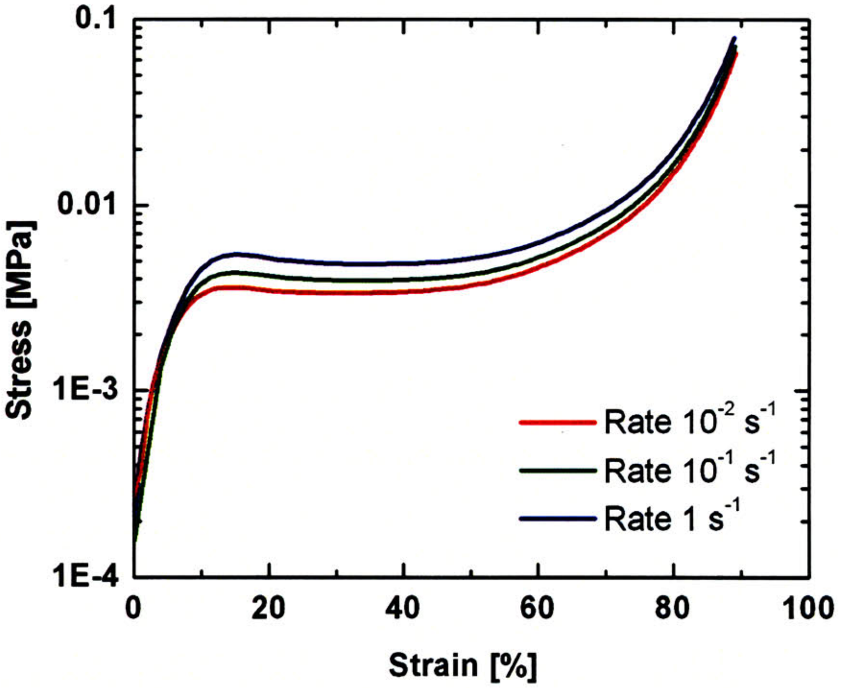

Figure 4.2.1: Stress-strain response of polyurethane foam with density of 0.03 kg/m^3 and $E_S = 70$MPa at strain rates that varied between $10^{-2} - 1$ s^{-1}.

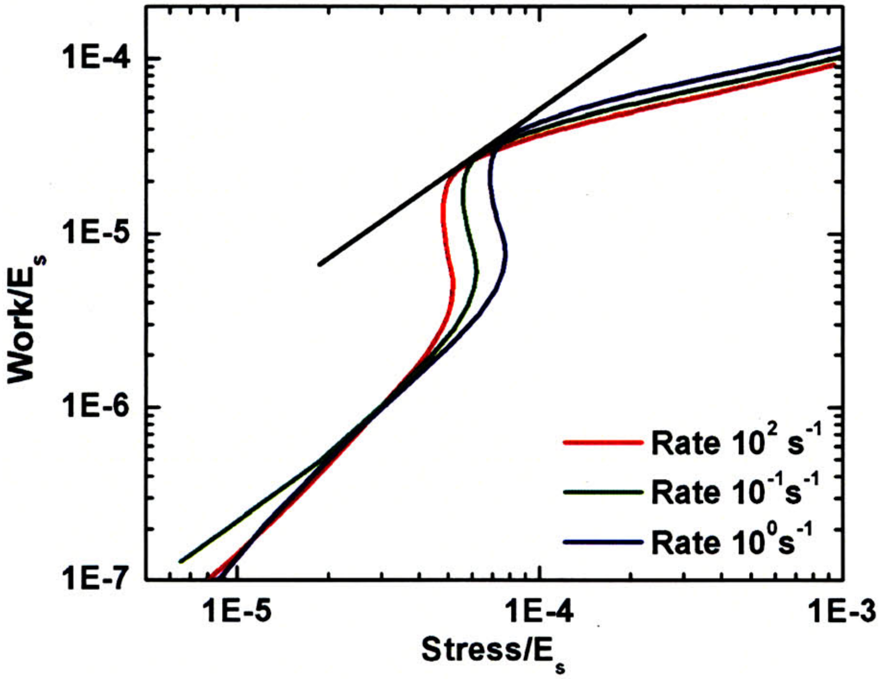

Figure 4.2.2: Optimization chart for polyurethane open cell foam with density 0.03 kg/m^3 and $E_S = 70$MPa. Black line represents the optimization line as described in section 2.2.2.5.

4.2.2. Characterization of Glycerol Filled Foam

4.2.2.1. Rate Dependence

As explained earlier in section 2.2.2.2, the material response of the foam samples is greatly affected by presence of a viscous fluid; in particular the stress response of foam acquires a strong strain rate sensitivity. This is illustrated in Figure 4.2.3 where the stress-strain response of glycerol filled foam is shown at different strain rates. Additionally, we note that the "stress plateau" not only depends on strain rates but also depends on strain and increases proportional to $1/(1-\varepsilon)$ as derived earlier in section 2.2.2.2 equation (2.25).

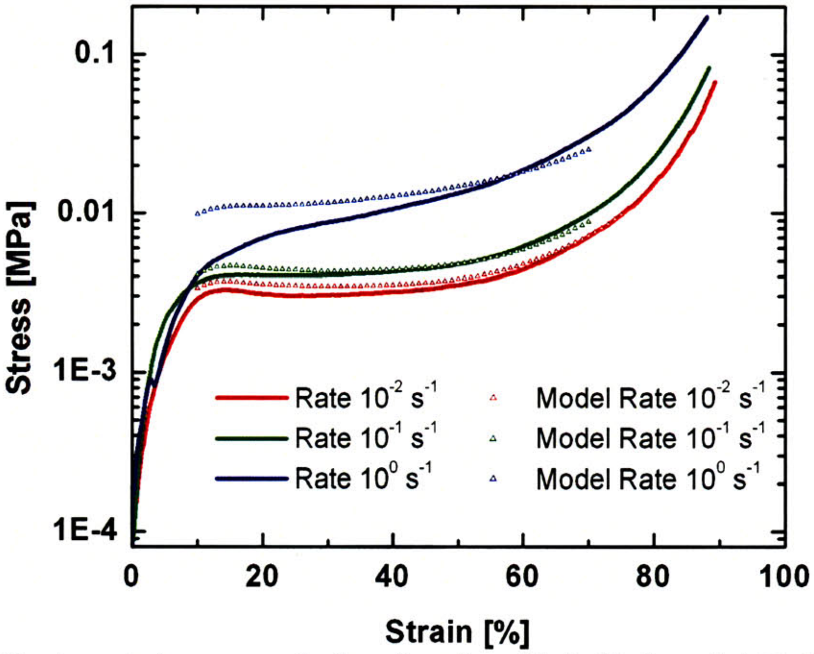

Figure 4.2.3:The stress-strain response of polyurethane foam filled with glycerol at ψ =100% for 3 different strain rates. (In symbols) Predictions of the scaling model as described in section 2.2.2.2. equation (2.26)

In fact, as the foam is compressed the fluid is pushed out of the pores, with the resultant stress being proportional to $\sim \eta \dot{\varepsilon}_{loc} \sim \eta V/l$ as for equation (2.24), where *V* is the velocity of foam compression and *l*, the cells size. As the strain ε increases, the size of the pore, and therefore the area through which the fluid flows decreases. This results in a much greater stress contribution. Also plotted in Figure 4.2.3 is the prediction from the scaling model presented in section 2.2.2.2, the model works well for 'low nominal strain rates', but fails to capture the behavior of the foam at strain rates greater than 1 s^{-1}. The strain dependence of the plateau stress is not very evident at low strain rates because the stress contribution from the fluid is small compared to the contribution from the solid matrix. This can be quantified by introducing a ratio Γ defined as:

$$\Gamma = \frac{\sigma_{fluid}}{\sigma_{foam}} = \left[\frac{C}{(1-\varepsilon)} \left(\frac{L}{l} \right)^2 \left(\frac{\mu \dot{\varepsilon}}{\sigma^*} \right) \right] \Psi \tag{4.2}$$

where σ_{fluid} is taken by equation (2.25), σ_{foam} is taken as the characteristic plateau stress σ^* and Ψ represents the volume fraction of fluid impregnated into the foam. The value of Γ at strain rates of 10^{-2},10^{-1} and 10^{0} are $\Gamma = 0.1$, 1 and 10 respectively; only when Γ becomes greater than unity do we start to observe substantial fluid contribution to the total stress. This is illustrated in Figure 4.2.4 where the response of glycerol filled foam is compared to the unfilled foam response for each strain rate. Looking carefully at Figure 4.2.4 one notices that, before the fluid contribution to stress became significant, the stress response of the empty foam is in fact greater than the response of the glycerol-filled one. This is not surprising if one realizes that the cell wall of the glycerol-filled foam are now "wet" with fluid which reduces the stiffness of the solid walls and therefore their stress response. As for the unfilled foam the energy absorption characteristics were calculated by integration of the stress-strain curve and optimization curves were constructed according to the methods described in section 2.2.2.5 and are shown in Figure 4.2.5. We note that the optimization curve is changed by the presence of the fluid and is no longer a single line but is better characterized as an area of optimization.

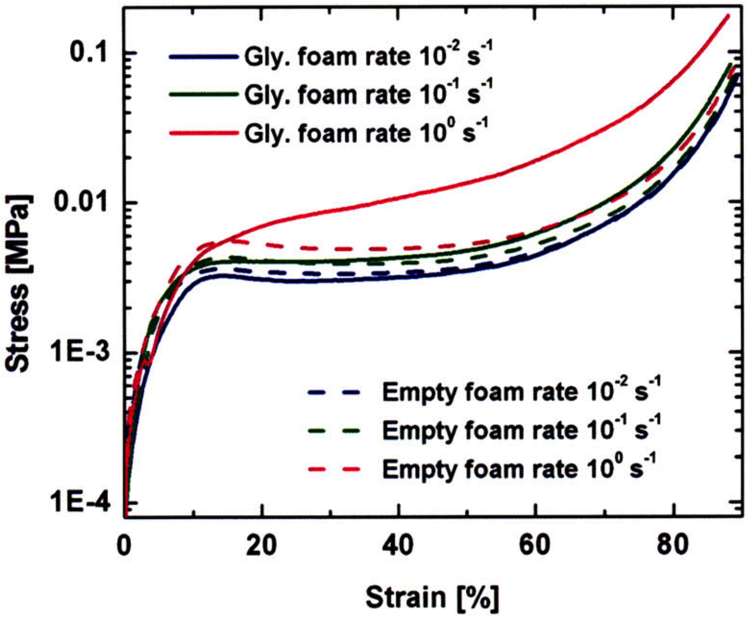

Figure 4.2.4: Comparison between unfilled foam and foam filled with glycerol at three different strain rates. (Solid lines) stress-strain response of polyurethane foam filled with glycerol at Ψ =100%. (Dashed lines) stress strain response of unfilled polyurethane foam.

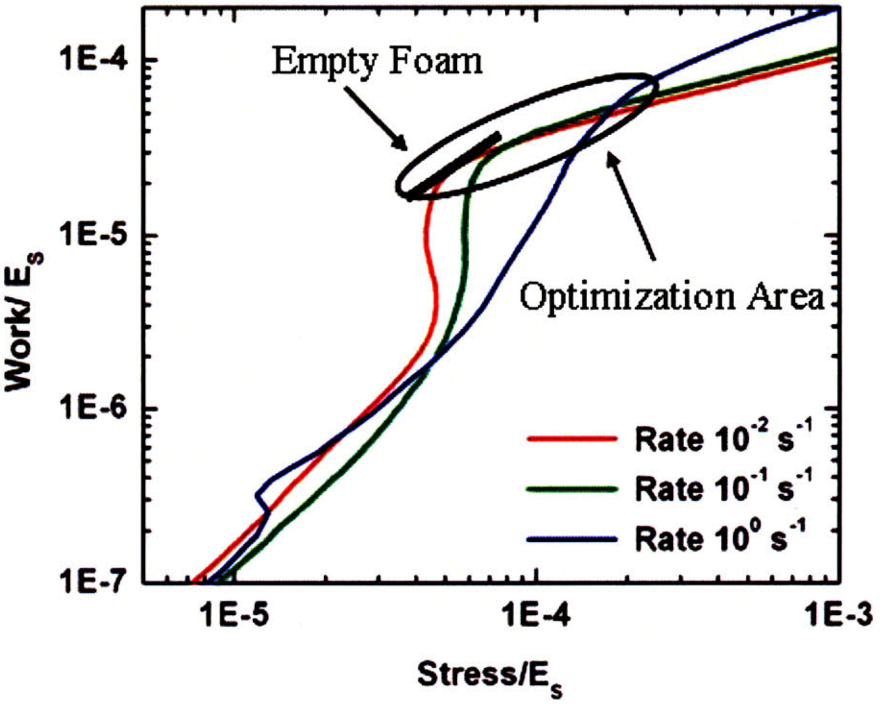

Figure 4.2.5: Optimization chart for polyurethane foam filled with glycerol at Ψ =100%

4.2.2.2. Volume Fraction Dependence

The stress response of fluid filled foams has been studied as a function of the fluid volume fraction Ψ. At relatively low strain rates, when the fluid contribution to stress is small and therefore the ratio Γ defined in equation (4.2) is much smaller than unity, we found no experimentally detectable difference between foams filled with glycerol at different volume fractions; Figure 4.2.6(a) illustrates this phenomenon. Even though no

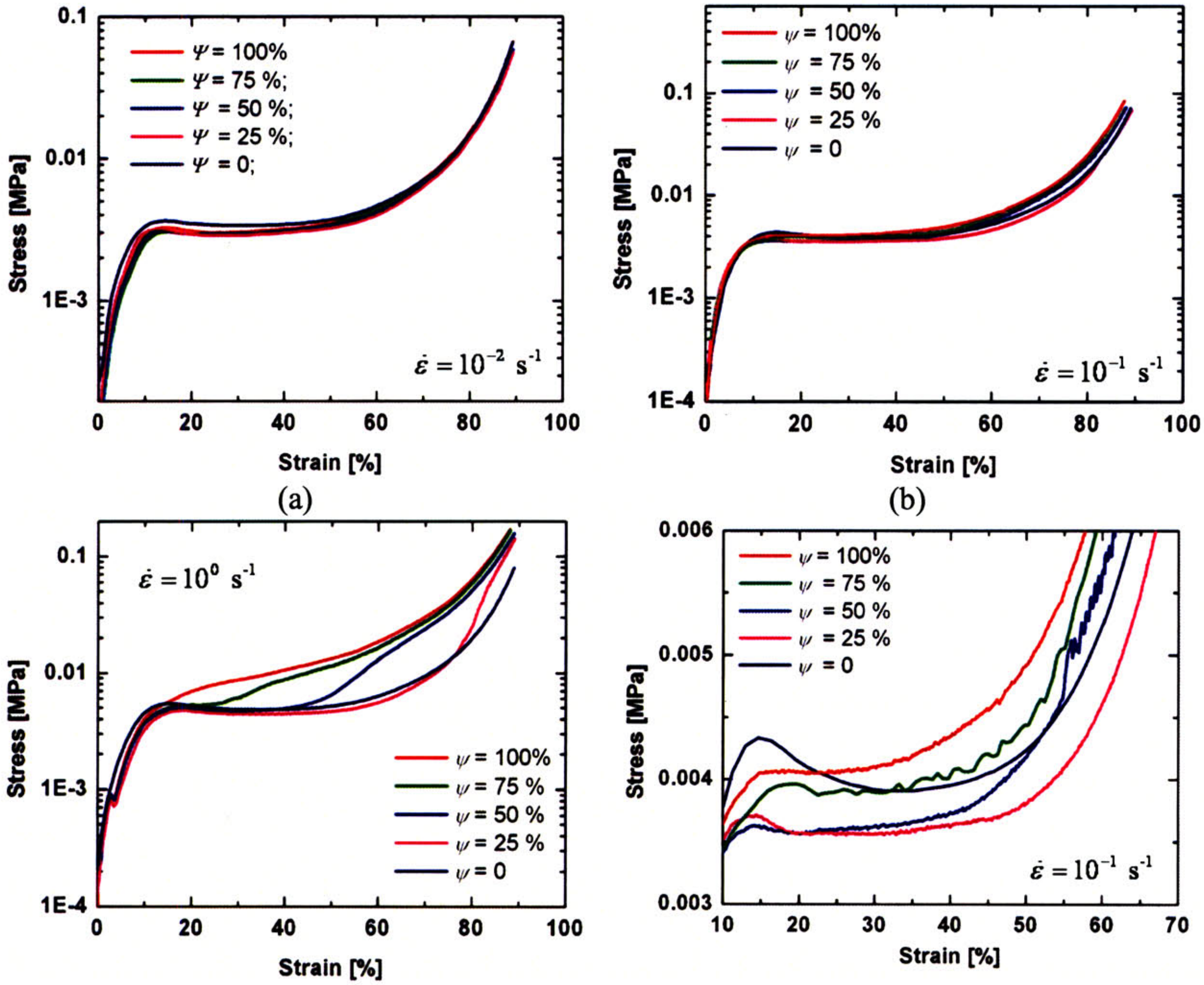

(a) (b)

(c) (d)

Figure 4.2.6: Compressive stress-strain response of polyurethane foams filled with glycerol. (a) Strain rate of $\dot{\varepsilon}=10^{-2}$ s^{-1}, fluid filling volume fraction vary between 100 to 0 %. (b) Strain rate of $\dot{\varepsilon}=10^{-1}$ s^{-1}, volume fraction vary between 100 to 0 %. (c) Strain rate of $\dot{\varepsilon}=1$ s^{-1}, volume fraction vary between 100 to 0 %. (d) close up (linear ordinate scale) of stress-strain curves at strain rate of $\dot{\varepsilon}=10^{-1}$ s^{-1}, volume fraction vary between 100 to 0 %.

observable difference between samples of different volume fraction was observed, the stress response of all the fluid-filled samples were found to be lower than the stress of the unfilled sample.

At strain rates of 10^{-1} s^{-1} one starts to observe a small volume fraction dependence in the measured stress as shown in Figure 4.2.6(b). In this case the unfilled foam stress response is higher than the 'wet' foam at low strains, but as the strain increases, so does the stress contribution from the fluid, as $\sigma_{fluid} \sim (1-\varepsilon)^{-1}$, and in the glycerol-filled foam the stress response becomes greater than the stress of the unfilled foam. The point at which the stress response of the unfilled foam and glycerol filled foam cross is a function of the volume fraction and the compression rate. This volume fraction dependence results from the fact that upon onset of axial compression it is first the unfilled fraction $(1-\Psi)$ of the sample that is collapsed before the fluid is forced to deform and therefore contributes to the stress response of the composite. As the strain rate is further increased this phenomenon becomes even more evident as illustrated in Figure 4.2.6(c).

4.2.3. Characterization of Shear Thickening Fluid Filled Foam

4.2.3.1. Rate dependence

Even at relatively low strain rates ($\dot{\varepsilon}=10^{-2}$ s^{-1}) the STF-filled foams behaves very differently than the glycerol-filled foam. In fact, the viscosity of shear thickening fluid depends on the 'local' strain rate and therefore is very sensitive to the local pore geometry. We can estimate the local strain rate as

$$\dot{\varepsilon}_{local} = C\frac{\dot{\varepsilon}}{d_i(1-\varepsilon)^{3/2}} \tag{4.3}$$

where C is a constant order 1 that depends on the foam cell geometry, d_i is the average cell size (360 μm for the foams used in these experiments), $\dot{\varepsilon}$ is the foam strain rate and ε is the 'macroscopic' strain. We can estimate the local strain rate by evaluating (4.3) with $d_i = 360$ μm and strains ε that vary between $\varepsilon = 0.1 - 0.8$ to find a local strain rates $\dot{\varepsilon}_{local} \approx 3 \times 10^3 \dot{\varepsilon} - 3 \times 10^4 \dot{\varepsilon}$. According to equation (4.3) a macroscopic strain rate of 10^{-2} s^{-1} will still impose a local strain rate of approximately $\dot{\varepsilon}_{local} \approx 30$ s^{-1} (at $\varepsilon = 0.1$) which is greater than the critical shear rate (see Figure 3.2.1) . The foams filled with shear thickening fluids were therefore always strained (even at low nominal rates) at rates greater than the critical deformation rate for onset of shear thickening..

This is consistent with the data shown in Figure 4.2.7, where the stress response of STF filled foams ($\Psi = 100$ %) is compared to the response of the glycerol filled foams (also filled to $\Psi = 100\%$). At this volume fraction the shear thickening fluid foam is always substantially stiffer than the glycerol filled one, and stresses can be up to 100 times greater.

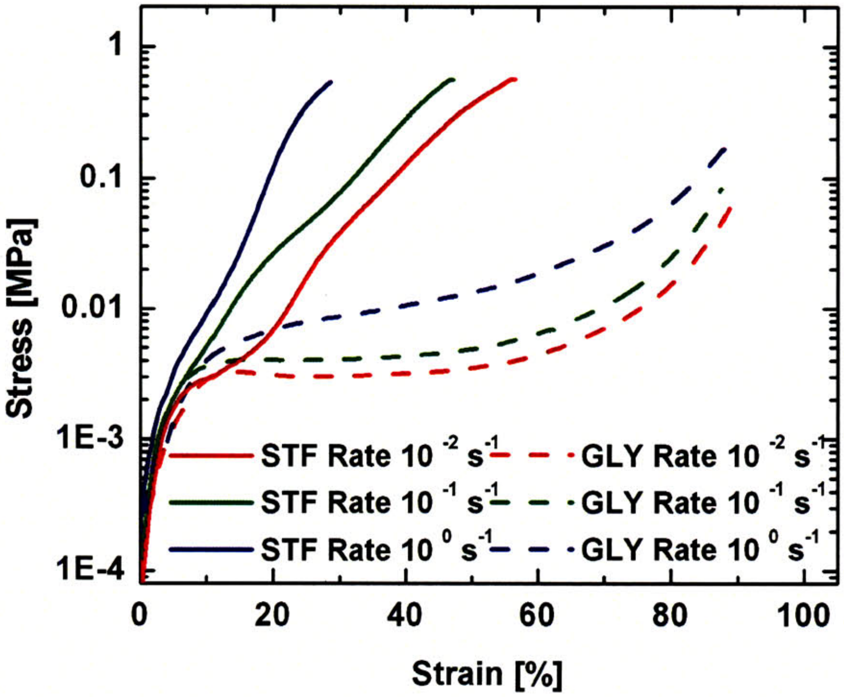

Figure 4.2.7: (solid lines) Stress-strain response of polyurethane foam filled with monodisperse shear thickening fluid (silica suspension) at $\phi = 60\%$ at strain rates that varied between 10^{-2} to 1 s^{-1}. (dashed lines) Corresponding stress-strain response of polyurethane foam filled with glycerol at strain rates that varied between 10^{-2} to 1 s^{-1}.

4.2.3.2. Volume Fraction Dependence

The compressive stress-strain response of the shear-thickening fluid based composite depends on the volume fraction of impregnation, Ψ ; and we also have investigated this variation. As may be expected, the higher the volume fraction of fluid inside the foam, the greater the magnitude of the stress response of the composite as illustrated in Figure 4.2.8. The shape of these stress-strain curves remains very similar, as it does not change with volume fraction. In fact, the curves superimposes until a strain of about 5-10 % is reached and then the stress grows proportionally to the volume fraction of STF in the sample. This is different than experimental measurement for the case of glycerol filled foam where the fluid contribution to stress started to grow at a strain of $(100\% - \Psi)$. In fact, the rate dependence of the STF based composites and therefore the greater stress response is seen at all strains greater than 5 % even if some air is present inside the sample pores (ie. $\Psi < 100\%$). This means that it is a lot harder for air trapped in the sample to escape when surrounded by the more viscous STF (especially during imposed straining) than when surrounded by glycerol where, as shown in section 4.2.2.2, air can easily escape.

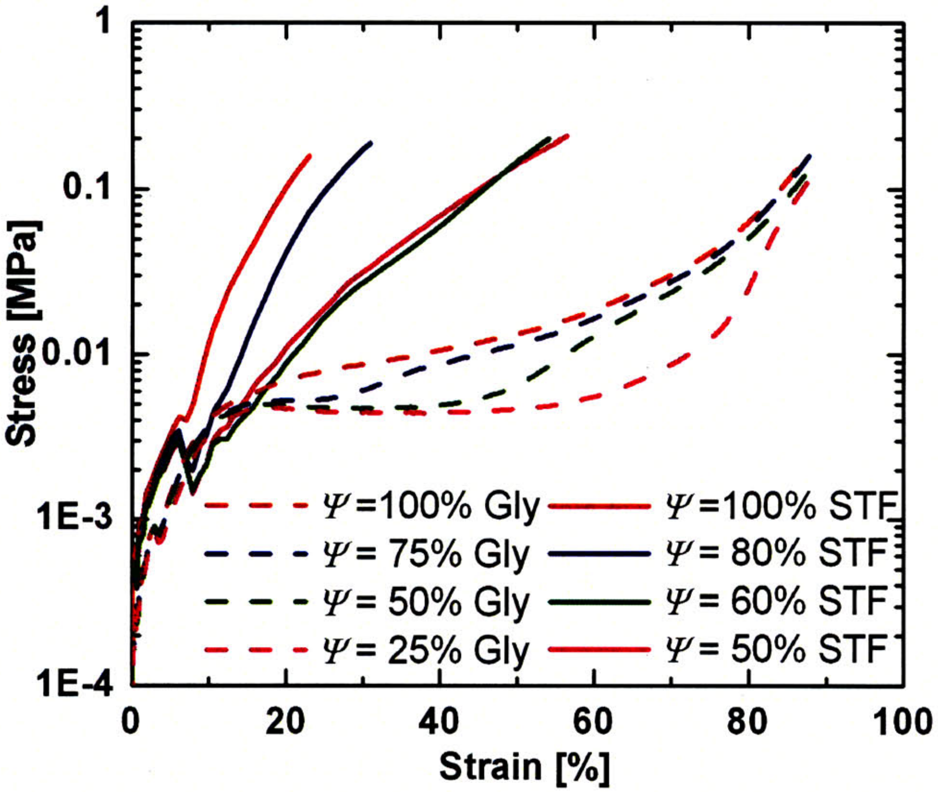

Figure 4.2.8: (dashed line) Stress-strain response of polyurethane foam filled with glycerol at different volume fraction Ψ. (solid lines) Stress-strain response of polyurethane foam filled with monodisperse silica suspension (ϕ=61%) at different volume fraction Ψ. Strain rate $\dot{\varepsilon} = 1$ s^{-1}.

5. Traumatic Brain Injury Protection

5.1. Introduction

Traumatic Brain Injuries (TBI) have very serious and debilitating consequences; as explained in section 2.4.2 these injuries are caused by the rapid acceleration or deceleration of the head that can result in coup and countercoup pressures and shear stresses in the brain inside the skull. The major goal in trying to design protective gear and helmets for these types of injuries is to decrease the magnitude of the acceleration that the brain is subjected to. Commonly, helmets or head gear consist of an outer shell designed to spread the load over a greater area, rather than a point load as frequently encountered from ballistic impacts, falling etc. The inside of the head gear is generally constructed from various types of absorbent material, primarily foams, which also make the helmet more comfortable to wear. The goal of a good material for this application is to absorb large amounts of energy at high rates of loading without exceeding a critical maximum load. Limited data is available on the human head tolerance to trauma, but a study by Hayda [53], found that the peak impact pressure for a 50 % probability of injury is around 50 MPa.

For this application we propose the use of shear-thickening fluid-filled foams. These fluid-solid composites have many potential advantages: they are flexible, and therefore provide comfort to the user during normal wear, while, as we will demonstrate later, they are also able to absorb large amounts of energy and maintain maximum stresses below critical levels.

5.2. High Rates Loading of Samples

In this study we examine the impact response of polyurethane foams filled with a non-Newtonian shear-thickening fluid and we compare the measurements with foams filled with a viscous Newtonian fluid: Glycerol. The variation on foam cell size and fluid rheology will also be examined. A drop tower apparatus, Dynatup HV9250 (described in section 2.2.3.2) and a high speed camera (Phantom V5) have been used to carry out the experiments. The Dynatup was modified to achieve unconstrained compression of the foam composites: the tup was replaced by a 3 cm diameter aluminum rod and a flat rigid aluminum plate was placed under the sample (see Figure 5.2.1).

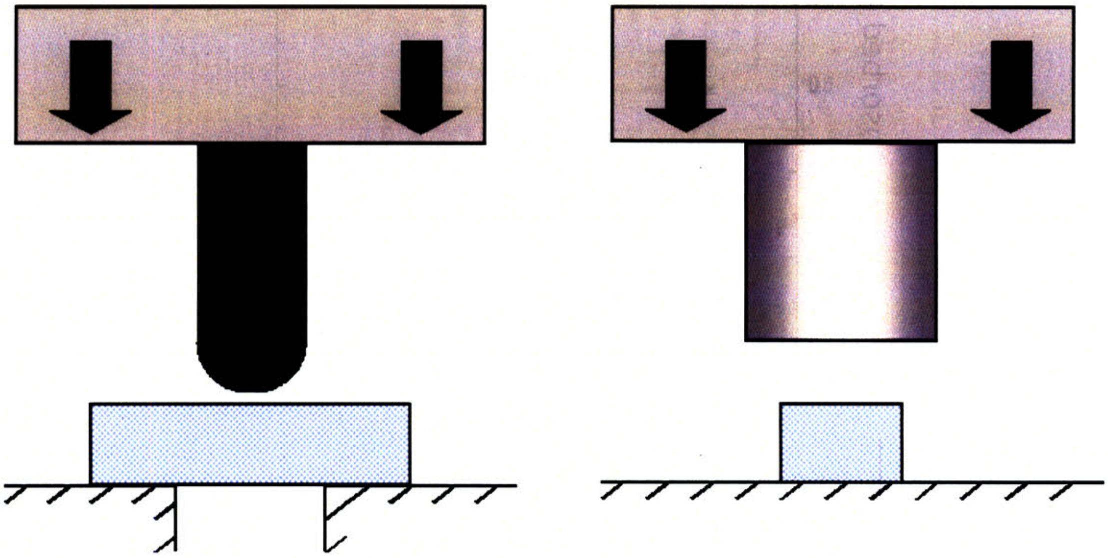

Figure 5.2.1 (left) original set up of Dynatup for sample penetration, tup diameter of 1 cm. (right) modified Dynatup set up for unconstrained compression experiments.

5.2.1. Glycerol Filled Samples

To create a baseline for reference, foam samples filled with glycerol were tested first. The impact energy, defined as $E = \frac{1}{2}mv^2$, where v the tup velocity at impactis can be scaled with the volume of the sample V, as

$$e = \frac{\frac{1}{2}mv^2}{V} \tag{5.1}$$

Even at relatively low e (energy per unit volume), the glycerol filled foam completely collapses (or 'bottoms out') and expels most of the fluid initially imbedded in the foam. At the lowest impact energies obtainable with this apparatus ($e = 1.3 \times 10^5$ J/m^3 for these specific samples) the glycerol samples were able to absorb up to 60% of the incoming energy, but as the impact energy was increased its performance (percentage of energy absorbed) dropped down to 25%; this is illustrated in Figure 5.2.2.

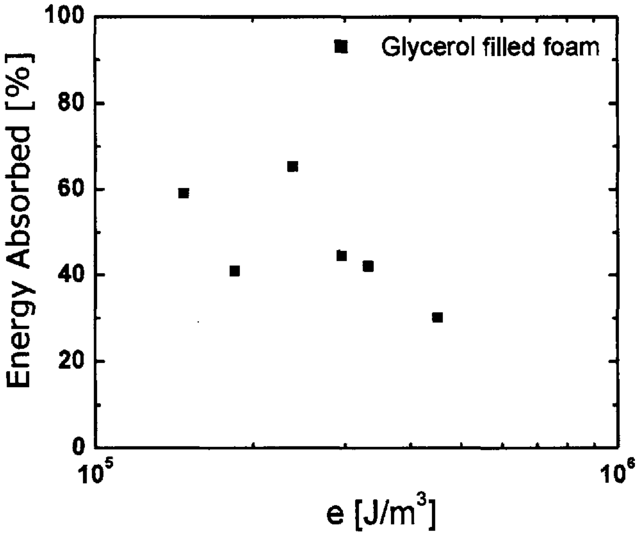

Figure 5.2.2: Percentage of energy absorbed for glycerol filled foam at =100% vs e, impact energy per unit Ψ volume. The sample absorbed a percentage of the incoming energy before bottoming out.

From each impact, the load vs. time data was collected and a representative set of curves are shown in Figure 5.2.3(a). The samples show a rapid increase in stress as the sample compresses and this becomes increasingly rapid as the impact energy is increased. The truncation of the data corresponds to the sample reaching the maximum strain allowable from the apparatus and therefore the collapsing of the sample. The load vs. time data can be used to derive a 'nominal' stress-strain curve (nominal because not a material function since deformation rates were not constant during experiments). This curve can be compared with the true stress-strain curves at low strain rates as shown in Figure 5.2.3(b). A sequence of high-speed video images of the impact were also collected and a series of them is shown in Figure 5.2.4 for a high energy impact.

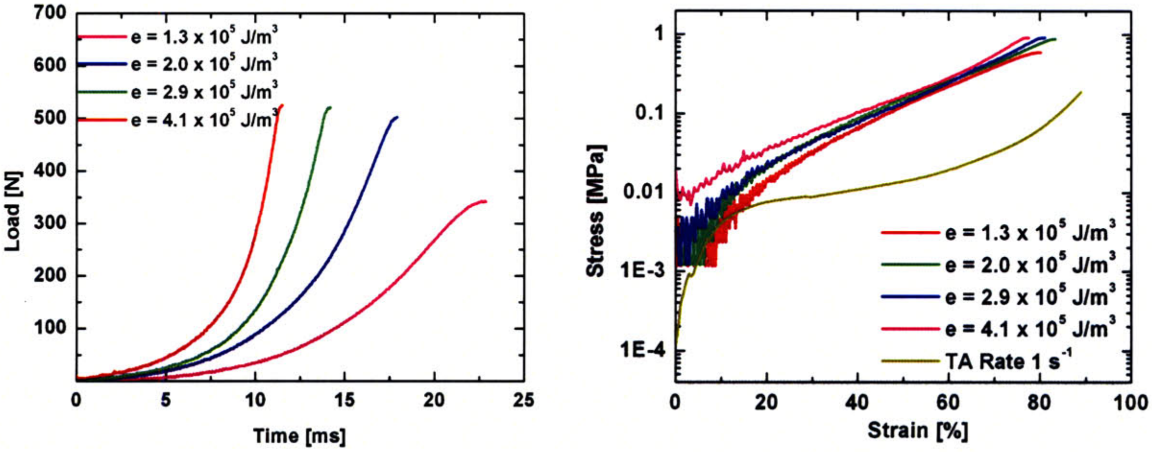

(a) (b)

Figure 5.2.3: (a) Load versus time data for e (impact energies /volume) that vary between 1.3×10^{-5} - 4.1×10^{-5} J/m^3 for glycerol sample filled to Ψ=100 %. (b) Calculated nominal stress versus strain for glycerol samples filled to Ψ=100 %. The initial strain rate defined as $\dot{\varepsilon}_0 = V_i / H$ (impact velocity Vi divide by sample height H) varied between 40 s^{-1} and 70 s^{-1}. True stress-strain experiment from low rate Texture Analyzer, $\dot{\varepsilon} = 1$ s^{-1}, is also plotted for comparison, see section 4.2.3.

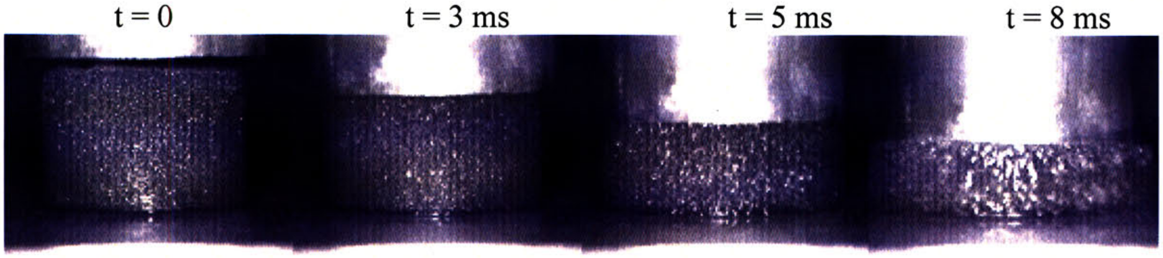

Figure 5.2.4: High-speed video images of impact for a glycerol filled foam at Ψ =100%, $e = 4.1 \times 10^5$ J/m^3, 55% energy absorbed.

5.2.2. Sample Filled with Shear Thickening Fluid

Drop tower experiments were also carried out with foam samples filled with the silica based suspension described in section 3.1. These experiments show that the fluid-solid composites are able to absorb most of the impact energy (up to 90 %) and return the rest in the rebound of the falling tup. A typical response at relatively low *e* (impact energy per unit volume) is shown in Figure 5.2.5 with the corresponding video images. One specific feature of this experiment is that the peak in the stress does not correspond to the point of max strain in the foam and therefore the point at which the impact velocity is zero. This is a consequence of the highly non-linear viscoelastic response of this foam/fluid composite system.

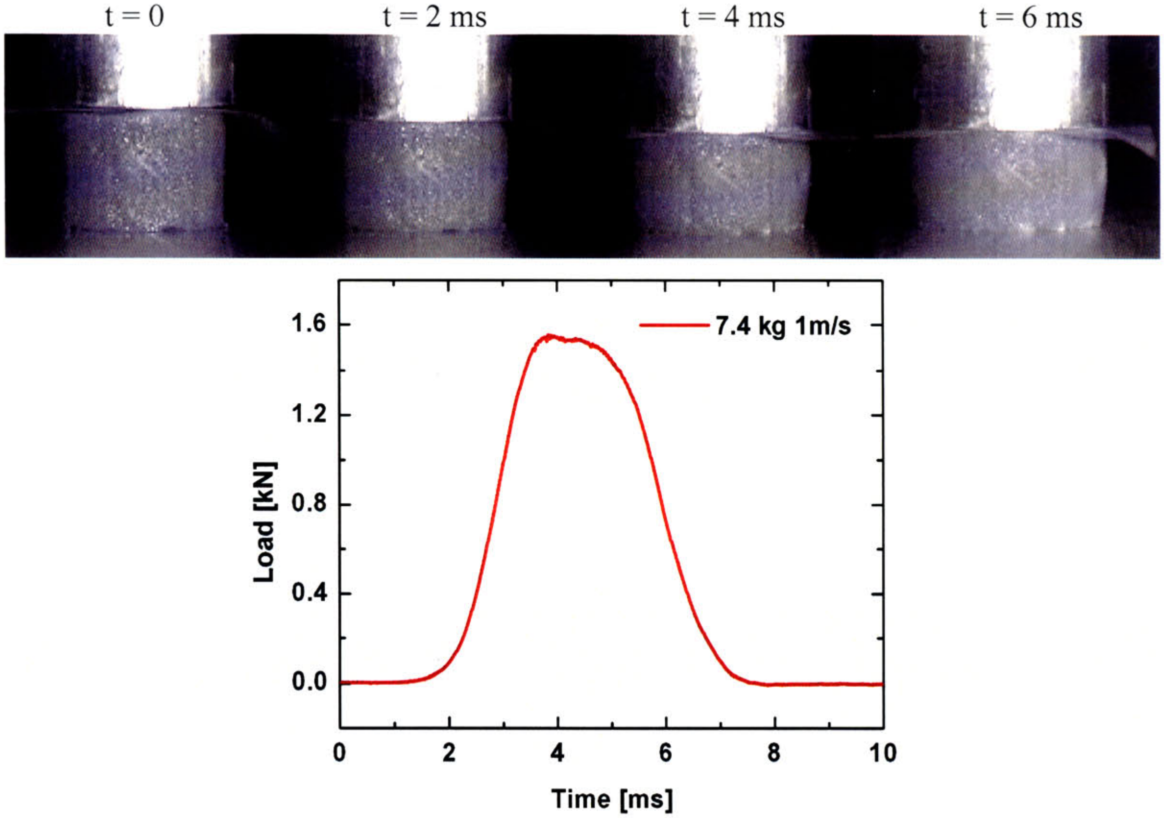

Figure 5.2.5: (top) High-speed video images of impact for Silica based STF filled foam, $e = 1.3\text{x}10^5$ J/m^3 , 89% energy absorbed. (bottom) Load vs time data for the same experiment.

As the impact energy density increases the composite response varied, the peak stress increased and the duration of the impact decreased; this is illustrated in Figure

5.2.6. In these experiments the material was able to absorb about 90 % of the incoming energy, while the remaining 10% was returned in the rebound.

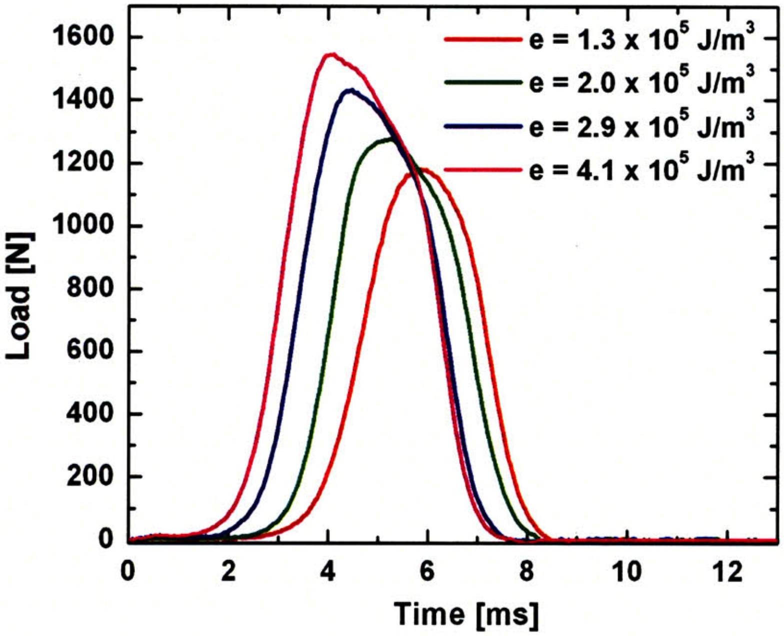

Figure 5.2.6: Impact data for Silica based STF filled foams filled to Ψ = 100%, *e* varied between 1.3 $\times 10^5$- 4.1 $\times 10^5$ J/m^3, 89 % energy absorbed.

As we increased the impact energies even further ($e > 6 \times 10^5$ J/m^3) we note a transition in the material response of the system. As the impact energy is further increased the peak stress reaches a maximum and then plateaus (see Figure 5.2.7), which suggests that a different mechanism for energy absorption comes into play. A clue regarding the mechanism for energy absorption comes from the high-speed video images of the samples during impact. As can be seen in Figure 5.2.8 after an initial deformation the fluid in the sample thickens and undergoes a transition from liquid to solid. If the impact energy is great enough ($e > 6 \times 10^5$ J/m^3) the sample fractures and deforms in a viscoplastic fashion. During the fracture and the propagation of the cracks the magnitude of the stress remains constant. This is further illustrated in Figure 5.2.9 where the instantaneous stress has been plotted against strain for varying values of *e*. For each experiment the stress reached a maximum value of 2.8 MPa after which it plateaus; the temporal duration of this plateau (ie the total amount of strain accumulated) depends on the impact energy. The deformations seen during impact in this regime were plastic in nature and very little recoil was observed. Thanks to this dissipative mechanism the samples were able to retain a relatively constant energy absorption percentage (energy absorbed over impact energy) around 80-90%, as shown in Figure 5.2.10, and the remaining energy was returned in rebound. This behavior is in contrast with the observations in a glycerol-filled composite. In this latter case the viscous dissipation of the fluid flowing through the foam pores constitutes the primary energy absorption mechanism.

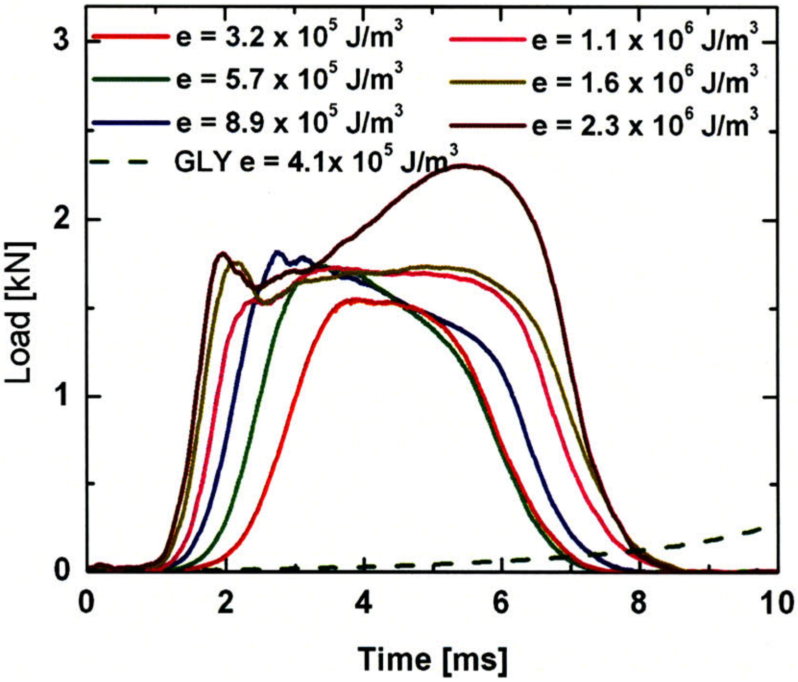

Figure 5.2.7: Impact data for Silica based STF filled foams, *e* varied between $3.2 \times 10^5 - 2.3 \times 10^6$ J/m^3. The corresponding data from the impact of glycerol filled foam is also shown for comparison.

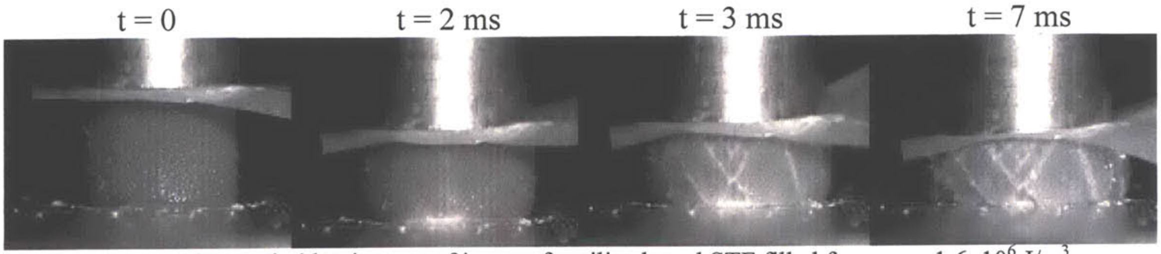

Figure 5.2.8: High-speed video images of impact for silica based STF filled foam, $e = 1.6\text{x}10^6$ J/m^3.

The key observation in this shear-thickening material is the ability to absorb large amount of energy (order of 10^6 J/m^3) at a relative constant plateau stress which is not affected by the magnitude of the incoming impact energy. Instead variations in the incoming energy density affect the magnitude of the viscoplastic deformation. This is an extremely important result because it suggests that this material can be used for energy absorption applications that also required flexibility or stiffness control. This composite is therefore an ideal candidate for TBI protection applications as it is able to reduce acceleration of the object of interest (by absorbing energy) and yet still be flexible and comfortable enough to be incorporated inside a composite helmet system.

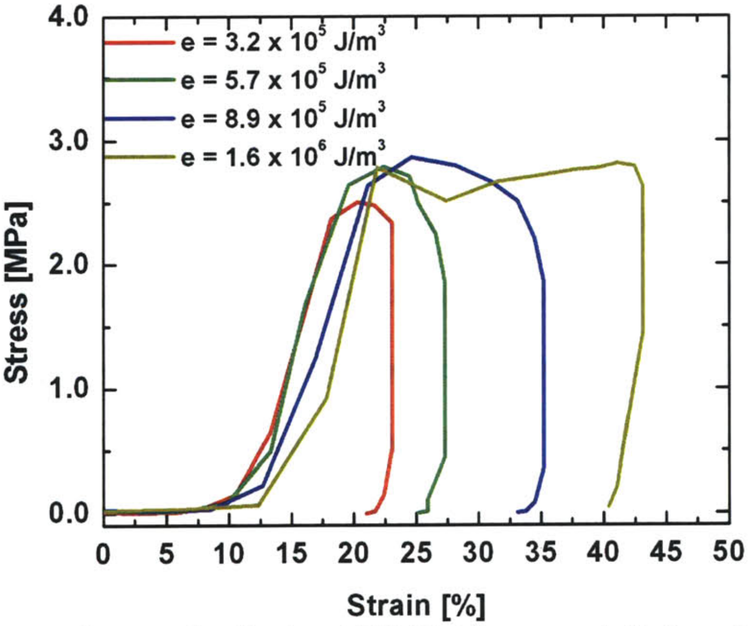

Figure 5.2.9: Stress-strain curves for silica based STF filled foams, e varied between $3.2\text{x}10^5 - 1.6\ \text{x}10^6$ J/m^3. The magnitude of the stress reaches a maximum of 2.8 MPa and then plateaus. Little sample recoil is observed.

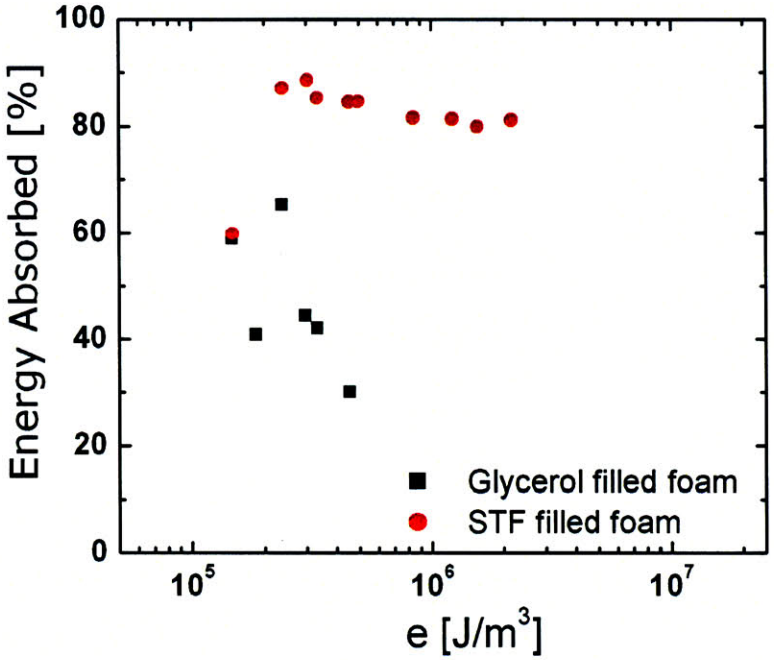

Figure 5.2.10: Percentage of energy absorbed vs. impact energy for both foams filled with glycerol or silica based STF.

5.2.3. High Rate Testing: Split Hopkinson Pressure Bars

High strain rates experiments were carried out by using a Split Hopkinson Pressure bar apparatus. Details of the apparatus and data reduction have already been presented in section 2.2.3.3. Aluminum pressure bars with a diameter of 19.05 mm and modulus of 72GPa were used. All foam samples (unfilled, glycerol filled and STF-filled) were tested but only STF filled composites returned meaningful results. In fact as explained in section 2.2.3.3 the stress is proportional to the magnitude of the strain measured on the transmitted bar. When the impedance of the sample is much smaller than the impedance of the measuring bar, the magnitude of the transmitted strain is so small that it is in the same range as the experimental noise in the system; this makes it difficult to distinguish between the two.

The stress-strain response of a STF based composites with $\Psi = 100\%$ at a strain rate of 800 s^{-1} is shown in Figure 5.2.11. Only data with strain of 4% or greater is shown because only then has the sample reached equilibrium and is therefore in a condition of uniform deformation. Higher strain rate experiments were also carried out but in this case the sample never reached a state of equilibrium and therefore we were not able to extract any meaningful data.

The response of these composites at high strain rates are consistent with the apparent stress-strain behavior observed in the Dynatup drop tower experiments. In fact the stress is found to grow until a plateau is reached (at around 15% strain). The value of stress at this plateau is consistent with the one found by drop tower experiments of 2 to 3 MPa. Comparison between experiments carried out with the Dynatup apparatus and with the Split Hopkinson bars are shown in Figure 5.2.12. By integration of the stress strain curve for the SHB experiment we can estimate the energy per unit volume that the composite absorbs during compression to be 1.0×10^5 J/m^3, which is in the same order of magnitude that the energy recorded during Dynatup experiments.

Unfortunately because of the limitation of this technique in measuring material properties of soft material (as foams) it was not possible to test the specimen at strains higher than 18% and therefore to sample the behavior along the stress plateau region.

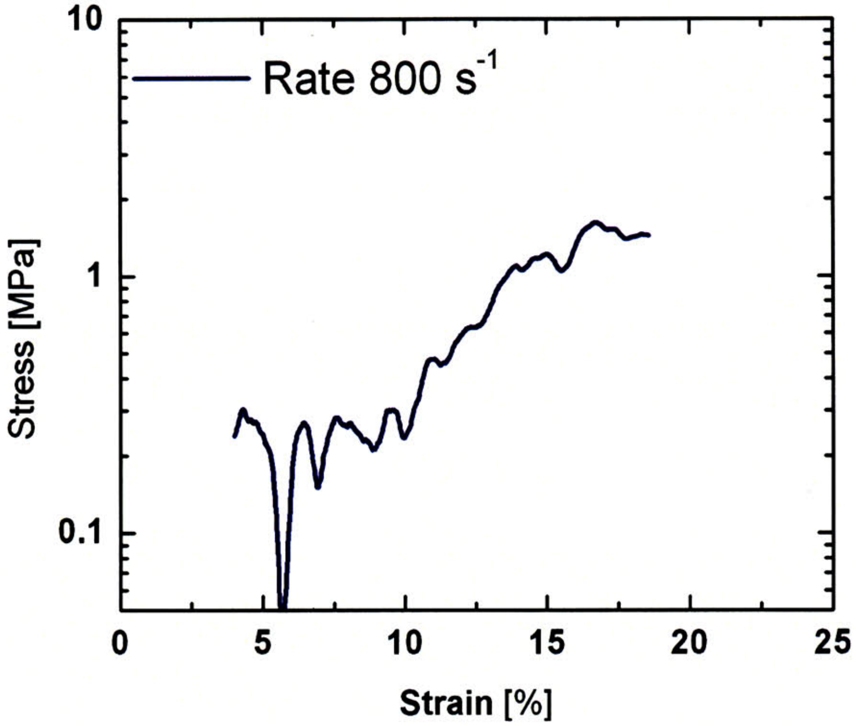

Figure 5.2.11: Stress-strain response of polyurethane foam filled with silica based STF under constant strain rate compression. Strain rate of 800 s^{-1}, $\Psi = 100\%$

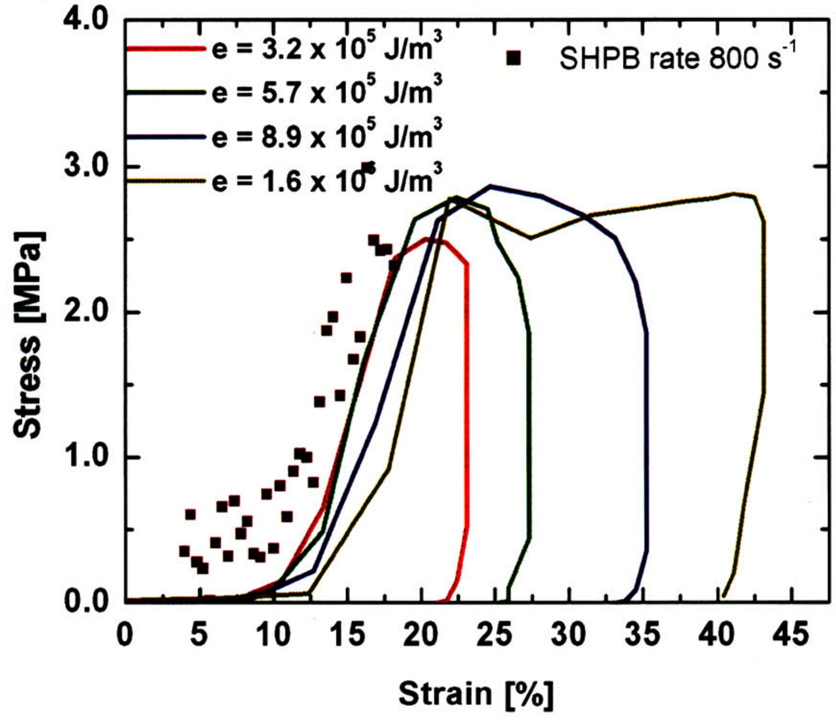

Figure 5.2.12: (solid lines) Stress-strain curves for silica based STF filled foams, *e* varied between 3.2x10^5 – 1.6 x10^6 J/m^3. (in symbols) Stress-strain curve measured using a Split Hopkinson Pressure bar system with the same sample at strain rate of 800 s^{-1}.

5.3. Dependence on Fluid Rheology

As presented in the section 5.2.2 the composite based on the silica shear-thickening fluid was able to absorb large amount of energy through a viscoplastic deformation mechanism. This mechanism, comprised of fluid thickening and solidification follow by cracking and the formation of shear banding, is due to the thickening properties of the silica suspension. The solidification and shear banding mechanism are an essential part of the energy absorbing capacity of the composite but cannot be easily related to the fluid rheology. In fact, there is still a need to understand which characteristic of the fluid rheology is necessary to obtain the desired response. Is the fact that the suspension shear thicken sufficient to obtain the desired composite behavior or does it have to reach a minimum level of viscosity. How does the jump in viscosity affect the composite behavior? To answer at least in part these questions the material response of the composite was studied as a function of the rheology of the shear-thickening fluid. A well known STF, a corn starch suspension, has been utilized for this purpose. Corn starch particle suspensions are probably the best known type of shear thickening fluids as it is easily obtainable. A common encountered problem with this suspension is aging but a systematic study on this matter has been conducted and steps have been taken to minimize this effect. In fact, the fluid was allowed to rest, after mixing, for a few hours. This allowed the particles to swell to an equilibrium state which resulted in a suspension with relatively constant (in time) rheological properties. Corn starch particles are polydisperse in size and not uniform in shape with a diameter of a few μm, an SEM image of dry starch particles is shown in Figure 5.3.1(a). The particles are negatively charged with a zeta potential of -9.51 mV.

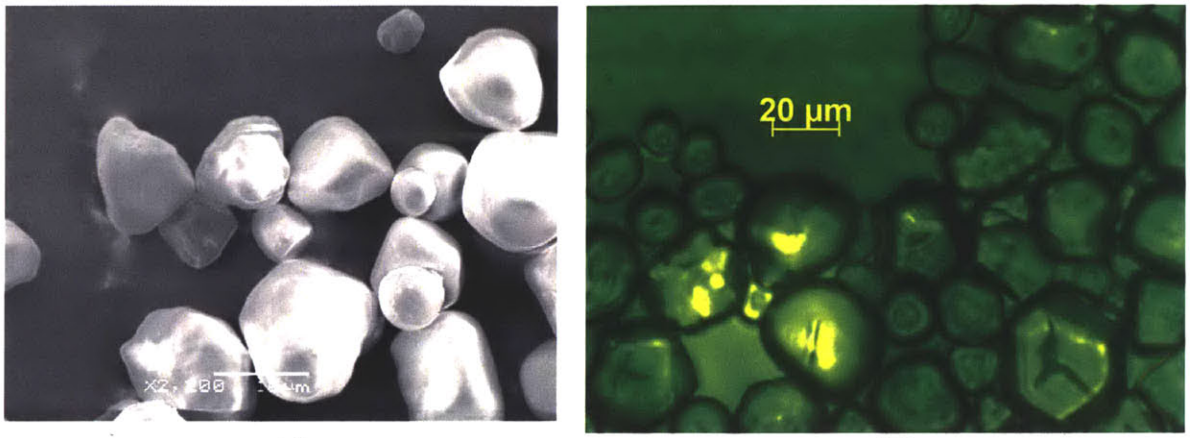

(a) (b)

Figure 5.3.1: (a) SEM image of dry corn starch particles, white bar correspond to 10 µm. (b) micrograph of corn starch in ethylene glycol.

To minimize evaporation problems and to keep the experiments consistent with the silica suspension, the particles were suspended in ethylene glycol. A weight fraction of 50% was found to give the desired shear thickening effect with minimal aging effects. In fact, when the suspension is mixed at higher volume fraction it tends to dry up much faster and turn into a paste. This is consistent with the idea that STF are in general more sensitive to variation of volume fractions at higher concentrations as was presented in section 2.1.3.1. Additionally, once in suspension, the particles swell and therefore increase in size, increasing the effective volume fraction even further; a micrograph of the swollen starch particles is shown in Figure 5.3.1(b).

After the suspension was allow to rest, to allow the particle to swell to equilibrium, the suspension rheology was measured by using an ARG2 rheometer and is shown in Figure 5.3.2. The rheological properties of this suspension were found to be very similar to the one of the silica suspension, shown in Figure 5.3.2, with the difference of a shift in the critical shear stress and rate; this reduction is not surprising as the corn starch particles are much greater than the silica particles.

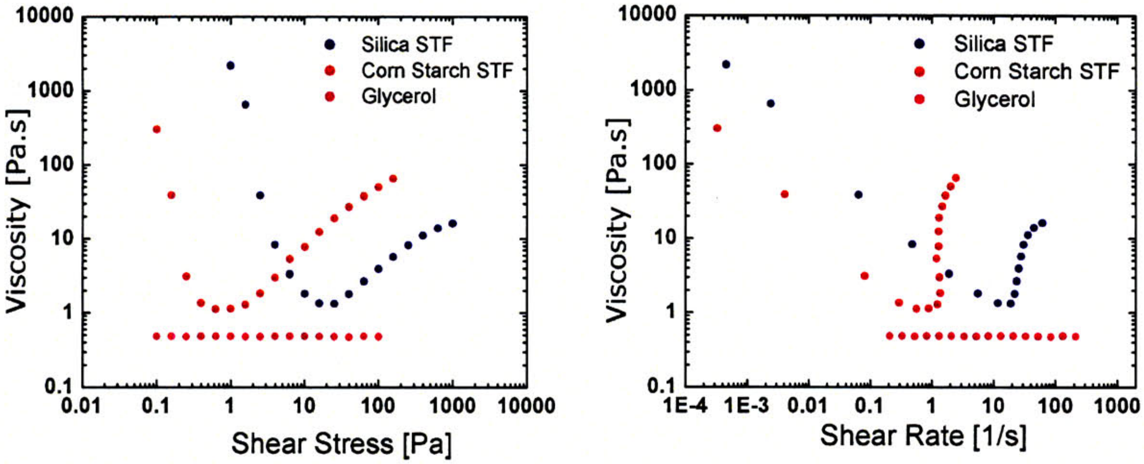

Figure 5.3.2: Steady shear rheology of corn starch in ethylene glycol at 50 % weight fraction, in blue also shown the rheology of a silica suspension at 60 % volume fraction which corresponds to 75 % weight fraction (solid %).

The polyurethane foam samples were impregnated with the starch suspension as described in section 4.1 and the dynamic properties of this composite were tested by using the drop tower apparatus. The result of load vs. time at four different kinetic energies is shown in Figure 5.3.3. At low *e* (energy per unit volume) the composite is able to absorb the impact energy without reaching the maximum strain ('bottoming out') but as *e* increases the composite collapses under the impact of the tup. This is shown by the truncation of the blue and purple data set in Figure 5.3.3, which indicates that the tup of the instrument has reached the minimal height and the experiments were terminated.

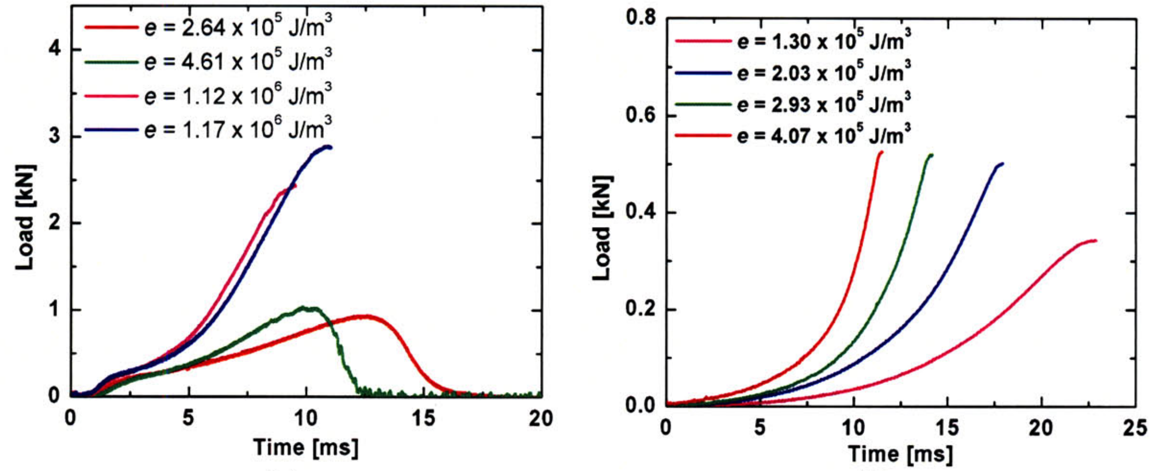

(a) (b)

Figure 5.3.3: (a) Load vs. time respond of polyurethane foam impregnated with a corn starch thickening suspension as a function of impact kinetic energy. The truncation of the data for higher impact energies indicates that the foam sample had reach a maximum strain ('bottom out') and the experiments was terminated. (b) Load vs. time respond of polyurethane foam impregnated with glycerol as a function of impact kinetic energy.

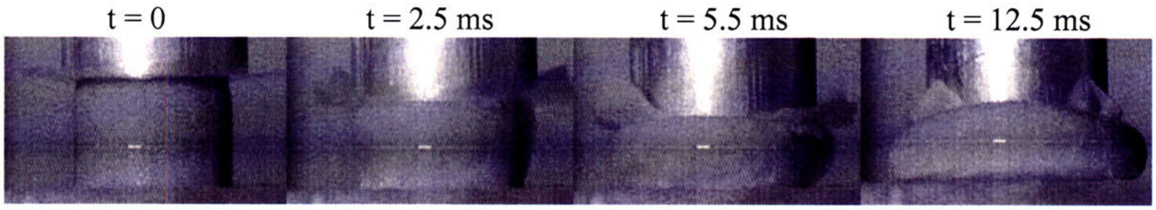

Figure 5.3.4: High-speed video images of impact for foam filled with 50 % weight fraction corn starch suspension in ethylene glycol at , e = 1.17x10^6 J/m^3.

More details of the composite behavior can be seen from the high speed video images in Figure 5.3.4. These images show the composite collapsing under impact and do not show any sign of extreme thickening (solidification) and shear banding (cracks) formation; this is in contrast with the behavior of the silica based composite as shown in Figure 5.2.8. The low *e* data set (green and red of Figure 5.3.3a) shows that the sample is able to sustain small impacts but with viscous dissipation the predominant mechanism for energy absorption. Despite the similar rheological properties of these fluids the material response of the composites are dramatically different. In fact, the response of the corn starch suspension is very similar to the glycerol filled foams response even though the loads experienced are an order of magnitude greater (see Figure 5.3.3b). The difference in behavior cannot simply be explained by the suspension rheological properties.

In fact the critical shear rates for the corn starch suspension is 1 s^{-1} which is much smaller than the local strain rate experienced by the fluid during impact. The local strain rates can be estimated as:

$$\dot{\varepsilon}_{loc} = \left\{ \frac{C}{(1-\varepsilon)^{3/2}} \frac{L}{l} \right\} \dot{\varepsilon}_{nom} \approx 10^{3} \dot{\varepsilon}_{nom} \tag{5.2}$$

where C is a geometric constant of order 1, ε is the strain, L represent the size of the sample and l the size of the foam pores. The local strains that the fluids experiences are around 10^3-10^4 s^{-1}, which are much greater than the shear rates probed by the rheological experiments and shown in Figure 5.3.2, this suggests that the two suspension have very different behavior at high shear rates. A further investigation of the suspension rheology at much greater shear rates would be necessary to explain the difference in behavior of the two composites. This result shows that not all shear-thickening fluids based composites will show viscoplastic deformation as reported in Figure 5.2.7 and Figure 5.2.8 and therefore ones needs to be careful when designing a composite of this type. In fact only a shear thickening fluid that solidifies at high strain rates is capable of creating a composite that behaves as discussed in section 5.2.2.

5.4. Dependence on Foam Pore Size

The microstructure of the foam, in particular its pore size has been studied as it may affect the response of the composite under loading. Three different pore sizes were compared: 280μm, 360μm and 500μm. All foams were impregnated with the silica suspension as described in section 4.1 and tested by using the drop tower apparatus.

Figure 5.4.1 shows the material response of the 500μm foam as a function of four impacts energies. As we can see from the impact data, the behavior of this composite is very similar to the 360 μm foam (shown in Figure 5.2.7) as it is comprised of a linear regime followed by a stress plateau. High speed video images of an impact (Figure 5.4.2) show that in the stress plateau region the fluid solidifies and starts to form cracks (shear banding occurs). This is the same mechanism seen for the 360 μm foam illustrated in Figure 5.2.8. Additionally, the magnitude of the critical stress or plateau stress is not statistically different than the one of foam of different pore sizes.

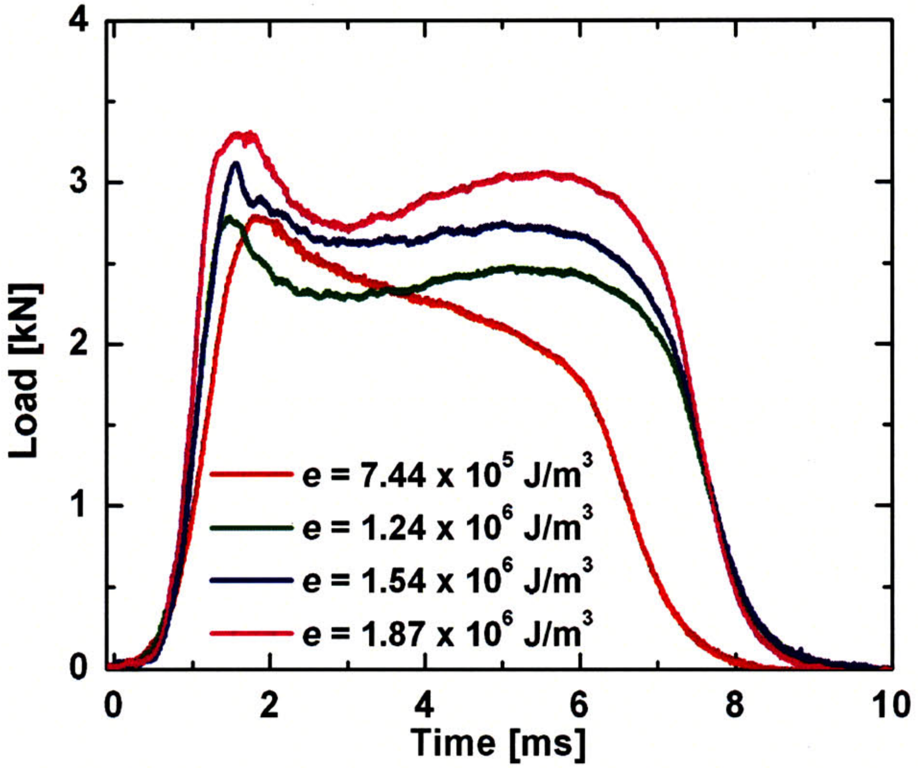

Figure 5.4.1: Impact data for 500 μm size foams filled silica based STF, *e* varied between 7.44x10^5 – 1.87x10^6 J/m^3.

Figure 5.4.2: High-speed video images of impact for 500μm pore size foam filled with silica based STF, *e* = 1.87×10^6 J/m^3.

Similar results were found for the composite based on 260 μm foam which are shown in Figure 5.4.3. These results suggest that the foam pore size does not affect the plateau stress. This is a surprising result as we would have expected the plateau stress to grow as the pore sizes are reduced. This suggests that once the fluid solidifies the STF is no longer sensitive to changes in strain rates and therefore is not very sensitive to the matrix geometry. Once the fluid solidifies the shear thickening fluid simply continues to yield as more energy is put into the system.

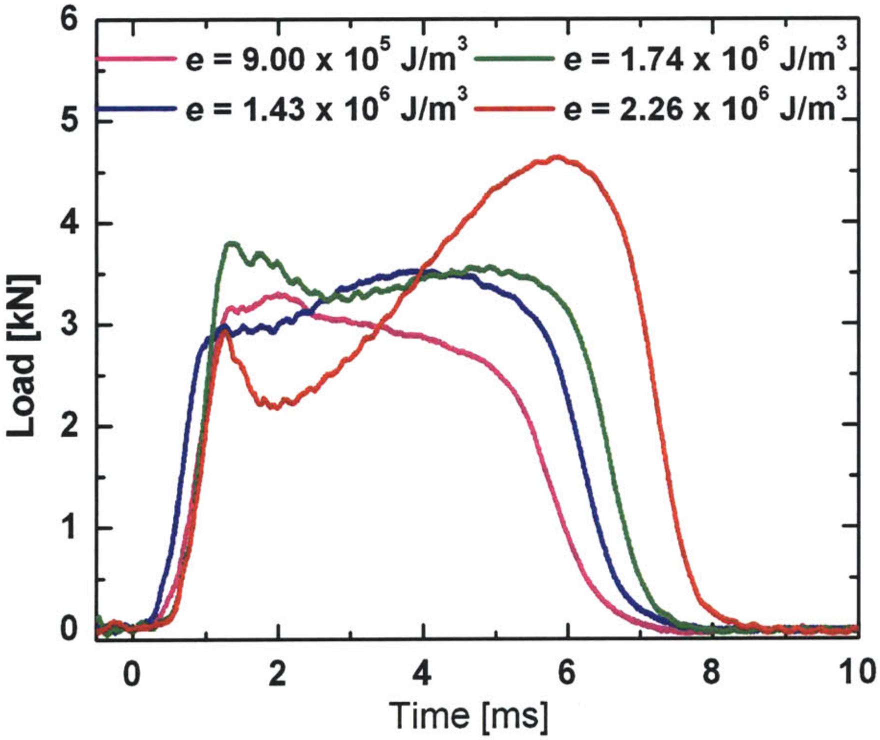

Figure 5.4.3: Impact data for 280 μm size foams filled silica based STF, *e* varied between 9.0×10^5 – 2.26×10^6 J/m^3.

5.5. Conclusions

The silica based STF composite has been found to be an excellent candidate for use in applications of TBI protection. In fact, through the mechanism of viscoplastic deformation, with solidification and shear banding, the composite was able to absorb large amount of energies (10^6 J/m^3) and still maintain stresses below critical levels. Additionally, as shown in Figure 5.2.10 the energy absorbing properties of the composite were found to be independent of the magnitude of the incoming kinetic energy.

The characteristics of these composites are due to the non-linear response of the silica based STF. Other fluids, as glycerol, have been used to fill the open cell foam but the resultant composite was not able to sustain the stresses imposed and collapsed under impacts. A shear thickening corn starch suspension was also used but the resultant composite did not give the desired response as it also collapsed under large impact energies without undergoing shear banding or cracking. From the design point of view this means that one needs to pay particular attention to the type of fluid used as not all STF, as shown, will produce the desired effect. The fluid rheology at high enough stain rates is necessary to assess the applicability of the specific STF.

Experiments have also shown that the composite has been found to be relative insensitive to the pore size of the solid matrix, at least in the range of energies tested. This fact simplifies the design process even though there are still limits on how small or large the pores of the foam can be. As the pores get smaller it becomes harder to efficiently impregnate the foams as the fluid deformation rates are inversely proportional to the pore size. On the other hand, if the foam pores are equal or greater than the capillary length the fluid will tend to drain out of the foam.

6. Blast Mitigation

6.1. Introduction

Primary Blast Injuries (PBI) occurs when a body is exposed to a blast wave and is due to the high pressure differential that is created across body tissue. As explained in section 2.3.3, these types of injuries are commonly found in gas-containing organs and are the result of the interaction between the blast wave and the chest cavity. Specifically, one of the wave characteristic, the rate of pressure rise, has been linked to primary blast injuries. Details on wave mitigation and the injury mechanism were discussed in section 2.3.

The goal in designing a blast mitigation material or composite is to reduce the rate of pressure rise of the wave transmitted to the body and therefore slow down the pressure pulse. Additionally there are other considerations, coverage and flexibility for example. As explained in section 2.3.4, thorax coverage is extremely important, especially in close environments where blast waves reflect back and forth on walls and enter the body from all directions. For this reason it is important to design a torso protecting gear that is flexible so that it can be wrapped around the body and follow the body shape for complete coverage. For this purpose we propose to use a silica based suspension impregnated in polyurethane foam as part of a layered composite.

6.2. Test apparatus: Shock Tube

A shock tube apparatus has been used to test the material response of unfilled foams, glycerol filled composite and silica based STF-filled composites. Details of the apparatus and the theory behind it were discussed in section 2.3.6.

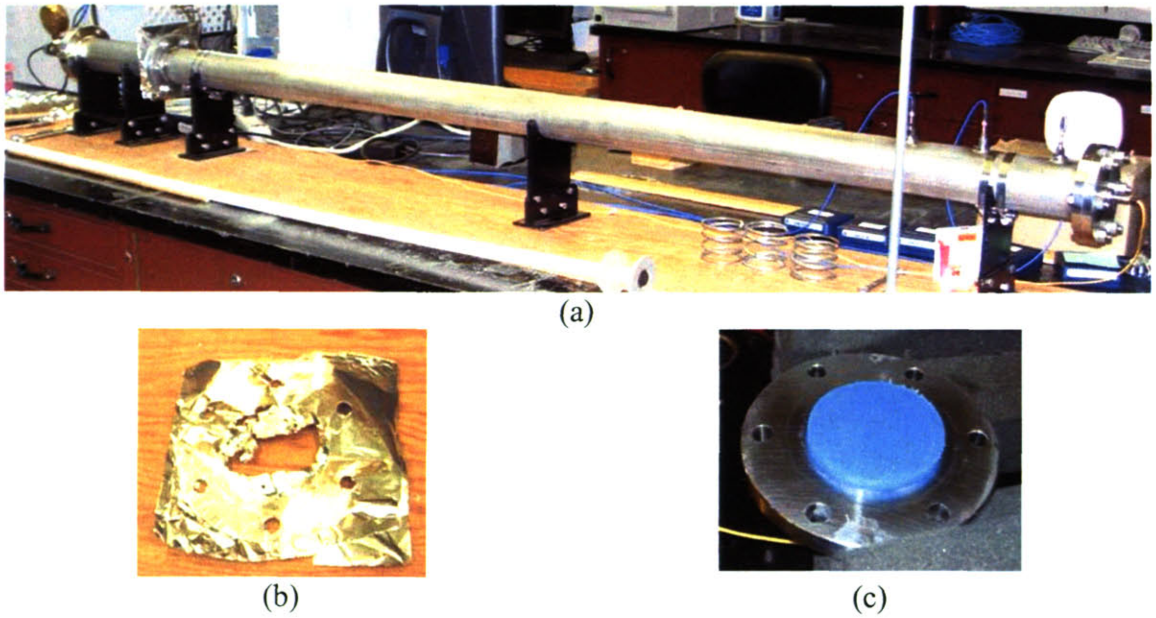
(a)

(b)

(c)

Figure 6.2.1: (a) Picture of shock tube apparatus used for the testing of the composite (b) picture of a burst diaphragm made from aluminum sheets. (c) endplate of the apparatus with STF based composite placed on top of the pressure sensor

The shock tube used for the experiments, used in collaboration with the Center for Soldier Survivability at Natick, had a diameter of 2.5" and was composed of a pressure chamber attached to a long tube. A picture of the set up is shown in Figure 6.2.1(a). A diaphragm made from Aluminum sheets separates the pressure chamber from the tube. A picture of a burst diaphragm is shown in Figure 6.2.1(b). Three sensors were placed along the tube to check the advancing wave while one sensor was placed at the end of the tube, on the endplate, to collect pressure measurements. The samples were placed on the endplate, as seen in Figure 6.2.1(c), and kept in place by a thin ring which was placed just inside the 2.5" tube.

A typical pressure pulse results from this apparatus is shown in Figure 6.2.2. The rise in the initial pressure pulse is shown with a small time delay since the triggering was activated by the first side sensor of the tube upon the passing of the wave. The successive spikes in the pressure pulse are due to the wave traveling back and fourth though the tube.

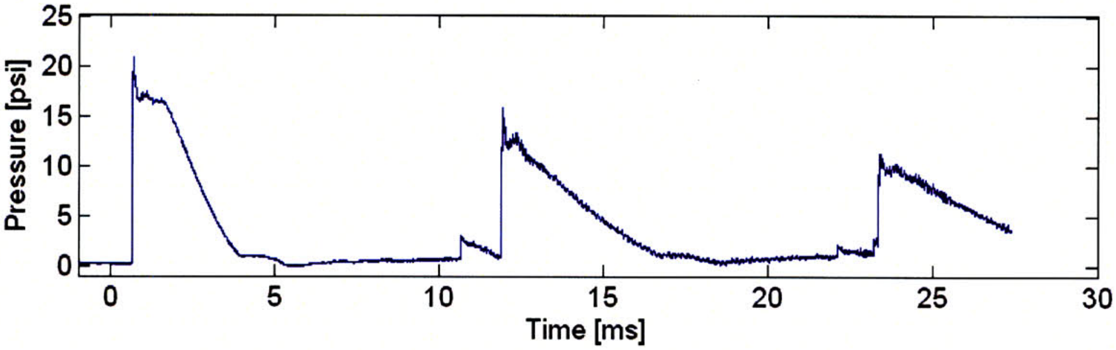

Figure 6.2.2: Pressure pulse as measured directly from the pressure sensor at the endplate for an unfilled foam of ¼" thickness.

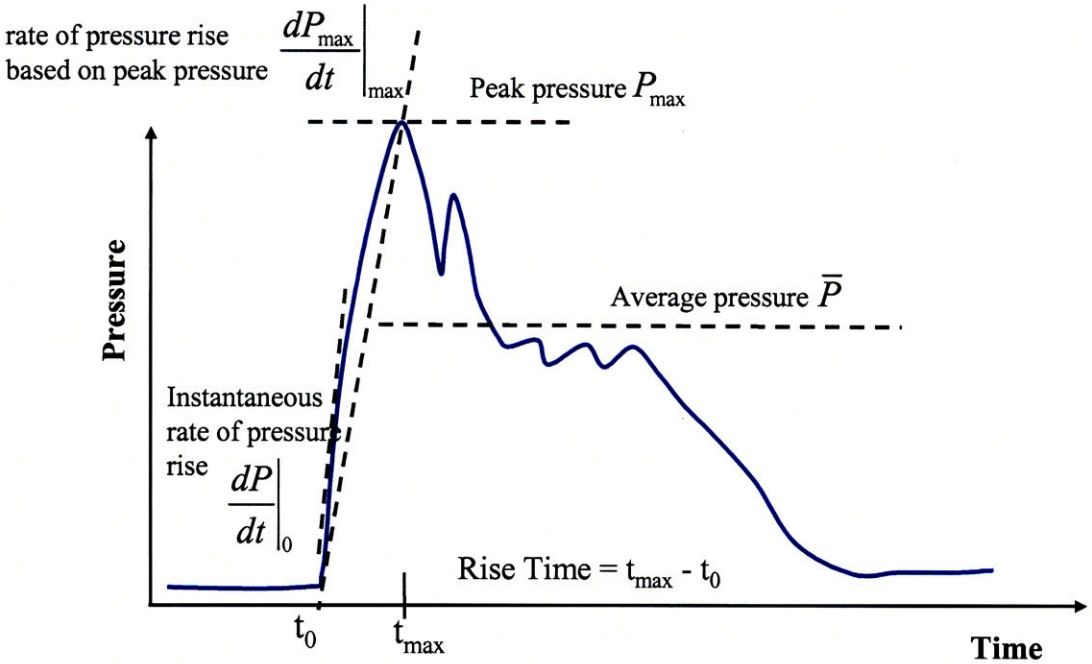

Figure 6.2.3: Sketch of a pressure pulse with definition of typical parameters

The shock wave parameters considered in this study were: rate of pressure rise, peak pressure, average pressure, pulse duration, and impulse; a sketch is shown Figure 6.2.3. The rate of pressure rise $\frac{dP}{dt}$ can be calculated as instantaneous, at every point in time or, as generally done, based on the peak pressure and rise time. Even tough all the parameters play a role in how much damage or injuries can result from a blast wave we focus on the rate of pressure rise because it has been specifically link to lung injuries (as explained in section 2.33).

6.3. Dependence on Fluid Rheology

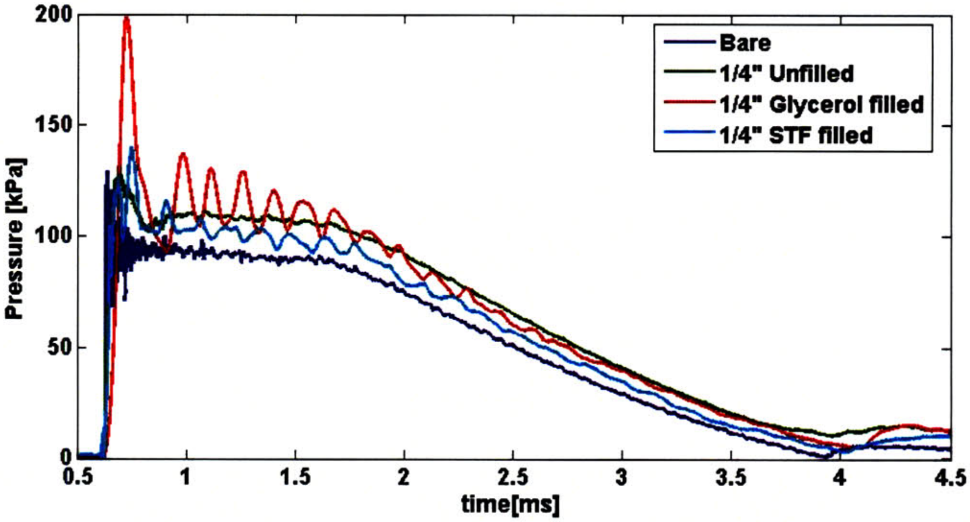

Figure 6.3.1: Pressure pulse of ¼" samples of unfilled, glycerol filled and STF filled composites. The bare signal, with no sample, is also plotted for reference.

Composite made from polyurethane foam filled with either air, STF, or glycerol were tested in the shock tube; Figure 6.3.1 illustrates the results for ¼" thick samples. The presence of the sample was found to increase the overall magnitude of the pressure and at the same time created large spikes in the peak pressure. This effect is well known and documented and is due to the momentum increase due to the additional mass of the samples. This is normally seen in foams that are deforming either in the linear regime (below 5 % for unfilled foam) or collapsing into the densification region. More details of this phenomenon were discussed in section 2.3.5. The rate of the pressure rise, on the other hand, was found to decrease with the presence of fluid filled samples; this is seen in

Figure 6.3.2 where the composite fluid-filling dependence is shown for samples with ½" thickness. For clarity, some of the values of the wave parameters (peak and average pressure and rate of pressure rise) are reported in Table 6.3.1. This clearly shows more than an order of magnitude improvement on the rate of pressure rise for both glycerol and STF filled samples.

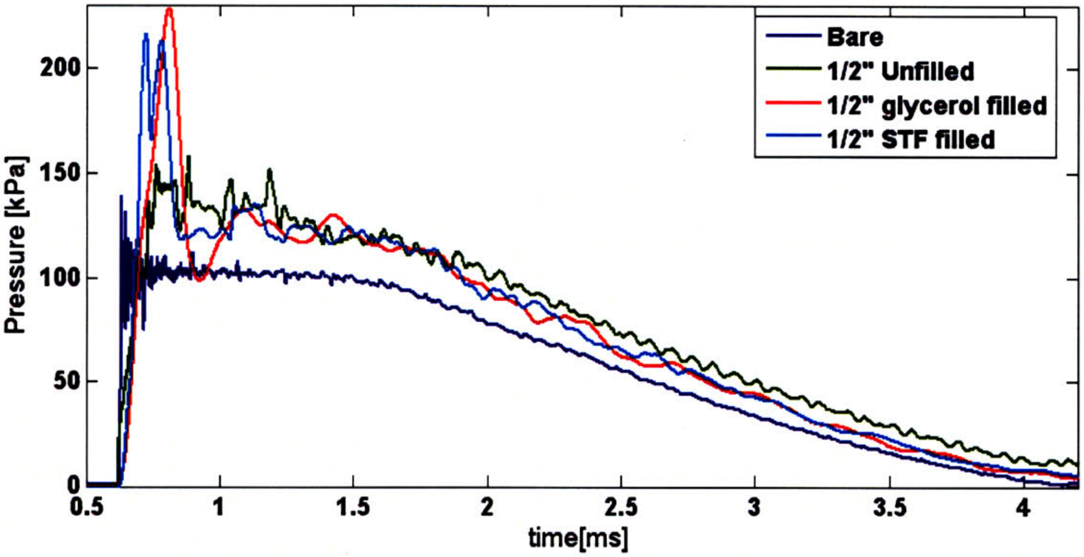

Figure 6.3.2: Pressure pulse measured at the endplate of the shock tube for ½" samples of unfilled, glycerol filled and STF filled composites. The bare signal, with no sample, is also plotted for reference.

	Peak Pressure [kPa]	Average Pressure [kPa]	Rate of Pressure Rise [kPa/s]
Bare	144	100	1.6 x 107
½" Unfilled	151	125	2.5 x 107
½" Glycerol Filled	251	155	3.8 x 106
½" STF Filled	220	112	6.7 x 106

Table 6.3.1: Rate of pressure rise, peak and average pressure for ½" thick samples undergoing shock tube experiments.

The results for single layer composites show that if samples are completely fluid-filled (Ψ=100%) they are able to slow down the rate of pressure rise by one order of magnitude. This is independent of the type of fluid in the composite and therefore does not result from the non-linear response of the shear-thickening suspension; slight variations do occur but the overall behavior is similar. Moreover, the single layer glycerol-filled composites performed better than the STF filled foam. This suggests that, as the wave travels through the sample, the glycerol flows through the foam pores and is able to dissipate energy though the mechanism of viscous dissipation. The STF based composite, on the other hand, thickens and behaves more in a solid like manner than like a fluid, which in this regime is not as efficient in slowing down the pressure wave.

6.4. Volume Fraction Dependence

6.4.1. Glycerol Filled Samples

The volume fraction dependence of the composite was studied for glycerol filled foams of both ¼" and ½" thickness. As the volume fraction of fluid in foam (Ψ) is decreased we found a reduction in the rate of pressure rise; this is illustrated in Figure 6.4.1. The values of peak pressure and rate of pressure rise for these experiments are given in Table 6.4.1. In fact, it is found that by varying the volume fraction we can obtain a reduction in the rate of pressure rise of two orders of magnitude from the incident wave. This reduction is due to the fact that, at lower volume fraction, the fluid can move freely though the pores of the composite, while in 100% filled sample because of the constrained geometry, the fluid has little space to move. As we decrease the amount of fluid in the composite the fluid has more space to move during impact and therefore dissipate energy. Naturally the dissipation is proportional to the amount of fluid and therefore we find an optimal volume fraction, which for these samples was found around 50% - 60%. This is shown in Figure 6.4.2 for both the instantaneous rate of pressure rise and the one based on the peak pressure. A reduction of the peak pressure has also been found as a function of the decreasing volume fraction. This effect is due to the reduced mass and therefore momentum transfer from the sample to the pressure sensor as discusses in section 2.3.5.

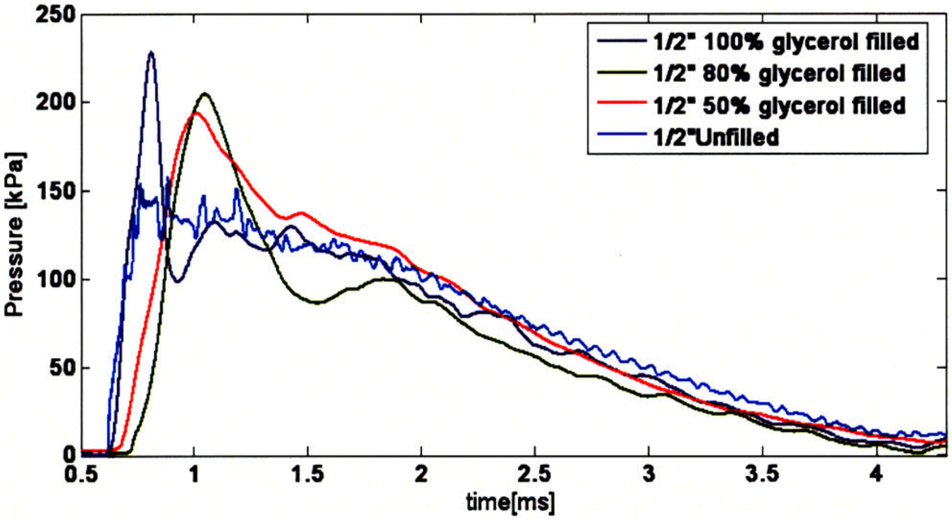

Figure 6.4.1: Pressure pulse measured at the endplate of the shock tube for ½" glycerol filled samples at varying volume fractions. The unfilled foam experiment is also plotted for reference.

	Peak Pressure [kPa]	Rate of Pressure Rise (instantaneous) [kPa/s]	Rate of Pressure Rise (peak) [kPa/s]
Bare	144	1.6×10^7	8.4×10^7
½" Unfilled	151	2.5×10^7	1.1×10^6
½" 100% Gly. Filled	251	3.8×10^6	1.4×10^6
½" 80% Gly. Filled	223	1.8×10^6	6.5×10^5
½" 50% Gly. Filled	194	1.4×10^6	5.0×10^5

Table 6.4.1: Peak pressure and rate of pressure rise both instantaneous and based on peak pressure for ½" thick glycerol-filled samples of different volume fraction.

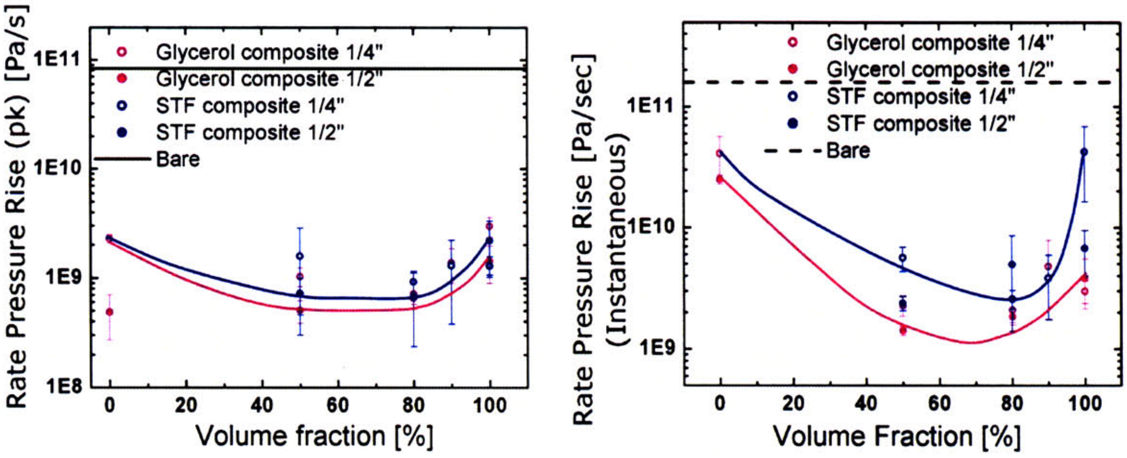

(a) (b)

Figure 6.4.2: (a) Rate of pressure rise based on the value of peak pressure vs. Ψ, volume fraction of fluid in the foam, for both glycerol and STF filled composites. (b) Instantaneous rate of pressure rise vs. volume fraction for both glycerol and STF filled composites.

6.4.2. STF Filled Samples

Volume fraction dependence experiments were also carried out for the silica STF filled composites and are shown in Figure 6.4.3. A reduction in the rate of pressure rise was again found to relate to the reduction of the composite volume fraction, Ψ. Similarly to the results found for the glycerol filled composite and optimal volume fraction around 50% was found as illustrated in Figure 6.4.2.

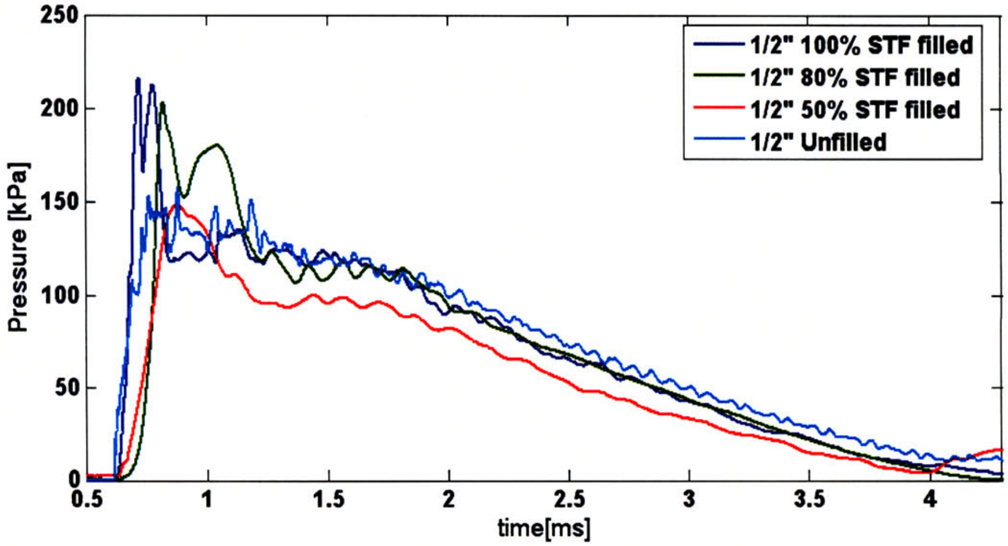

Figure 6.4.3: Pressure pulse measured at the endplate of the shock tube for ½" STF filled samples at varying volume fractions. The unfilled foam experiment is also plotted for reference.

The overall performance of the STF based composite used alone was inferior to the glycerol filled composite. In fact, the greater reduction in the rate of pressure rise (based on peak pressure) for the STF composite was 125 times smaller than the bare signal while for the glycerol filled sample was 170 times. This is related, as explained earlier in section 6.3, to the ability of glycerol to flow though the foam pores and dissipate energy while the STF solidifies and behaves in a solid like manner.

	Peak Pressure [kPa]	**Rate of Pressure Rise (instantaneous) [kPa/s]**	**Rate of Pressure Rise (peak) [kPa/s]**
Bare	144	1.6×10^7	8.4×10^7
½" Unfilled	151	2.5×10^7	1.1×10^6
½" 100% STF Filled	220	6.7×10^6	2.2×10^6
½" 80% STF Filled	168	5.0×10^6	6.7×10^5
½" 50% STF Filled	267	2.6×10^6	8.5×10^5

Table 6.4.2: Peak pressure and rate of pressure rise both instantaneous and based on peak pressure for ½" thick STF filled samples of different volume fraction.

6.5. Dependence on Sample Thickness

Samples of different thicknesses filled to a volume fraction of 100 % were tested and their response compared. Figure 6.5.1 illustrates the difference between glycerol filled samples of two thicknesses. As can be also seen from Table 6.5.1, which contains the average values of parameters for these experiments, we found that the sample thickness affect the peak pressure of the resultant pulse. The increase in the peak pressure is related to the weight of the sample as explained in section 2.3.5 and as found in all other single layer experiments. The rate of pressure rise, on the other hand, is found to be independent of sample thickness. Similar results were found for the shear-thickening fluid filled composites and presented in Figure 6.5.2 are the pressure pulse for STF filled composites with different thicknesses. Again, the rate of pressure rise, both instantaneous and based on peak pressure were found to be statistically equivalent. The peak pressure was also found to increase with thickness and therefore weight, as by now we learned to expect. The average value for the parameters of the pressure waves for the above described experiments are given in Table 6.5.1

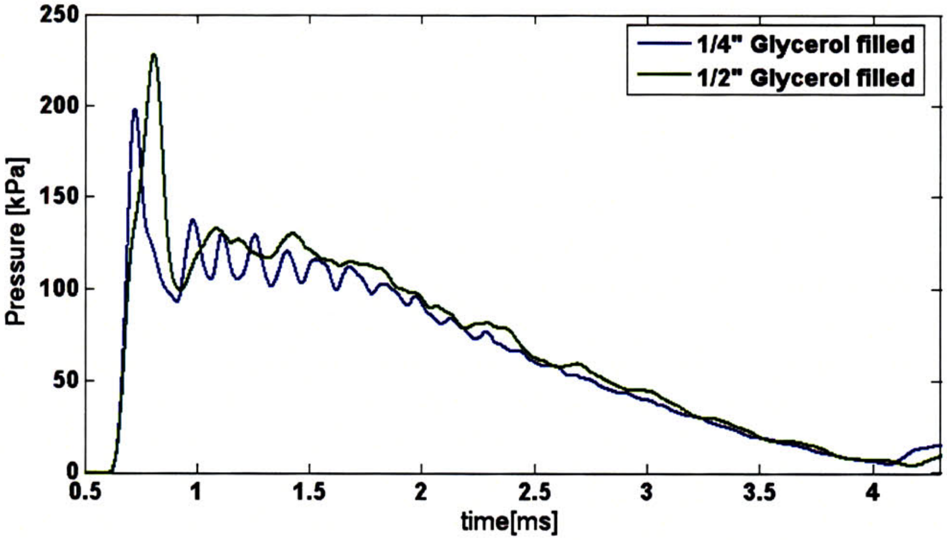

Figure 6.5.1: Pressure pulse measured at the endplate of the shock tube for ½" and ¼" glycerol filled samples (Ψ= 100%).

	Peak Pressure [kPa]	Rate of Pressure Rise (instantaneous) [kPa]	Rate of Pressure Rise (peak) [kPa/s]
½" Unfilled	151	2.5E+07	1.1E+06
¼" 100% Gly. Filled	193	3.0E+06	1.4E+06
½" 100% Gly. Filled	251	3.8E+06	1.4E+06
¼" 100% STF Filled	150	4.2E+07	1.3E+06
½" 100% STF Filled	220	6.7E+06	2.2E+06

Table 6.5.1 : Peak Pressure and rate of pressure rise both instantaneous and based on peak pressure for glycerol and STF filled sample of different thicknesses.

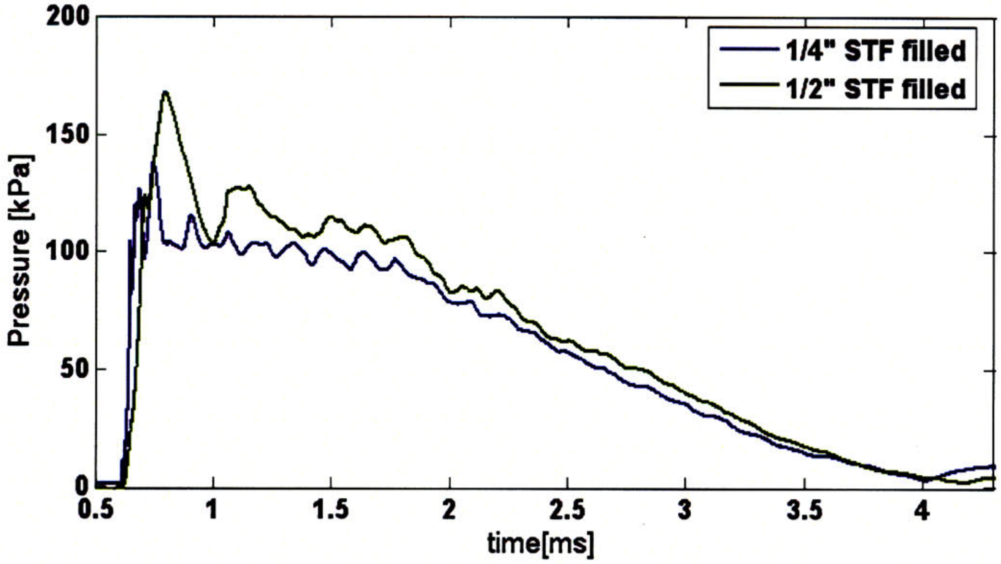

Figure 6.5.2: Pressure pulse measured at the endplate of the shock tube for ½" and ¼" STF filled samples (Ψ= 100%).

6.5.1. Mass Dependence

An attempt to scale out the mass dependence of the composite has been carried out. Results from ½" thickness filled to Ψ=50% and ¼" thick sample filled to Ψ=100% for both glycerol and STF were compared and are shown in Figure 6.5.3. It has been difficult to draw any conclusion from these comparisons as in this case the filling fraction dependence obscures the effect of mass. Another way to scale out the mass dependence is to compare samples with similar weights but different filling fluids as shown in Figure 6.5.4. The average values for the peak pressure for the two composite were found to be statistically equivalent, see Table 6.5.2 for average values. This suggests that for a single layer material the value of the peak pressure is related simply to the weight of the sample.

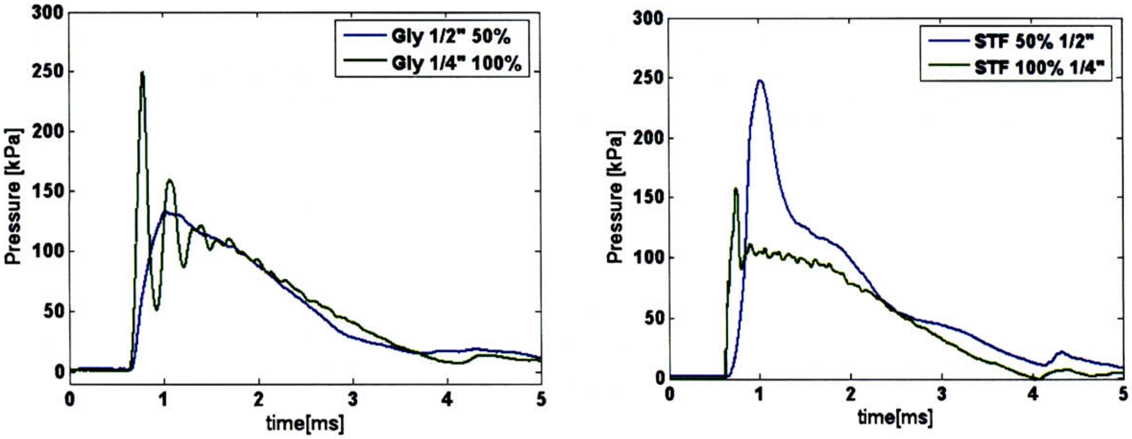

(a) (b)

Figure 6.5.3 (a) Pressure pulse for single-layer glycerol filled composites of ½" thicknesses filled to $\Psi =$ 50% and ¼" thickness filled at $\Psi =$ 100%. (b) Pressure pulse for single-layer STF filled composites of ½" thicknesses filled to $\Psi =$ 50% and ¼" thickness filled at $\Psi =$ 100%.

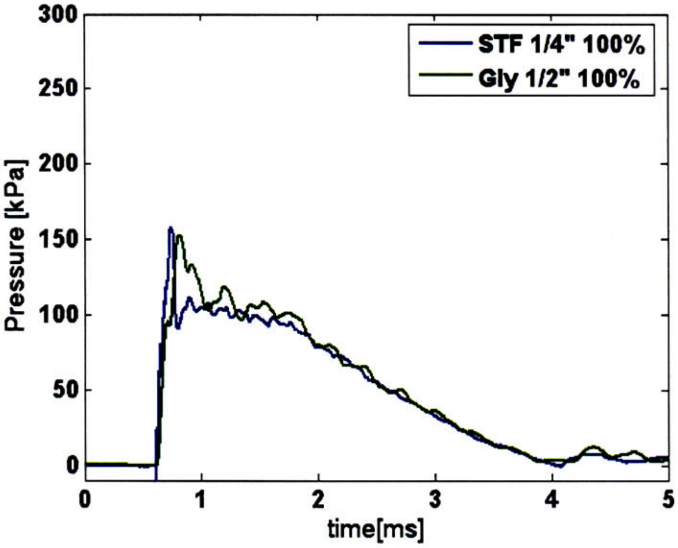

Figure 6.5.4 Pressure pulse for single-layer composites of ½" thicknesses filled with glycerol to $\Psi =$ 100% and ¼" thickness STF filled at $\Psi =$ 100%.

	Peak Pressure [kPa]	Rate of Pressure Rise (peak) [kPa/s]
½" 100% GLY Filled	155	1.4E+06
¼" 100% STF Filled	150	1.3E+06

Table 6.5.2 : Peak Pressure and rate of pressure rise based on peak pressure for single-layer composites of ½" thicknesses filled with glycerol to $\Psi =$ 100% and ¼" thickness STF filled at $\Psi =$ 100%.

6.6. Layered Composites

As discussed in detail in section 2.3.4, blast mitigation has been achieved previously by using a method of layering hard plates with elastomeric foam. The reduction of accelerations achieved with these systems were said to be due to the impedance mismatch between the solid and the foam layer.

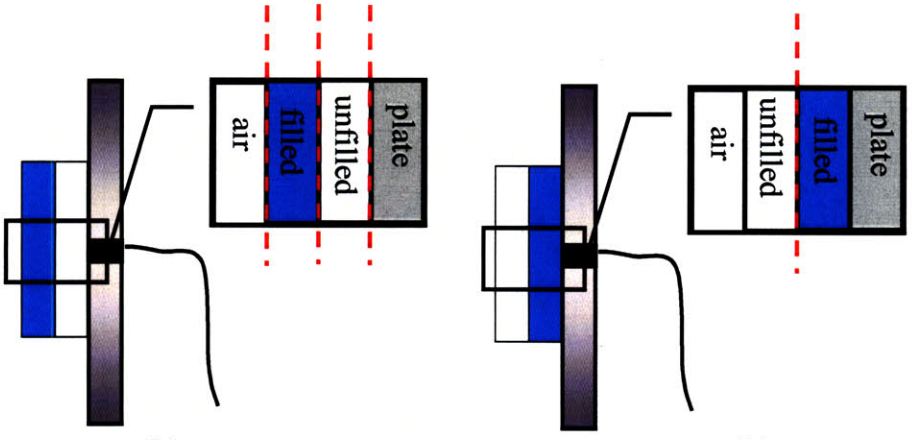

(a) (b)

Figure 6.6.1: (a) Sketch of sample with heavy layer (fluid filled) facing the incoming wave. This setup allows for 3 interfaces of high impedance mismatch. (b) Sketch of sample with light layer (unfilled) facing the incoming wave. This setup allows for 1 interfaces of high impedance mismatch.

In this study we try to exploit the same mechanism but replace the hard plate with a STF based composite. This would have, of course, many advantages as, for example flexibility, the potential to follow more closely body shape and therefore improve coverage.

Two different geometries were tested: one with the heavy layer facing the incoming wave, the other with the light layer (foam) facing the wave, a sketch of the geometries is given in Figure 6.6.1. Results for glycerol filled composites, illustrated in Figure 6.6.2, show that the layered composite is capable of reducing the rate of pressure rise and that different results are obtained depending on the layers order. A reduction of two orders of magnitude was achieved, specifically a 100 times reduction for geometry (b) from Figure 6.6.1 and a 300 times reduction in the rate of pressure rise for geometry (a) of Figure 6.6.1 (where the filled composite is facing the incoming wave). Unlike the results for a single layer of the fluid filled composite, the layered geometry did not produced a spike in the peak pressure which is seen to remain relatively constant.

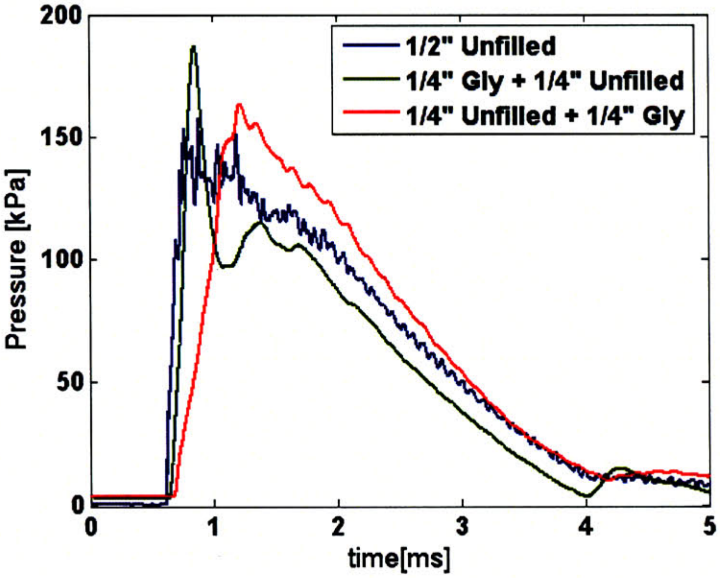

Figure 6.6.2: Pressure pulse measured at the endplate for layered composite of ¼" unfilled foam and ¼" thick glycerol filled samples in both configurations as shown in Figure 6.6.1

Similar results were found for the layered STF filled composite. In fact a reduction of the rate of pressure rise of 2 order of magnitude was found, more specifically a reduction of 100 times for geometry (b) from Figure 6.6.1 and a reduction of about 600 from the bare signal for geometry (a) of Figure 6.6.1.

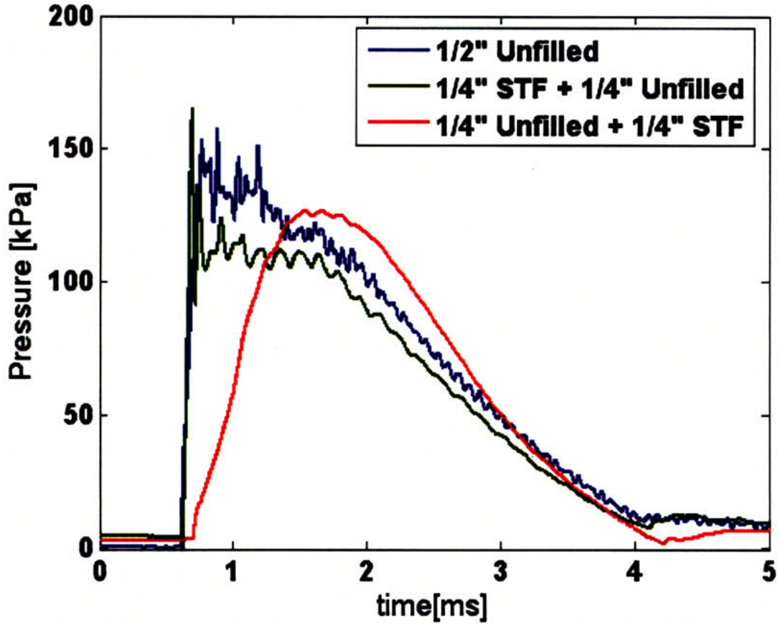

Figure 6.6.3: Pressure pulse measured at the endplate for layered composite of ¼" unfilled foam and ¼" thick STF filled samples in both configurations as shown in Figure 6.6.1

For the case of layered composite with the light layer facing the incoming wave we notice that the pressure pulse is very similar to the one found for a single layer fluid filled sample, see Figure 6.6.5 for geometries. In fact if we compare the two samples, as done in Figure 6.6.4 we see very little difference in the response of the two samples. This result has been found in both glycerol and STF filled composites and suggests that, when facing the wave the light layer of unfilled foam does not add to the energy absorption of the system.

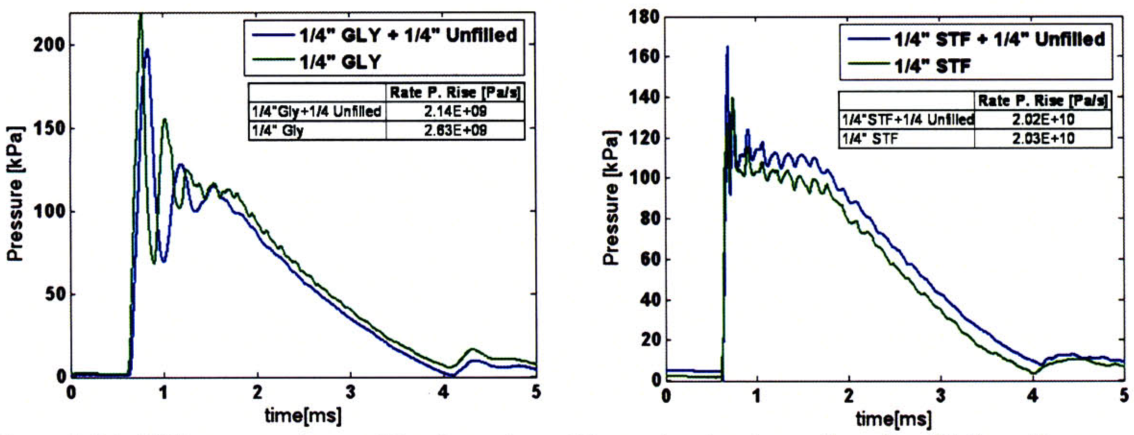

Figure 6.6.4: (a) Pressure pulse resulting from glycerol layered system in configuration (b) from Figure 6.6.1 and single-layer glycerol-filled composite. (b) Pressure pulse resulting from STF layered system in configuration (b) from Figure 6.6.1 and single-layer STF-filled composite.

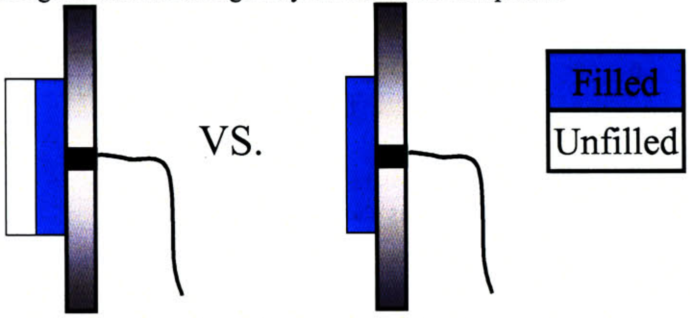

Figure 6.6.5: (left) Geometric configuration of sample with light layer of foam facing the incoming wave. (right) Single layer geometry of fluid filled composite.

6.6.1. Mass-Spring-Damper Model

A mass-spring-damper model has been used to simulate the response of the layered composite; a sketch of the system is given in Figure 6.6.1. The model was fed the bare signal as input and the simulation data was matched with the real data by optimization of the system parameters. The model was then used to match the layered composite response with both geometries, heavy layer facing the wave and light layer facing the wave.

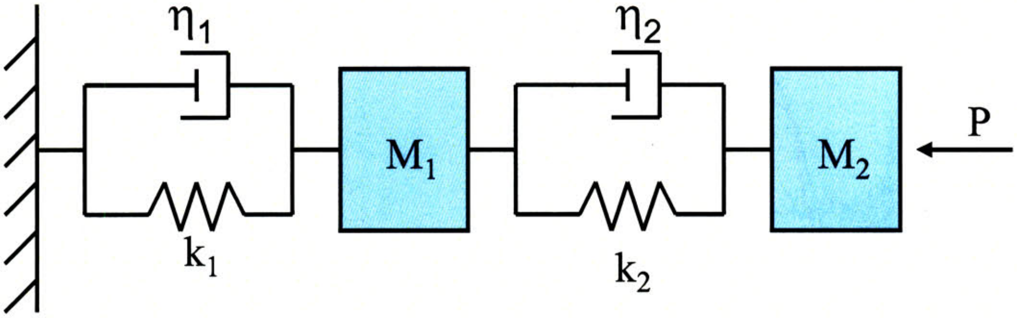

Figure 6.6.6: Mass-spring-damper model utilized for the simulations of the layered composite. η_1, k_1, M_1, η_2, k_2, M_2 represent the system parameters, P is the incoming pressure pulse.

Figure 6.6.7 illustrates the results for the two layers glycerol-filled composite with the light layer (unfilled foam) facing the incoming wave. The green data represents the incoming pressure pulse, while the blue data is the prediction form the model; the parameters used to match the data are given in Table 6.6.1. The model does reasonably well in predicting the rate of pressure rise and peak pressure; see Table 6.6.2 for values, even tough some problems still remain in trying to match the overall data. The simulation was found to predicts large oscillations which are not seen in the results form real data.

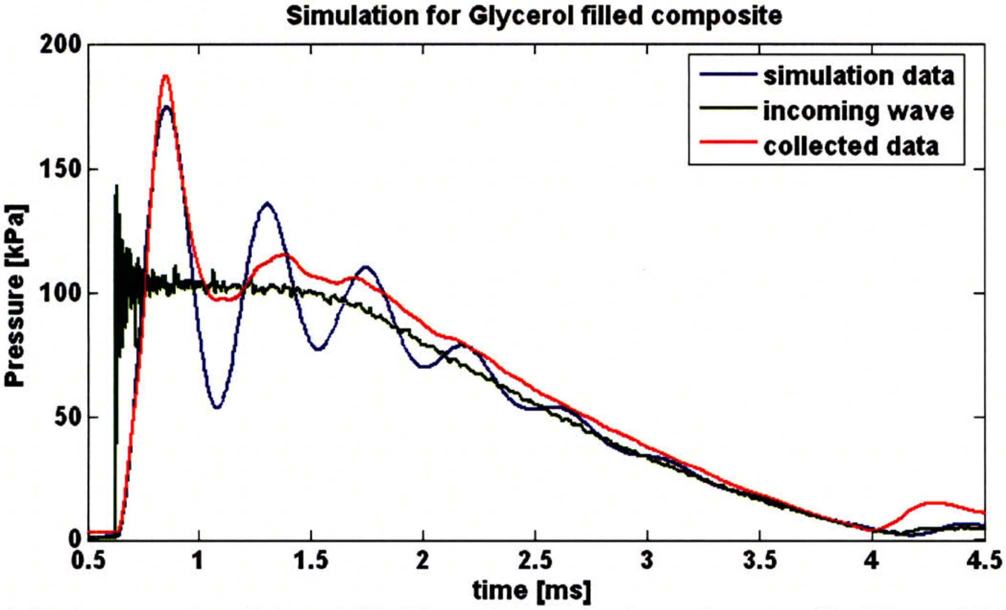

Figure 6.6.7: Pressure pulse of glycerol-filled layered-composite for configuration (b) of Figure 6.6.1 with light layer facing wave. Plotted in blue are the predictions from the simulation.

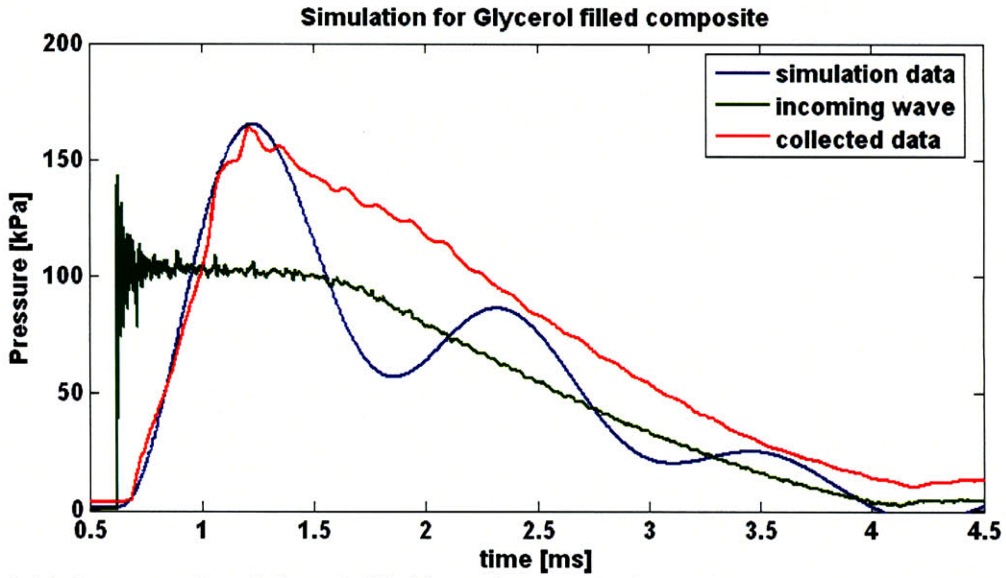

Figure 6.6.8: Pressure pulse of glycerol-filled layered-composite for configuration (b) of Figure 6.6.1 with heavy layer facing wave. Plotted in blue are the prediction from the simulation.

	k [Nm^{-1}]	M [kg]	η [Nm^{-2}]
Unfilled Layer	5×10^7	0.01	3200
Glycerol Layer	3×10^8	1.5	5000

Table 6.6.1: Parameters used by the model to match the glycerol-filled layered composite response.

Similarly, when we switch the order of the layers we still find a reasonable match between the model prediction and the real data for the peak pressure and the rate of pressure rise based on peak pressure. Details on the actual values for these parameters can again be found in Table 6.6.2.

Sample	Ppeak [kPa]	Rate P. Rise (instantaneous) [kPa/s]	Rate of P. Rise (Peak) [kPa/s]
Layered Glycerol (light layer facing wave)	176	2.6E6	7.3E5
Layered Glycerol (light layer facing wave) Model	175	1.2E6	8.0E5
Layered Glycerol (heavy layer facing wave)	160	4.1E6	2.9E5
Layered Glycerol (heavy layer facing wave) Model	165	4.4E5	2.8E5
Layered STF (light layer facing wave)	185	1.7E6	2.0E5
Layered STF (light layer facing wave) Model	183	3.2E6	2.8E5
Layered STF (heavy layer facing wave)	127	1.3E6	1.5E5
Layered STF (heavy layer facing wave) Model	130	2.2E5	1.4E5

Table 6.6.2: Average values of rate of pressure rise and incoming pressure for layered glycerol-filled and STF-filled composites. The prediction from the mass-spring-damper model are also included

The data for the STF filled layered composite has also been matched with the model predictions; the model parameters used are given in Table 6.6.3. In order to optimized the match of the STF data the values for the unfilled foam previously used (glycerol layered composite) had to be modified. Similarly to what found for the glycerol based composite the model prediction matches the values of the rate of pressure rise and the peak pressure reasonably well even tough the shape of the pulse was not exactly matched; for the values of the wave parameters see Table 6.6.2. Figure 6.6.9 and Figure 6.6.10 show the pressure pulse for the STF based composite and the model predictions for both geometry (a) and (b) of Figure 6.6.1. In particular, the data for the STF composite with the foam layer facing the wave was particularly hard to predict as the model had difficulty in predicting the very high rate of pressure rise without incurring in high frequency oscillation as seen in Figure 6.6.10

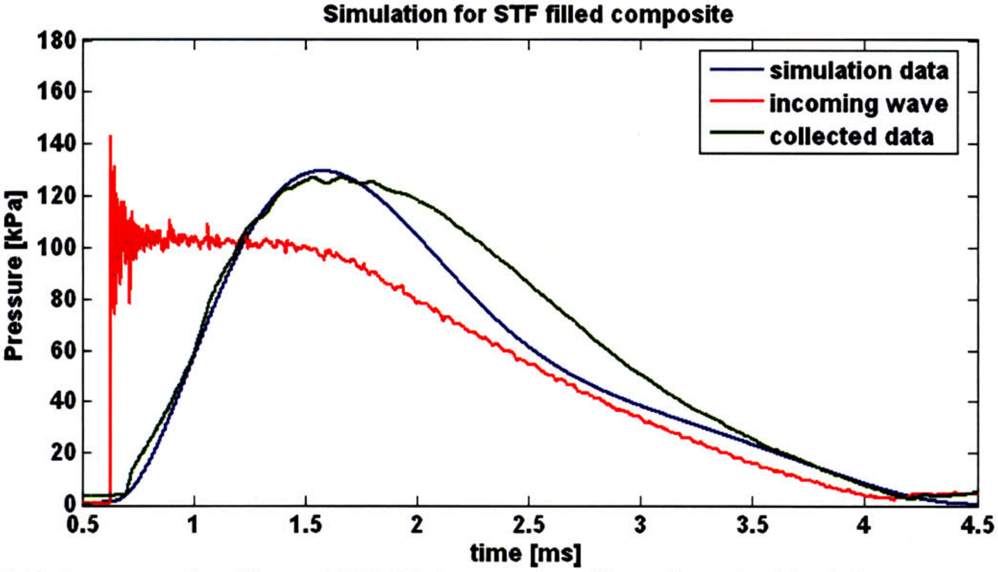

Figure 6.6.9: Pressure pulse of layered STF filled composite with configuration (a) of Figure 6.6.1 with heavy layer facing wave. Plotted in blue are the results from the simulation.

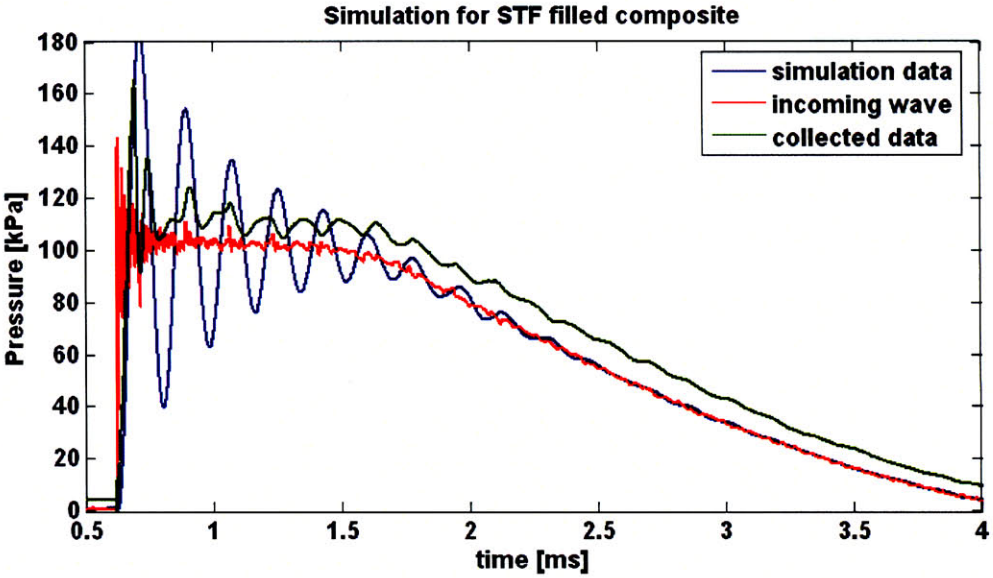

Figure 6.6.10: Pressure pulse of layered STF filled composite with configuration (b) of Figure 6.6.1 with light layer facing wave. Plotted in blue are the results from the simulation.

	k [Nm^{-1}]	M [kg]	η [Nm^{-2}]
Unfilled Layer	5×10^{8}	0.01	1.1×10^{5}
STF Layer	5×10^{10}	40	2×10^{5}

Table 6.6.3: Parameters used by the model to match the layered STF filled composite response.

In general, the behavior seen from the layered samples can be reproduced by the simple mass-spring-damper model. The model follows very closely the behavior of the filled composite for both geometries. Some discrepancies do arise when trying to match the whole curve for the pressure pulse, but the overall trend is reasonably followed.

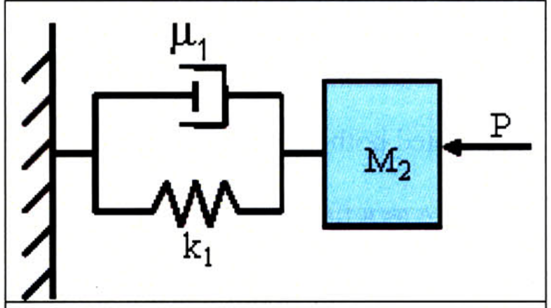

Figure 6.6.11 Simplified single mass-spring-damper model utilized for the simulations of the STF layered composite, *P* represents the incoming pressure pulse.

For the case of STF-filled samples the double mass-spring-damper system can be further simplified by utilizing the parameter values used to fit the data. In fact, we note that $M_{STF} \gg M_{unfilled}$ and $k_{STF} \gg k_{unfilled}$: this allows us to reduce the system to a single mass-spring-damper, as shown in Figure 6.6.11, with stiffness $k_1 = k_{unfilled}$, $M_2 = M_{STF}$ and $\mu_1 = \mu_{unfilled}$. The governing equation for this system is:

$$M_2\ddot{x}+\mu_1\dot{x}+k_1=F \qquad (6.1).$$

From equation (6.1) we can define a frequency and damping ratio as follows:

$$\omega=\sqrt{\frac{k_1}{M_2}} \qquad \zeta=\frac{\mu_1}{2\sqrt{k_1 M_2}} \qquad (6.2).$$

To analyze the response of this system we imposed a forcing step function and we studied the resultant pressure pulse as a function of ζ see Figure 6.6.12.

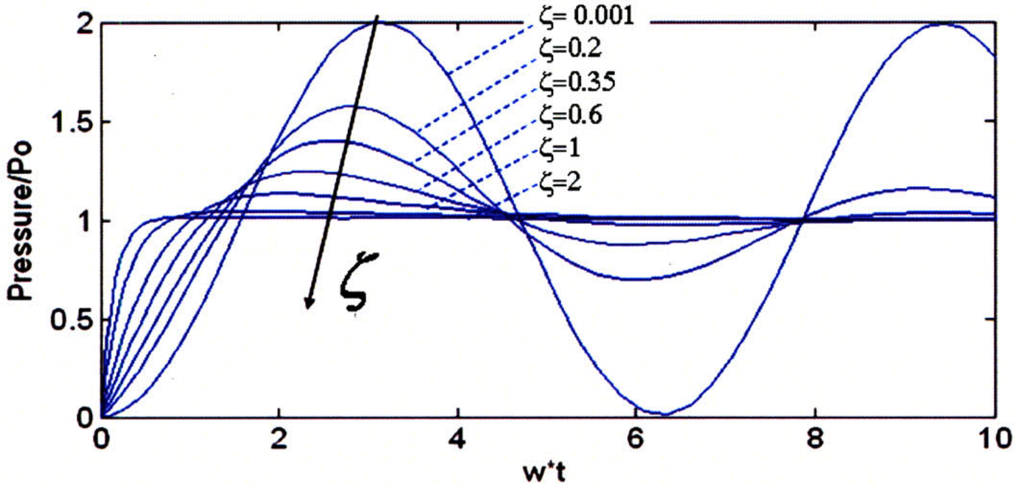

Figure 6.6.12: Pressure profiles for the single mass-spring-damper system as a function of nondimensional time for a number of values of ζ.

As explained earlier in section 2.3.3 the rate of pressure rise of the pulse has been related to lung's injuries. To optimize this system for blast mitigation applications we calculated both the instantaneous rate of pressure rise and the one based on the peak pressure as a function of ζ ; this is illustrated in Figure 6.6.13. As you can observe from Figure 6.6.13 the nondimensional instantaneous rate of pressure rise has a minimum at $\varsigma = 0.26$ while the nondimensional rate of pressure rise based on peak pressure and rise time has a minimum at $\varsigma = 0.5$. This result indicates that in order to minimize both rates of pressure rises and therefore mitigate blast injuries the system parameters should follow the condition:

$$0.26 \le \zeta = \frac{\mu_1}{2\sqrt{k_1 M_2}} \le 0.5 \qquad (6.3).$$

To note that the damping ratio for the STF based composite is $\zeta_{STF} = 0.36$, which is right in between the two minimums of rate of pressure rise.

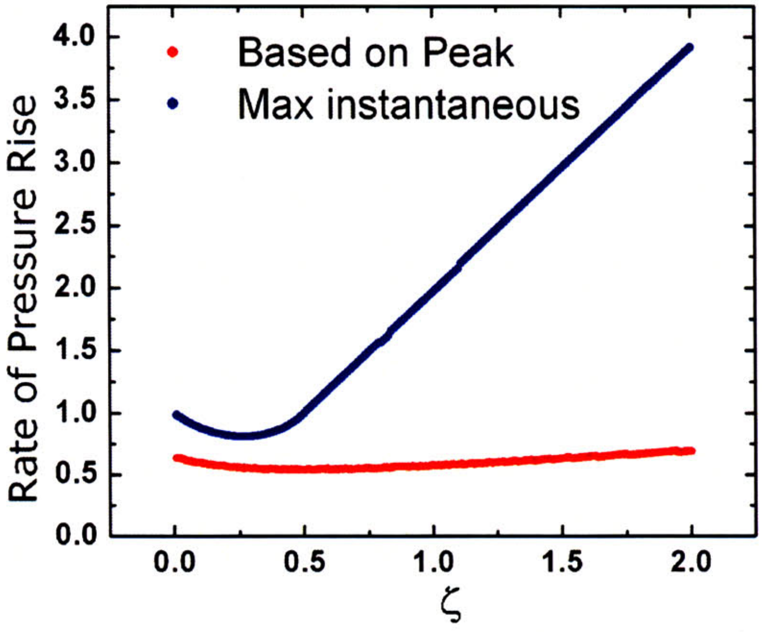

Figure 6.6.13: Rate of pressure rise, both instantaneous and based on peak pressure calculated with the single mass-spring-damper model as a function of ζ .

6.7. Dependence on Number of Layers

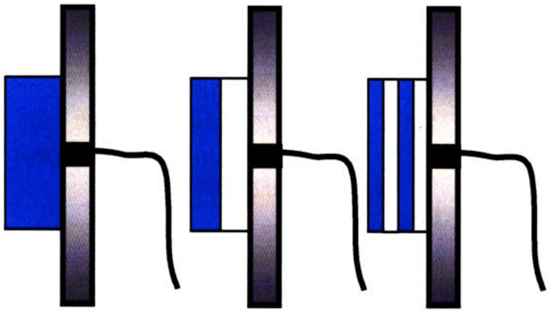

Figure 6.7.1: Geometric configuration of single-layer fluid-filled sample on the left, two-layer sample with fluid filled layer facing the incoming wave and four-layer sample with fluid filled layer facing the incoming wave on the right.

A geometric configuration with four layers, two of unfilled foam and two of fluid filled foam, see Figure 6.7.1(right), have been tested. The layers were cut to be 1/8" so that the total sample thickness amounted to ½" as in the two-layer samples; consequently the weight of the samples also matched. Results for glycerol filled samples presented in Figure 6.7.2 show that the pressure pulse for the four-layer composite is the same (statistically equivalent) as the two-layer geometry. In fact the rate of pressure rise for the four-layer composite was found to be 300 times smaller than the bare wave which is the same found for the two-layer sample. The peak pressure for the four-layer composite also matched the results from the two–layer. We notice that despite the fact that the samples all have the same weight, the peak pressure is lower for the single layer sample filled to 50%. This is in disagreement with what described in section 6.5.1 where we found that for single layer materials the peak pressure was dependent only on the weight of the sample; for the layered composite a more complex dependence is found.

Similar results were found for STF filled samples with four-layer geometry, see Figure 6.7.3. For this case the rate of pressure rise was found to be 600 times smaller than the bare wave as found for the two-layer system and reported in section 6.6. The peak pressure also matched and was found to be much smaller than the value found for the single layer STF filled to $\Psi = 50\%$.

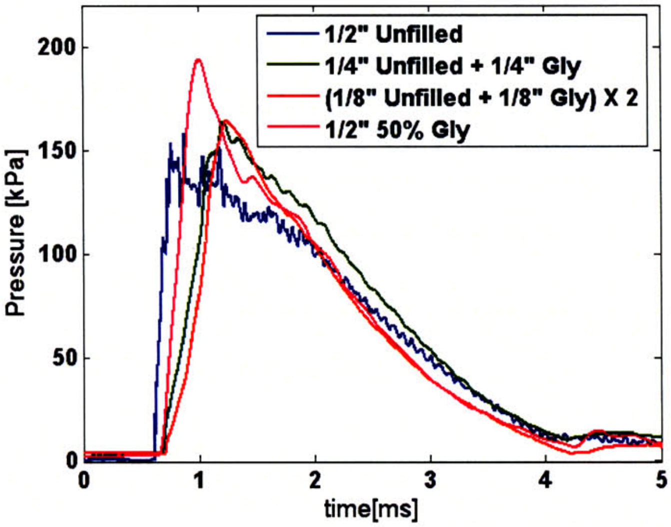

Figure 6.7.2: Pressure pulses for glycerol filled composites as in geometries illustrated in Figure 6.7.1, the pressure pulse for ½" thick unfilled foam is also plotted for reference.

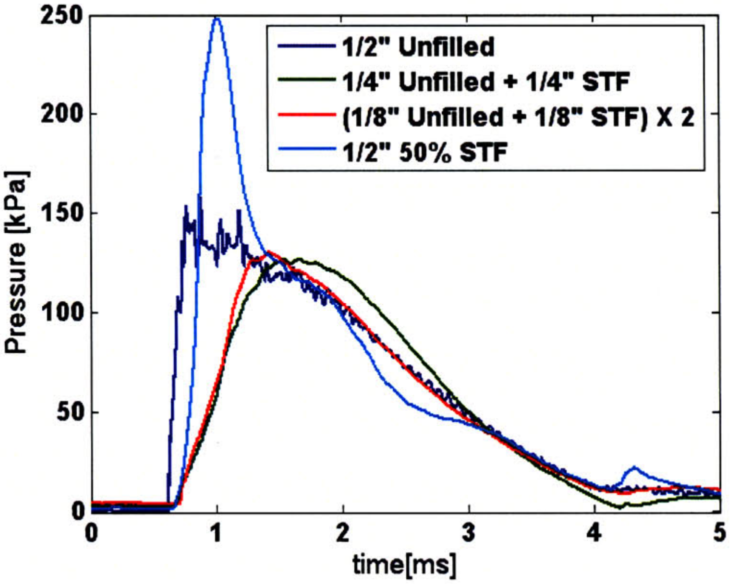

Figure 6.7.3: Pressure pulses for STF filled composites as in geometries illustrated in Figure 6.7.1, the pressure pulse for ½" thick unfilled foam is also plotted for reference.

The fact that the pressure pulses did not vary when we increased the number of layers suggests that, in these composites, the number of high impedance mismatch interfaces does not affect the transmission of the pressure pulse. Geometries with a greater number of layers were not tested because of the limit on how small the layers can be and still expect the same energy absorption mechanism to be important. In fact a 1/8" layer correspond to about 3 mm in thickness but the average pore size for this foam is 360 μm which allows for 10 pores in thickness. Below this threshold of 10 pores we don't expect the system to behave in the same manner, and we do expect other energy absorption mechanisms to become more important.

The spring-mass-damper model presented in section 0 was modified to represent the four-layer geometry; a sketch of the model is shown in Figure 6.7.4. For these geometries the model was not a good fit for the data. In fact the model overestimated the peak pressure while underestimating the rate of pressure rise, see Table 6.7.1. The data for the layered glycerol filled samples and the model prediction are shown in Figure 6.7.5 while the results for the STF based composite are shown in Figure 6.7.6.

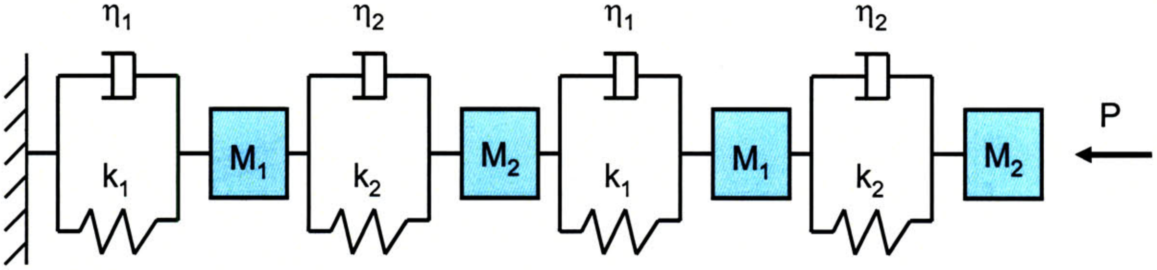

Figure 6.7.4: Mass-spring-damper model utilized for the simulations of the four-layer composite. η_1, k_1, M_1, η_2, k_2, M_2 represent the system parameters, P is the incoming pressure pulse.

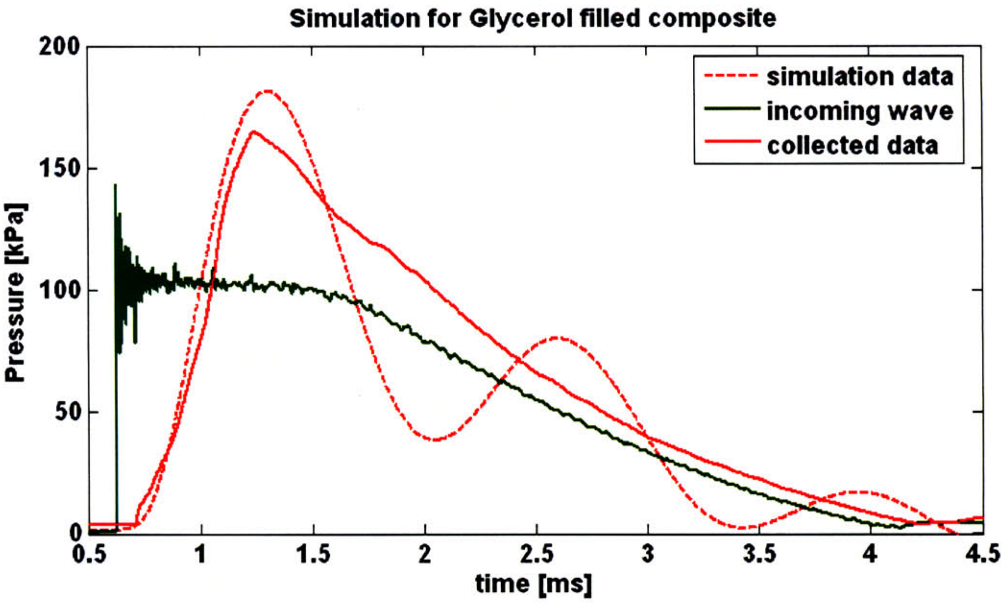

Figure 6.7.5: Pressure pulse for glycerol filled composite with four-layer; the dashed line corresponds to the model prediction.

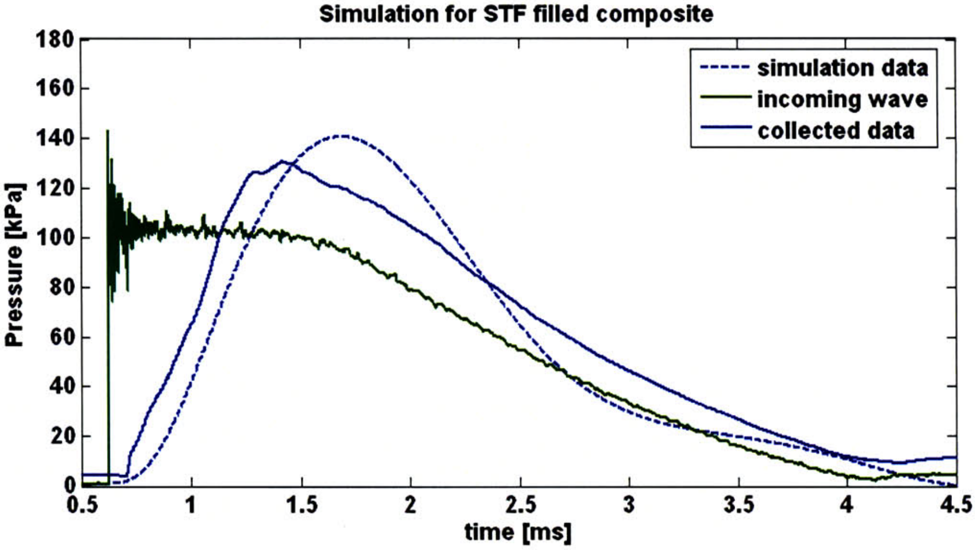

Figure 6.7.6: Pressure pulse for STF filled composite with four-layer; the dashed line corresponds to the model prediction.

	Peak Pressure [kPa]	Rate of Pressure Rise (peak) [kPa/s]
½" 4 layers Glycerol filled model	181	2.1E+05
½" 4 layers Glycerol filled	164	2.4E+05
½" 4 layers STF filled model	141	1.4E+05
½" 4 layers STF filled	138	1.8E+05

Table 6.7.1: Peak pressure and rate of pressure rise based on peak pressure for both glycerol and STF filled four-layer samples. The prediction from the mass-spring-damper model is also included.

6.8. Dependence on Overpressure

6.8.1. Single-Layer Composites

Experiments were conducted where the magnitude of the incoming wave was varied by changing the thickness of the diaphragm of the shock tube. The shape and magnitude of the resulting pressure profiles were then studied as a function of incoming pressure. Single layer composites where investigated, in particular we report the results for a glycerol filled sample with $\Psi = 80\%$, see Figure 6.8.1 , but similar results were found for all single-layer fluid-filled composites. For these experiments 2Al, 3Al, and 5Al refer to the number of aluminum layers that constituted the diaphragm and therefore represent the change in incoming pressure. A linear dependence between the rate of pressure rise, based on peak pressure, and the incoming pressure was found. This relation is shown in Figure 6.8.2(a), where the average values of the rate of pressure rise have been plotted against the incoming pressure. Similarly, the values of the peak pressure were found to depend linearly on the incoming pressure, but on the other hand, the instantaneous rate of pressure rise was not, see Figure 6.8.2(b). For reference the average values for both rates of pressure rise and peak pressure are given in Table 6.8.1.

The linear dependence found in the single layer samples suggests that the matrix contribution to the stress is small in this regime, as the foam has a non-linear behavior, while the stress contribution from the fluid flow constitutes the major part of the composite response.

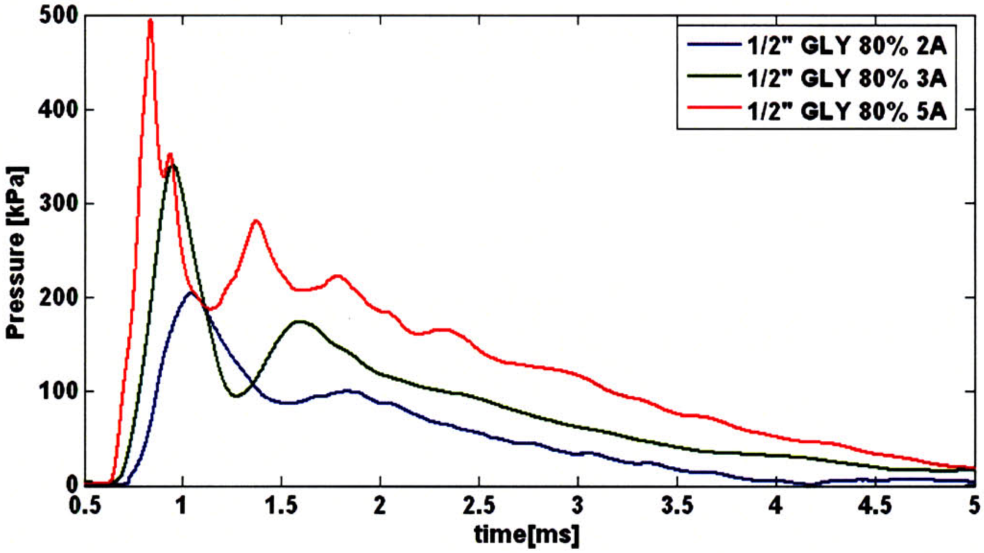

Figure 6.8.1: Pressure profiles of single-layer glycerol-filled samples with volume fraction $\Psi = 80\%$ as a function of incoming pressure. 2Al, 3Al, and 5Al refer to the number of aluminum layers that constituted the diaphragm and therefore represent the increase in the incoming pressure.

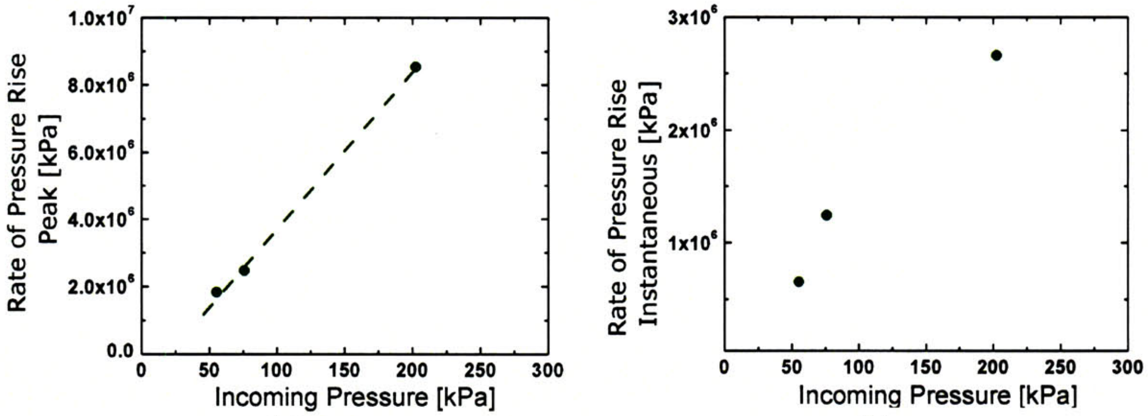

(a) (b)

Figure 6.8.2: (a) Average values of rate of pressure rise based on peak pressure as a function of incoming pressure for single-layer glycerol-filled samples with volume fraction $\Psi = 80\%$. (b) Average values of instantaneous rate of pressure rise as a function of incoming pressure for single-layer glycerol-filled samples with volume fraction $\Psi = 80\%$.

Sample	Pin [kPa]	Ppeak [kPa]	Rate P. Rise (instantaneous) [kPa/s]	Rate of P. Rise (Peak) [kPa/s]
Ψ=80% Glycerol filled 2A	55	220	1.8E6	6.5E5
Ψ=80% Glycerol filled 3A	76	360	2.5E6	1.2E6
Ψ=80% Glycerol filled 5A	202	500	8.5E6	2.7E6

Table 6.8.1: Average values of rate of pressure rise and incoming pressure for single-layer glycerol-filled composites at $\Psi = 80\%$.

6.8.2. Multilayer Glycerol Based Composites

As found for single layer composites and described in section 6.8.1 the rate of pressure rise based on peak pressure for glycerol-filled layered composite was also found to relate linearly with the incoming pressure. Figure 6.8.3 reports the pressure pulse for the glycerol-filled composites as a function of three different incoming pressures. From this graph we find that the curves are self similar, and that indeed the rate of pressure rise and the peak pressure vary linearly with the incoming pressure, these relations are plotted in Figure 6.8.4. As for the single layer composite, this linearity was not found for the instantaneous rate of pressure rise as Figure 6.8.5 illustrates.

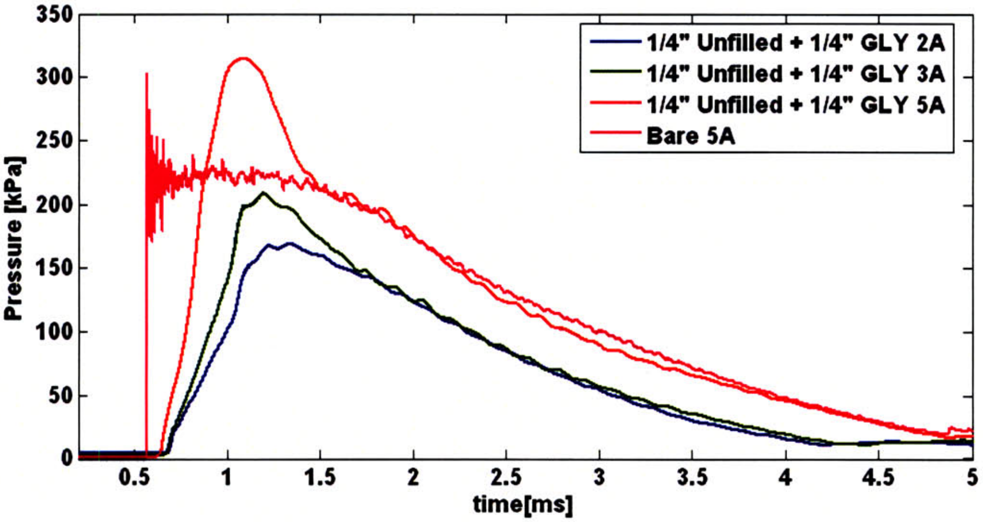

Figure 6.8.3: Pressure profiles for glycerol-filled layered composites as a function of incoming pressure. The incoming pressure wave at 5Al is shown for reference. 2Al, 3Al, and 5Al refer to the number of aluminum layers that constituted the diaphragm and therefore represent the increase in the incoming pressure.

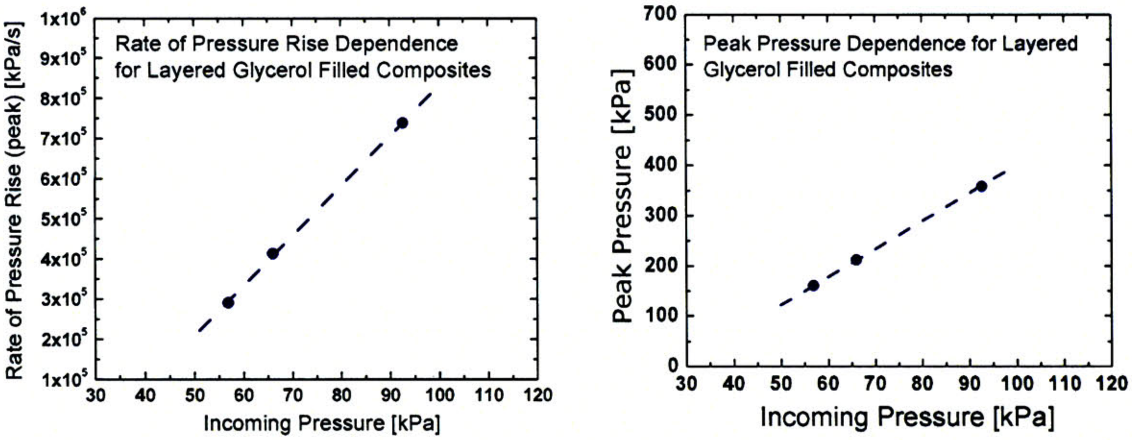

(a) (b)

Figure 6.8.4: (a) Average values of rate of pressure rise based on peak pressure as a function of incoming pressure for glycerol-filled layered composites. (b) Average values of peak pressure as a function of incoming pressure for glycerol-filled layered composites.

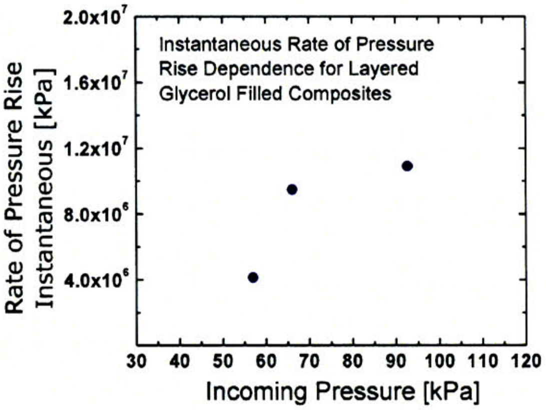

Figure 6.8.5: Average values of instantaneous rate of pressure rise as a function of incoming pressure for glycerol-filled layered composites.

The composite behavior and its linear relation with the incoming pressure are well captured by the spring-mass-damper model presented in section 0. The model was fed the bare signal for 2A, 3A and 5A and the result data together with the model predictions are shown in Figure 6.8.6.

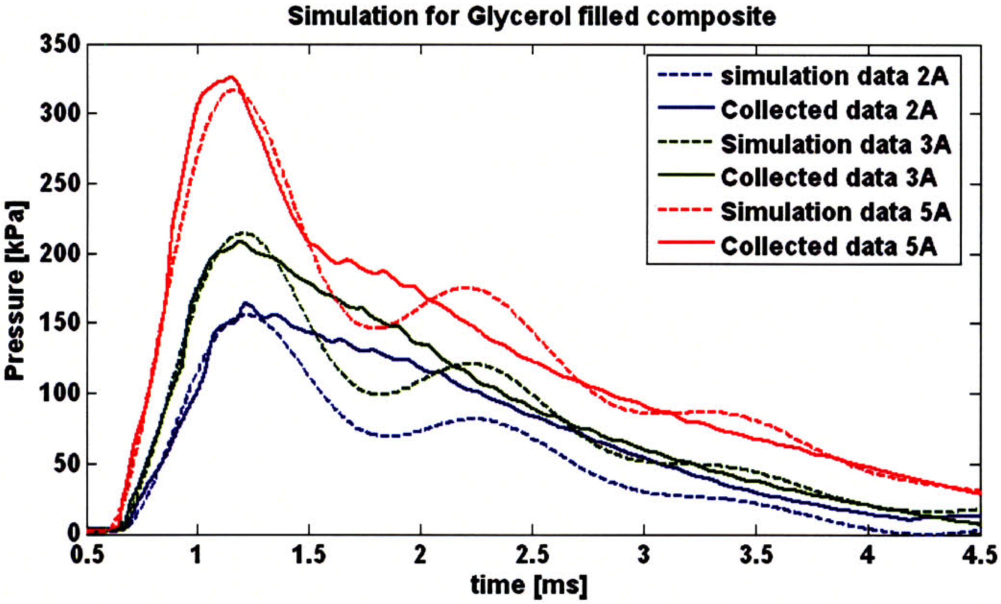

Figure 6.8.6: Pressure profiles for glycerol-filled layered composites as a function of incoming pressure. The dashed lines correspond to the model predictions.

Sample	Ppeak [kPa]	Rate P. Rise (instantaneous) [kPa/s]	Rate of P. Rise (Peak) [kPa/s]
Layered Glycerol 2A	160	4.1E6	2.9E5
Layered Glycerol 2A Model	165	4.4E5	2.8E5
Layered Glycerol 3A	212	9.5E6	4.1E5
Layered Glycerol 3A Model	224	6.0E5	3.9E5
Layered Glycerol 5A	327	1.2E7	6.5E5
Layered Glycerol 5A Model	336	8.9E5	6.0E5

Table 6.8.2: Average values of rate of pressure rise and incoming pressure for layered glycerol-filled composites; model predictions are also included.

6.8.3. Multilayer STF Based Composites

Results similar to what found for the glycerol based composites were found for the STF filled composites see Figure 6.8.7. The rate of pressure rise based on peak pressure, shown in Figure 6.8.8(a), was again found to vary linearly with the incoming pressure, while the instantaneous rate of pressure rise was not, see Figure 6.8.8(b). Despite the fact that the STF in non-Newtonian the system still behaved linearly with respect to the incoming pressure.

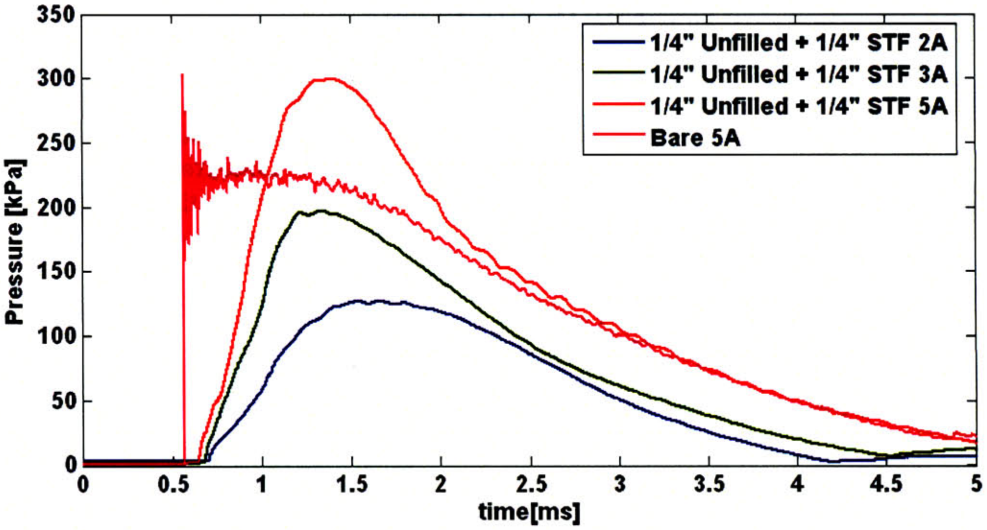

Figure 6.8.7 Pressure profiles for STF-filled layered composites as a function of incoming pressure. The incoming pressure wave at 5Al is shown for reference. 2Al, 3Al, and 5Al refer to the number of aluminum layers that constituted the diaphragm and therefore represent the increase in the incoming pressure.

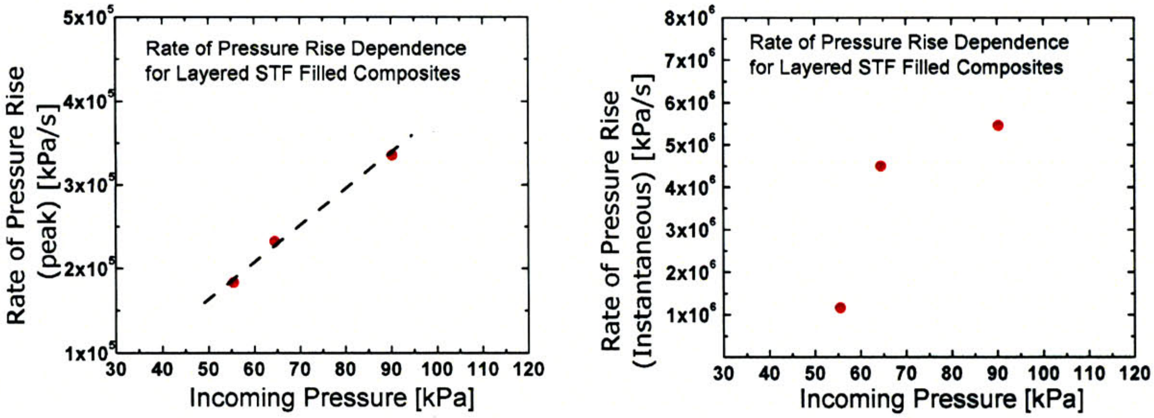

(a) (b)

Figure 6.8.8: (a) Values of rate of pressure rise based on peak pressure as a function of incoming pressure for STF-filled layered composites. (b) Values of instantaneous rate of pressure rise as a function of incoming pressure for STF-filled layered composites.

The behavior for the STF based composite was compared with the prediction of spring-mass-damper model which are shown in Figure 6.8.9; a very good agreement between the data and the model is found. Again the peak pressure and rate of pressure rise were very well predicted but the model was not able to match the whole shape of the pulse. Table 6.8.3 presents the average values of the pressure pulse parameters and the model prediction.

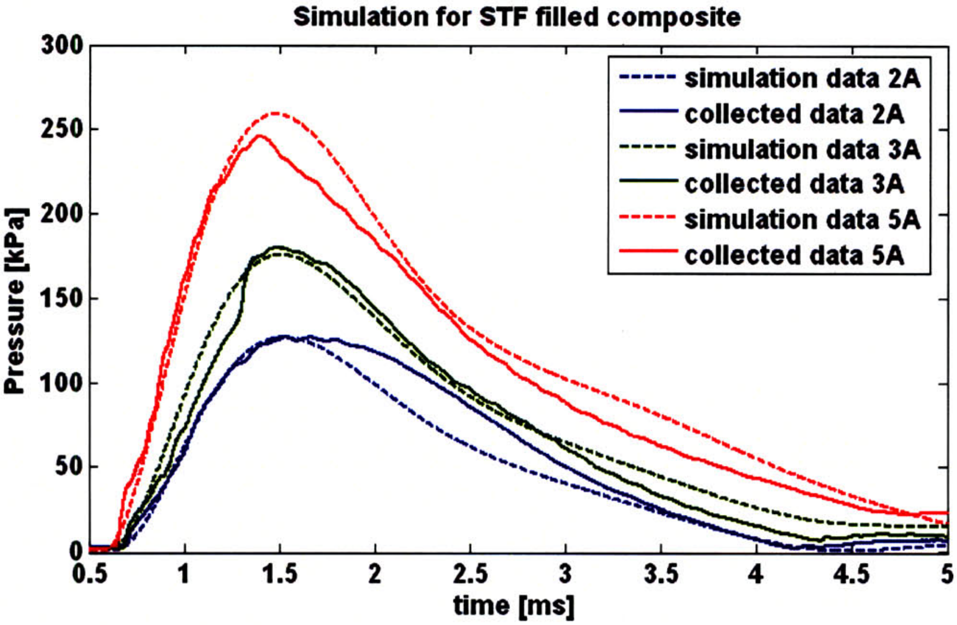

Figure 6.8.9: Pressure profiles for STF-filled layered composites as a function of incoming pressure. The dashed lines correspond to the model predictions.

Sample	Ppeak [kPa]	Rate P. Rise (instantaneous) [kPa/s]	Rate of P. Rise (Peak) [kPa/s]
Layered STF 2A	127	1.3E6	1.5E5
Layered STF 2A Model	130	2.2E5	1.4E5
Layered STF 3A	178	4.5E6	2.3E5
Layered STF 3A Model	180	3.0E5	2.0E5
Layered STF 5A	262	5.5E6	3.3E5
Layered STF 5A Model	265	4.5E5	2.7E5

Table 6.8.3: Average values of rate of pressure rise and incoming pressure for layered STF-filled composites.

Despite the fact that we found that both layered system (glycerol and STF filled) are well behaved, in fact linearly with the incoming pressure, one needs to be careful to extrapolate this results to blast wave found in the field. Due to the shock tube limitations we were unable to reach higher incoming pressures. The ranges of pressures varied between 50 kPa to about 100kPa which is quite restrictive to investigate the parameters dependencies. Further investigation would be necessary to verify that this behavior is also seen in blast waves of greater magnitude. It is quite possible that at much greater incoming pressures the non-linear properties of the STF based composite will play a much greater role.

6.9. Conclusion

The silica based composite was found to be efficient in reducing the rate of pressure rise of shock waves. Single layer geometries did provide some protection (reduction of 1 order of magnitude in the rate of pressure rise) but they also always induced a magnification of the peak pressure. This magnification of pressure was found to relate to the weight of the sample as various filling fractions and thicknesses were tested.

A geometry of layering with fluid filled foam facing the incoming wave backed by unfilled foam reported the best performance. This composite was found to be well modeled by a double spring-mass-damper system for both glycerol and STF filled composites. In fact, the two composites exhibited similar behaviors, some difference did exist in the magnitude of the rate of pressure rise but the overall behavior was consistent.

Based on these results we can conclude that the STF layered composite can be used for blast mitigation as it can efficiently reduce the rate of pressure rise. Additionally the composite has the advantage of being flexible under normal wear circumstances and therefore can be used to create a protecting gear that wraps around the body chest. This is extremely important, as explained in section 2.3.4 as it allows for total coverage which is essential in close environments. Another advantage of these composites is that their flexibility allows for a better and easier range of motion which are invaluable properties for a soldier in the battlefield.

7. Conclusions

Shear thickening fluids and their ability to transition from a low viscosity to a solid like state has sparked much interest in the field of personal protection gears and energy absorption. In particular the army is in great need of a personal protecting gear that is efficient at energy absorption yet still flexible enough to wear in combat where soldier mobility and comfort is vital. Since the introduction of Kevlar soldiers' protection has been greatly improved but some threats still exist. In particular, as reported in section 2.4.1 nowadays most of the injuries seen from wounded soldiers coming back from Iraq and Afghanistan are the result of close-range explosions. Close-range explosions can cause great injuries as limbs and tissue damage, shrapnel puncture wounds, burns, head trauma, internal organ failure just to name a few. In this work we have focused on two types of injuries which we believe would benefit the most from a mitigation system based on a shear thickening fluid: Traumatic Brain Injuries (TBI) and Primary Blast Injuries (PBI).

For this purpose a suitable shear thickening fluid has been used and characterized. Silica particles of 300 nm in size were dispersed into ethylene glycol at a volume fraction of 60%. This suspension exhibited extreme shear thickening behavior both in shear and extension, and it was found to follow the Delaware Rutgers rule. The fluid was impregnated in polyurethane open cell foam with average size of 360 μm. Foam was chosen as the enveloping geometry because it best exploits the thickening properties of the fluid since squeeze flow is a combination of both shear and extension. Additionally, foam magnifies the strain rate the fluid is subjected to, as described in equation (4.2), maximizing the stress response. Foams also prevent settling of the particles in suspension which increase the lifespan of the composite.

To simulate the energies and strain rates experienced during impacts that result in TBI we subjected the fluid-filled composites to drop tower experiments. The impact kinetic energies of these experiments varied between 10^5 to 10^6 J/m^3; for comparison we report the impact energies resultant from a football tackle to be around 5×10^4 J/m^3 while a fall on hip about 3×10^3 J/m^3. A new mechanism of energy absorption has been found which utilizes viscoplastic deformation upon fluid solidification with the occurrence of shear banding and cracking. This mechanism allows the composite to absorb large amount of energies and still maintain a constant stress below critical level. These experiments have shown that the silica based composite is in fact a good candidate for use in application of TBI protection as it absorb energies of magnitudes comparable to the one experienced during injuries with stresses below 50 MPa (critical stress). Additionally the composite is flexible and therefore comfortable to wear for the user head. The deployment of this material for TBI protection can be easily implemented as a band of this material could be inserted directly in a preexisting helmet. This would make for a fast and easy transition which is beneficial for the army and ultimately for the soldier in the field.

The other type of injury that we believe could benefit the most from an active-fluid based composite are Primary Blast Injuries. To investigate the composite behavior under this type of loading the samples were tested in a shock tube apparatus. The samples were subjected to pressure pulses that varied in magnitude between 50 to 100 kPa with pulse durations of a few milliseconds. A layering geometry with the heavy, fluid filled foam facing the wave, backed by a layer of unfilled foam gave the greater reduction in the rate of pressure rise. The rate of pressure rise is in fact the parameter of the wave that has been linked to primary blast injuries. This mechanism and the layered composite behavior have been shown to be well captured by a double spring-mass-damper model. This composite offers great advantages over the previously used method of layering hard plates with foam. In fact, because of its flexibility it allows for better body fitting and can be used to effectively and more comfortably cover the torso in totality. This is extremely important especially in closed environment when shock waves come from all directions. Additionally, because of its flexibility it allows for blast protection without limiting the range of motion of the user which is extremely important in the battlefield.

Bibliography

1. King, A.I., *Fundamentals of impact biomechanics: Part I --Biomechanics of the head, neck, and thorax.* Annu.Rev. Biomed. Eng., 2000. **2**: p. 55-81.
2. Stickel, J.J. and R.L. Powell, *Fluid Mechanics and Rheology of Dense Suspensions.* Annu. Rev. Fluid Mech., 2005. **37**: p. 129-49.
3. Barnes, H.A., *Shear-Thickening ("Dilatancy") in suspension of nonaggregating solid particles dispersed in newtonian liquids.* Journal of Rheology, 1989. **33**(2): p. 329-366.
4. Hoffman, R.L., *Discontinuous and dilatant viscosity behavior in concentrated suspension III. necessary conditions for their occurrence in viscometric flows.* Advances in Colloid and interface science, 1982. **17**: p. 161-184.
5. Hoffman, R.L., *Explanations for the cause of shear thickening in concentrated colloidal suspensions.* Journal of Rheology, 1998. **42**(1): p. 111-123.
6. Laun, H.M., R. Bung, and F. Schmidt, *Rheology of extremely shear thickening polymer dispersions (passively viscosity switching fluids).* Journal of Rheology, 1991. **35**(6): p. 999-1034.
7. Laun, H.M., R. Bung, S. Hess, W.Loose, O.Hess, K.Hank, E.Hadicke, R.Hingmann, F.Schmidt, and P.Linder, *Rheological and small-angle neutron-scattering investigation of shear-induced particle structures of concentrated polymer dispersions submitted to plane poiseuille and couette-flow.* Journal of Rheology, 1992. **36**(4): p. 743.
8. Bender, J. and N.J. Wagner, *Reversible shear thickening in monodisperse and bidisperse colloidal dispersions.* Journal of Rheology, 1996. **40**(5): p. 899-916.
9. Maranzano, B.J. and N.J. Wagner, *Flow-small angle neutron scattering measurements of colloidal dispersion microstructure evolution through the shear thickening transition.* Journal of Chemical Physics, 2002. **117**(22): p. 10291-10302.
10. Maranzano, B.J. and N.J. Wagner, *The effects of particle size on reversible shear thickening of concentrated colloidal dispersion.* Journal of chemical physics, 2001. **114**(23): p. 10514.
11. D'Haene, P., J. Mewis, and G.G. Fuller, *Scattering dichroism measurements of flow-induced structure of a shear thickening suspension.* Journal of Colloid and Interface Science, 1993. **156**(2): p. 350-358.
12. Bender, J.W. and N.J. Wagner, *Optical measurement of the contribution of colloidal forces to the rheology of concentrated suspensions.* Journal of Colloid and Interface science, 1995. **172**: p. 171-184.
13. Bossis, G. and J.F. Brady, *The rheology of brownian suspensions.* J. Chem. Phys., 1989. **91**(3): p. 1866-1874.
14. Boesma, W.H., J. Laven, and H.N. Stein, *Computer simulations of shear thickening of concentrated dispersions.* Journal of Rheology, 1995. **39**(5): p. 841-860.
15. Foss, D.R. and J.F. Brady, *Structure, diffusion and rheology of Brownian suspensions by stokesian dynamic simulation.* Journal of Fluid Mechanics, 2000. **407**: p. 167-200.

16. Catherall, A.A., J.R. Melrose, and R.C. Ball, *Shear thickening and order-disorder effects in concentrated colloids at high shear rates.* Journal of Rheology, 2000. **44**(1): p. 1-25.
17. Boek, E.S., P.V. Coveney, H.N.W. Lekkerkerker, and P. vanderSchoot, *Simulating the rheology of dense colloidal suspensions using dissipative particle dynamics.* Physical Review E, 1997. **55**(3): p. 3124-3133.
18. Singh, P., T.I. Hesla, and D.D. Joseph, *Distributed Lagrange multiplier method for particulate flows with collisions.* International Journal of Multiphase Flow, 2003. **29**(3): p. 495-509.
19. Hoffman, R.L., *Discontinuous and dilatant viscosity behavior in concentrated suspensions. I. Observation of flow instability.* Journal of Rheology, 1972. **16**(1): p. 155-173.
20. Batchelor, G.K., *Effect of Brownian-motion on bulk stress in a suspension of spherical-particles.* Journal of fluid mechanics, 1977. **83**: p. 97-117.
21. Larson, *The Structure and Rheology of Complex Fluids.* 1999, New York: Oxford University Press.
22. DeKruif, C.G., E.M.F. Vanlersel, and A. Vrij, *Hard sphere colloidal dispersions: Viscosity as a function of shear rate and volume fraction.* J. Chem. Phys., 1985. **83**(9): p. 4717-4725.
23. Hiemenz, P.C. and R. Rajagopalan, *Principles of Colloid and Surface Chemistry.* 1997, New York: Marcel Dekker, Inc.
24. Batchelor, G.K., *Browning Diffusion of Particles with Hydrodynamic Interaction.* J. Fluid Mech., 1976. **74**: p. 1-29.
25. Barnes, H.A., J.F. Hutton, and W. F.R.S., *An Introduction to Rheology.* 1989, New York: Elsevier.
26. Wagstaff, I. and C.E. Chaffey, *Shear Thinning and Thickening Rheology.* Journal of colloid and Interface Science, 1977. **59**(1): p. 53-62.
27. D'Haene, P. and J. Mewis, *Rheological characterization of bimodal colloidal dispersions.* Rheologica Acta, 1994. **33**: p. 165-174.
28. Egres, R. and N. Wagner, *The rheology and microstructure of acicular precipitated calcium carbonate colloidal suspensions through the shear thickening transition.* Journal of Rheology, 2005. **49**(3): p. 719-746.
29. Maranzano, B.J. and N.J. Wagner, *The effects of interparticle interactions and particle size on reversible shear thickening: Hard-sphere colloidal dispersions.* Journal of Rheology, 2001. **45**(5): p. 1205-1222.
30. Raghavan, S.R. and S.A. Khan, *Shear-thickening response of fumed silica suspensions under steady and oscillatory shear.* Journal of Colloid and Interface Science, 1997. **185**(1): p. 57-67.
31. Lee, Y.S. and N. Wagner, *Dynamic properties of shear thickening colloidal suspensions.* Rheologica Acta, 2003. **42**: p. 199-208.
32. Doraiswamy, D., A.N. Mujumdar, I. Tsao, A.N. Beris, S.C. Danforth, and A.B. Metzner, *The Cox-Merz rule extended: a rheological model for concentrated suspensions and other materials with yield stress.* Journal of Rheology, 1991. **35**: p. 647-685.
33. Sami, S.,1996,Stokesion dynamics simulations of Brownian suspension in extensional flow,Pasadena,Master Thesis California Institute of Technology,52

34. Hayes, W.C., S.N. Robinovitch, and T.A. McMahon,"Bone fracture prevention garment and method",1997
35. Gibson, L.J. and M.F. Ashby, *Cellular solids Structure & Properties*. 1988: Pergamon Press.
36. Hilyard, N.C. and A. Cunningham, *Low Density Cellular Plastics*. 1994, London: Chapman & Hall.
37. Pearson, J.R.A. and P.M.J. Tardy, *Models for flow on non-Newtonian and complex fluids through porous media.* J. Non-Newtonian Fluid Mechanics, 2002. **102**: p. 447-473.
38. Biot, M.A., *Theory of propagation of elastic waves in a fluid-saturated porous solid. I Low frequency range. II Higher frequency range.* J. Acoustic. Soc. Am., 1956. **28**: p. 168-191.
39. Kim, J.M., R.R. Parizek, and D. Elsworth, *Evaluation of fully-coupled strata deformation and groundwater flow in response to longwall mining.* International Journal of Rock Mechanics and Mining Sciences, 1997. **34**(8): p. 1187-1199.
40. Parra, J.O., *Poroelastic model to relate seismic wave attenuation and dispersion to permeability anisotropy.* Geophysics, 2000. **65**(1): p. 202-210.
41. Williams, K.L., D.R. Jackson, E.I. Thorsos, D.J. Tang, and S.G. Schock, *Comparison of sound speed and attenuation measured in a sandy sediment to predictions based on the Biot theory of porous media.* Ieee Journal of Oceanic Engineering, 2002. **27**(3): p. 413-428.
42. Kim, Y.J., L.J. Bonassar, and A.J. Grodzinsky, *The Role of Cartilage Streaming Potential, Fluid-Flow and Pressure in the Stimulation of Chondrocyte Biosynthesis During Dynamic Compression.* Journal of Biomechanics, 1995. **28**(9): p. 1055-1066.
43. Li, L.P., M.D. Buschmann, and A. Shirazi-Adl, *A fibril reinforced nonhomogeneous poroelastic model for articular cartilage: inhomogeneous response in unconfined compression.* Journal of Biomechanics, 2000. **33**(12): p. 1533-1541.
44. Korhonen, R.K., M.S. Laasanen, J. Toyras, R. Lappalainen, H.J. Helminen, and J.S. Jurvelin, *Fibril reinforced poroelastic model predicts specifically mechanical behavior of normal, proteoglycan depleted and collagen degraded articular cartilage.* Journal of Biomechanics, 2003. **36**(9): p. 1373-1379.
45. Zhao, H., *Testing of Polymeric Foams at High and Medium strain rates.* Polymer Testing, 1997. **16**: p. 507-516.
46. Chen, W., F. Lu, and N. Winfree, *High-strain-rate Compressive Behavior of Rigid Polyurethane Foam with Various Densities.* Experimental Mechanics, 2002. **42**(1): p. 65-73.
47. Chen, W., F. Lu, D.J. Frew, and M.J. Forrestal, *Dynamic Compression Testing of Soft Materials.* Journal of Applied Mechanics, 2002. **69**: p. 214-223.
48. Chen, W., B. Zhang, and M.J. Forrestal, *A Split Hopkinson Bar Technique for Low-impedance Materials.* Experimental Mechanics, 1999. **39**(2): p. 81-85.
49. Chen, W., F. Lu, and B. Zhou, *A Quartz-crystal-embedded Split Hopkinson Pressure Bar for Soft Materials.* Experimental Mechanics, 2000. **40**(1): p. 1-6.

50. Gary, G., J.R. Klepaczko, and H. Zhao. *Correction for wave dispersion and analysis of small strains with split Hopkinson bar.* in *Proceedings of the international symposium on impact engineering*. 1992. Sendai, Japan.
51. Wang, L., K. Labibes, Z. Azari, and G. Pluvinage. *On the use of a viscoelastic bar in the split Hopkinson bar technique.* in *Proceedings of the international symposium on impact engineering*. 1992: Sendai, Japan.
52. Wightman, J.M. and S.L. Gladish, *Explosion and Blast Injuries.* Annals of Emergency Medicine, 2001. **37**(6): p. 664-678.
53. Hayda, R., R.H. Harris, and C.D. Bass, *Blast Injury Research.* Clinical orthopedics and related research, 2004. **422**: p. 97-108.
54. Cooper, G.J., *Protection of the lung from blast overpressure by thoracic stress wave decouplers.* The Journal of Trauma: Injury, Infection and critical care, 1996. **40**(3): p. 105-110.
55. Iremonger, M.J., *Physics of detonations and blast-waves*, in *Scientific Foundations of Trauma*, G.J. Cooper, et al., Editors. 1997, Butterworth-Heinemann. p. 189-199.
56. Mayorga, M., *The pathology of primary blast overpressure injury.* Toxicology, 1997. **121**: p. 17-28.
57. Yelverton, J.T., *Blast Biology*, in *Scientific Foundations of Trauma*, G.J. Cooper, et al., Editors. 1997, Butterworth-Heinemann: Oxford, UK. p. 200-213.
58. Stuhmiller, J.H., *Biological response to blast overpressure: A summary of modeling.* Toxicology, 1997. **121**: p. 91-103.
59. Hull, J.B. and G.J. Cooper, *Pattern and mechanism of traumatic amputation by explosive blast.* Journal of Trauma: Injury, Infection, and Critical Care, 1996. **40**: p. S198-S205.
60. Cernak, I., J. Savic, D. Ignjatovic, and M. Jevtic, *Blast injury from explosive munitions.* Journal of Trauma: Injury, Infection, and Critical Care, 1999. **47**(1): p. 96-104.
61. Fung, Y.C., *Strength, Trauma and Tolerance*, in *Biomechanics of Motion, Flow, Stress, and Growth.* 1990, Springer-Verlang: New York.
62. Grimal, Q., S. Naili, and A. Watzky, *Nonpenetrating impact on the thorax: influence of curvature on wave propagation.* C.R. Mecanique, 2002. **330**: p. 569-574.
63. Cooper, G.J. and A. Jonsson, *Protection against blast injury*, in *Scientific Foundations of Trauma*, G.J. Cooper, et al., Editors. 1997, Butterworth-Heinemann: Oxford, UK.
64. Axelsson, H. and J.T. Yelverton, *Chest wall velocity as a predictor of nonauditory blast injury in a complex wave environment.* Journal of Trauma: Injury, Infection, and Critical Care, 1996. **40**(3): p. S31-S36.
65. Stuhmiller, J.H., K.H. Ho, M.J. Vander Vorst, K.T. Dodd, T. Fitzpatric, and M. Mayorga, *A model of blast overpressure injury to the lung.* Journal of Biomechanics, 1996. **29**(2): p. 227-234.
66. Cooper, G.J., D.J. Townend, S.R. Cater, and B.P. Pearce, *The role of stress waves in thoracic visceral injury from blast loading: modification of the stress transmission by foam and high-density materials.* Journal of Biomechanics, 1991. **24**: p. 273-285.

67. Makris, A., D.L. Frost, J. Nerenberg, and J.H.S. Lee. *Attenuation of a blast wave with cellular material.* in *20th International Symposium on Shock Waves*. 1996. Pasadena: World Scientific.
68. Ouellet, S., D.L. Frost, and A. Bouamul, *Using a shock tube to predict the response of polymeric foam to a blast loading.* J. Phys. IV France, 2006. **134**: p. 783-787.
69. Glass, I.I., *Shock tubes: theory and performance of simple shock tubes*. 1958, University of Toronto: Toronto.
70. Glass, I.I., W. Martin, and G. Patterson, *A theoretical and experimental study of a shock tube*. 1953, University of Toronto: Toronto.
71. Thurman, D.J., C.M. Branche, and J.E. Sniezek, *The Epidemiology of sport-related traumatic brain injuries in the United States: recent development.* J. Head Trauma Rehabil., 1998. **13**(2): p. 1-8.
72. Zhang, L., K.H. Yang, and A.I. King, *A proposed injury threshold for mild traumatic brain injury.* Journal of Biomechanical Engineering, 2004. **126**: p. 226-236.
73. Langlois, J.A., W. Rutland-Brown, and K.E. Thomas, *Traumatic brain injury in the United States: emergency departments visits, hospitalization, and deaths*. 2004, Center for Disease Control and Prevention.
74. Okie, S., *Traumatic brain injury in the war zone.* New England Journal of Medicine, 2005. **352**: p. 2043.
75. Gondusky, J.S. and M.P. Reitere, *Protecting military convoys in Iraq: An examination of battle injuries sustained by mechanized battalion during Operation Iraqi Freedom II.* Military Medicine, 2005. **170**(6): p. 546-549.
76. Mannion, R.J., J. Cross, P. Bradley, J.P. Coles, D. Chatfield, A. Carpenter, J.D. Pickard, D.K. Menon, and P.J. Hutchinson, *Mechanism-based MRI classification of traumatic brainstem injury and its relationship to outcome.* Journal of Neurotrauma, 2007. **24**(1): p. 128-135.
77. Gilchrist, M.D., *Experimental device for simulating traumatic brain injury resulting from linear accelerations.* Strain, 2004. **40**: p. 180-192.
78. Al-Bsharat, A.S., W.N. Hardy, K.H. Yang, T.B. Khalil, S. Tashman, and A.I. King. *Brain/skull relative displacement magnitude due to blunt head impact: new experimental data and model.* in *Stapp Car Crash Conference*. 1999.
79. Margulies, S.S. and L.E. Thibault, *A proposed tolerance criterion for diffuse axonal injury in man.* Journal of Biomechanics, 1992. **25**(8): p. 917-923.
80. Pfister, B.J., T.P. Weihs, M. Betenbaugh, and G. Bao, *An in vitro uniaxial stretch model for axonal injury.* Annu. Biomed. Eng., 2003. **31**: p. 589-598.
81. LaPlaca, M.C., D.K. Cullen, J.J. McLoughlin, and R.S.C. II, *High rate shear strain of three-dimensional neural cell cultures: a new in vitro traumatic brain injury model.* Journal of Biomechanics, 2005. **38**: p. 1093-1105.
82. Morrison, B., K.E. Saatman, D.F. Meaney, and T.K. McIntosh, *In vitro central nervous system models of mechanically induced trauma: A review.* Journal of Neurotrauma, 1998. **15**: p. 911-928.
83. Goldsmith, W., *The state of head injury biomechanics: past, present, and future: part 1.* Critical Reviews in Biomedical Engineering, 2001. **29**(5): p. 441-600.

84. Ommaya, A.K. and A.E. Hirsch, *Tolerances for cerebral concussion from head impact and whiplash in primates.* Journal of Biomechanics, 1971. **4**: p. 13-21.
85. Lowenhielm, P. *Brain susceptibility to velocity changes, relative and absolute limits for brain tissue tolerance to trauma and their relation to actual traumatic situations.* in *International Interdisciplinary Symposium on Traffic Speed and Casualities.* 1975. Funen, Denmark.
86. Ewing, C.L., D.J. Thomas, L. Lustick, E. Becker, G. Becker, G. Willems, and W.H. Muzzy. *The effect of the initial position of the head and neck to Gx impact accelerations.* in *19th Stapp Car Crash Conference.* 1975. Warrendale, USA.
87. Pincemaille, Y., X. Trosseille, P. Mack, C. Tarriere, F. Breton, and B. Renault. *Some new data related to human tolerance obtained from volunteer boxers.* in *33rd Stapp Car Crash Conf.* 1989.
88. Zhou, C., T.B. Khalil, and A.I. King. *A new model comparing impact responses of the homogeneous and inhomogeneous human brain.* in *39th Stapp Car Crash Conference.* 1995.
89. Cross, M.M., *Rheology of non-Newtonian fluids: A new flow equation for pseudo-plastic system.* J. Colloids Sci., 1965. **20**: p. 417-437.
90. Pipkin, A.C., *Lectures on viscoelasticity theory.* Applied Mathematical Sciences 1972, New York: Springer-Verlag.